The Use of A Digital Image Correlation Method With A Low Speed Camera to Obtain Characteristics of Surface Velocity and Sound Radiation for Automotive-Type Panels.

by

Mohd Faizal Mat Tahir

Doctoral Thesis

Submitted in partial fulfilment of the requirements for the award of
Doctor of Philosophy

Department of Aeronautical and Automotive Engineering
Loughborough University
United Kingdom

August 2018

Parts of the work contained in this thesis have previously been published by the author at the following conference:

INTER-NOISE 2015, the 44th International Congress and Exposition on Noise Control Engineering, will be held in San Francisco, California, United States of America, 9 -12 August 2015.

And the conference reference is

MAT TAHIR, M.F., WALSH, S.J. and O'BOY, D.J., 2015. Evaluation of the digital image correlation method for the measurement of vibration mode shapes. Inter-Noise and Noise-Con Congress and Conference Proceedings, 9-12th Aug., 2015, pp. 1986-1995

Abstract

The perceived quality of a vehicle is highly influenced by the driver's experience of the vehicle interior noise. Significant research has been carried out all over the world in order to characterize structural and acoustic characteristics, to control and minimize the vibration and noise from entering or emitted to vehicles.

Designers require tools to inform them whether the design changes are positive or negative in terms of the noise and vibration, and to help validate numerical finite element models of complicated structures.

This research explores the use of Digital Image Correlation (DIC) equipment and methods by using a relatively inexpensive low speed camera to investigate the structural-acoustics characteristics applied to automotive-type panels, where otherwise a highly expensive and sensitive scanning laser Doppler vibrometer would be required. Experimental measurements based on Noise Path Analysis (NPA) have been carried out and theoretical and numerical predictions on sound radiation behaviour have been developed. The prediction values have been evaluated and validated with experimental measurements.

Using a DIC measurement method to obtain spatially averaged surface velocities, averaged over several cycles through phase locking, the results for the sound power predictions for the selected mode shape and the resonance frequencies provided a good estimation when comparing with the experiment. For mode (1, 1), the sound power prediction was 80.9 dB while the measured one was 77.2 dB with a difference of 3.7.while the other selected modes showed a difference not more than 3.7 dB. It was within the range suggested by considering the mathematical simplification approach during the prediction development stage.

To conclude, it was found that the prediction of sound power throughout the vibrating structure can provide a good accuracy by using the DIC method Therefore, it can be an alternative technique to evaluate the sound radiation for characterizing one of the structural properties

Acknowledgment

Firstly, I would like to take this opportunity to express my genuine appreciation to both of my supervisors, Dr Stephen Walsh and Dr Dan J. O'Boy for giving his undying support, encouragement, and advice from the start of my journey until the completion of my research and thesis. I am profoundly grateful to have them as my supervisors and really thankfulness for their great assistance and patience in seeing through my progression to along my PhD study.

Many thanks to my sponsors, Universiti Kebangsaan Malaysia (UKM) and the Malaysian Government who funded my study at the Aeronautical and Automotive Engineering Department, Loughborough University, UK.

I would like to thank Dr. Azma Putra, for assisting me with valuable technical support and taking the time to discuss about various aspects of the research work. Not to forget, my entire colleague in AAE Department, especially Dr Ezhan, and Dr Ajith Pai for wonderful technical and motivation discussion during the research period. Thanks also to all my friends in Loughborough from Masyarakat Melayu Loughborough (MML) especially the "Thorpe Acre Geng" who thoroughly always volunteering in helping with truthfully without expecting anything as returns.

Special thanks to my dearest wife, Siti Munirah Mat Yunoh, and both my lovely son, Muhammad Adib Aiman and Muhammad Raihan Kamil for the love, support, inspiration, sacrifice and understanding continuously from the start of the journey until the finish line. Not forget to my newborn baby girl, Aisyah that bring more joy and happiness to my long and struggle Phd journey, Insyallah.

All thanks to my beloved mother, Pon Binti Mohamed, and my father Mat Tahir bin Ismail who are keep supporting and believe in me since my birth. Both of you are my true strength and I will always pray to God for your healthy and goodness in here and hereafter, Insyallah. To my father in law, Mat Yunoh bin Dollah and my mother in law, thank you for always stand there behind me. Not to forget all my family members from both sides especially: Along, Angah, Uda, Amim dan Mocu, I cannot find any words to express my appreciation for your understanding and

support during my PhD study. Family always first and there is nothing more important than family.

Finally, to all my friends and everybody who involve in my PhD journey directly or indirectly, only a true gratitude can I expressed to you and may Allah reward all of you with goodness.

List of figure

List of tables

Table of content

CHAPTER 1
Introduction

1.1 Research Overview

Automotive technologies have significantly developed since the creation of the steam engine automobile in the year of 1769. It is generally acknowledged that the first really practical automobiles with petrol/gasoline-powered internal combustion engines were completed almost simultaneously by several German inventors working independently. When Carl Benz built his three-wheeled Benz Patent-Motorwagen in 1885, it was regarded as the year of birth of the modern automobile [1]. In today's market, customers desire an extra quality factor which doesn't depend only on the engine and body shape, but the interior materials, trim and fixtures. The established brands are concerned with the increasing levels of comfort and luxury at the same time as reducing insulation and overall vehicle weight, cost and ensuring the product uses the most sustainable materials. With the current trend of increasing oil price and the need for more green technology, manufacturers and developers need to produce products which are the lightest, strongest, most eco-friendly and environmentally clean whilst still maintaining speed of production and without ignoring the human factor perception such as aesthetic, ergonomic and quality inside the cabin.

Noise, vibration and harshness (NVH) benchmarks are important modern qualities needed for any transportation. NVH is the study and modification of the noise and vibration characteristic of vehicles. Whereas noise and vibration can be measured, harshness directed more towards subjective quality assessments. It is measured by a group of jury evaluation or with analytical tools that can deliver results reflecting human subjective impressions. Thus, significant research has been carried out in previous decades to improve on noise control whether at the source stage (the starting point of the noise source), their path or even at the receiver stage and at the end user. The noise inside the cabin has become one of the perceived qualities of importance in buyer selection criteria. Customers want their

automobile to have superiority in technical and economical aspects such as comfort and relaxation, safety, engine specification and fuel consumption [2]. Therefore, for a certain car manufacturer, luxuriant sound quality has become a critical customer perception in choosing the segment and target market they want to cater for [3]. As a result, preparation and designing any sound package is a vital feature in the vehicle development process, especially from an early design stage.

Products such as insulation, absorption and damping materials are widely available in the market today for noise and vibration control purpose, but the majority of them are weighty and expensive. Extra material for the purpose of noise and vibration control will result in an extra cost, which contradicts with the requirement for a low price vehicle solution. It also will result in higher fuel consumption due to the increasing weight. Due to this, designing a good sound package for any type of vehicle is very challenging in order to achieve a good compromise between the acoustics needed and vehicle cost and weight target.

While the removal of combustion engines is likely in the next few decades, the masking effect these have on road noise, suspension noise and mechatronic sounds means that it is unlikely that the sound proofing will be immediately reduced (therefore, panels and components will still have relatively heavy damping materials added). This damping material takes space, time to install, is costly and adds complexity to numerical finite element models. It is however, particularly effective at reducing the noise and vibration across a relatively broad frequency range.

For vehicles, decreasing the panel sound radiation inside the vehicle's passenger compartment is one of the main concerns in automobile body Noise, Vibration and Harshness (NVH). The panels enclosing the vehicle body structure are designed to keep the body-in-white (BIW) mass low, which accounts for the efficient fuel economy [4], especially with the transition from steel joined with spot welds to aluminium extrusions joined with adhesive. So, generally, these panels are made out of thin sheet metal, which by itself has a very low bending stiffness. It is a

common practice to look for ways to increase the stiffness of these thin quasi-flat panels by introducing ribs, stiffeners or beads [5].

Performing numerical optimization is a common engineering technique for finding solutions to complex problems. One such complex problem that numerical optimisation has been applied to is the minimization of sound radiation from structures or structural components, such as vehicle structures [6]. In some of the published work, structural-acoustic optimisation is considered from a geometrically idealised point of view, such as beams [7], ribbed panel [8], and sandwich plates [9] excited by simple excitation. Moreover, structural-acoustic optimisations have a great application in vehicle NVH.

However, conventional measurements for structural dynamics are gained from sensors which are discrete and required to have a contact between surface and sensor. This type of sensor such as an accelerometer and strain gauge may modify the dynamic response in a small scale, especially when contacted with a light weight structure such as aluminium plate. Furthermore, the conventional measurements always involve samples that need to be measured directly and will result in a delay and potentially delay the start of a production line (in practice, this wouldn't happen, as the deadline for production is rigid, and work would be carried out to get to that point in any case). Thus, the demand for a non-contact or non-destructive test (NDT) method has increased, because the NDT methods have the ability to test rapidly and with robust outcomes. The importance of this is that it potentially allows the designer to compare vehicles on the production line with the design expectations without halting the line, stopping work or interfering with the quality of the product (e.g. surface finish), which would allow a link between the finite element design models and the actual manufactured product to be compared, to evaluate items like manufacturing tolerances and the bandwidth of any design benchmarks.

Nowadays, there are few advanced techniques that are capable to measure the dynamic response over a particular measurement area without contacting the surface and they start to emerge as reliable techniques. Some of techniques are

laser Doppler vibrometry (LDV) and three dimensional digital image correlations (3D-DIC). The former is highly expensive and requires both a highly accurate experimental setup but more importantly, a stable and low vibration ground surface, which is unlikely in the manufacturing plant areas. The latter systems are often based around highly expensive high speed cameras, required to take multiple photographs over a very narrow time window. Addressing this point is one of the key themes of this thesis, through the potential use of a low speed camera setup.

The designer is often restricted in the number of vehicles that can be tested, and the ability to test production vehicles in a rapid, non-destructive way without impacting the production line is highly valuable. This thesis offers one way to address this problem.

Both high speed cameras and laser Doppler vibrometry techniques are capable of measuring a vast number of measurement degrees of freedom without modifying the structural response [10]. They have the ability to measure the response at thousands of points across the surface of the entire test specimen and as a result, more data can be collected. With each increment, more data and the ability to measure at more complicated locations (small or edge locations that are hard to access when involving sensors), the accuracy of the measurement can be increased.

One key advantage of providing a visual representation of the surface vibration to a designer is that they can see more of the mode shape, the intricacies of the component and how the specific stiffening and dampening materials affect the response shape.

For 3D-DIC methods, when required for higher frequency measurements, the use of high speed camera is essential which has the ability to measure in fast responses. However, when dealing with a controlled condition such as a periodic, repeatable vibration source such as a laboratory shaker, with linear, predictable forcing and repeatable boundary conditions, a low speed camera is also capable of providing the same measurements by taking images at a multiple of one cycle of the phase

plus a small movement. This additional step which is needed to be considered is investigated in this thesis. It offers the potential to introduce far cheaper low speed cameras into the DIC method as opposed to the far more expensive high speed ones, requiring more stable footing.

Furthermore, structure-borne noise is related with a sound being radiated from adjacent vibrating surfaces resulting from the impact on or vibration against it. Assessing sound radiation is always important in order to control and interpret what is required by the consumer. Sound power is one of the criteria which is considered in terms of the rate at which sound energy is emitted, reflected, transmitted or received and has the advantage of not varying with specific positions (sound pressure varies with position of measurement).

The research in this thesis develops specific knowledge of how to predict the sound power level which is radiated from a specific vibrating plate, using the DIC equipment and method with low speed cameras for frequencies which are of interest to automotive interior designers (less than approximately 550Hz). Whilst the plate is a simplified geometry, the research aims to show what might be possible for plates of arbitrary size and shape, such as a footwell of a passenger car or a boot space.

A numerical prediction for sound power will be developed based on the sequence of images captured by the camera of a plate vibrating with harmonic excitation. Next, validation of the prediction will be compared using the experimental methods on sound power measurement guided by international standards. Finally the research proposes some alternative approaches to run the experiment using the low speed cameras.

1.2 Problem Statement

The automotive industry has witnessed a trend in recent years of decreasing the bulk weight of a vehicle in order to achieve economical fuel consumption. Unfortunately, reduced bulk weight often compromises the noise, vibration and

harshness (NVH) characteristics of the vehicle. One need is to reduce the sound radiation from the modes of the structure that lie in a particular frequency range of interest.

The amount of noise reduction achieved will depend on the structural properties (mass, stiffness, and damping) of the car body. Damping in the structure plays an important role in reducing both structure-borne and airborne noise. Most common sound absorptive materials (thin porous foam, fibreglass, or glass wool) are good for absorbing high frequency sound and are used to control the NVH problem in the vehicle. This absorptive and damping material will be attached to a designated part in the vehicle, commonly to the body part for the purpose of reducing NVH.

In general, sound power determination for a structure is quite a difficult task to be performed. For small and easily moveable objects, this can be done in special anechoic or reverberation chambers using either the sound intensity or the sound pressure method. However more complex or large structures or ones where a higher background noise is present can be difficult to obtain reliable or accurate values. Automotive structures are normally complex, large and require a large acoustic building to have a proper measurement. With a lot of components inside an automotive vehicle, their surface body is always vibrating when active and require an appropriate calculation to reduce the vibration.

One other option is determination of airborne sound power by using the vibration surface measurement of the solid structure. However, there is only one technical specification standard and not a complete ISO standard for this method yet. Determination of the accurate spatial variation of vibration velocity using conventional vibration transducers is hard and time consuming because of insufficient number of measurement positions over the surface (and the need to replicate the experiment perfectly every time the transducer is moved). Furthermore, measuring on a thin surface with a direct contact transducer also has a possibility to reduce the velocity accuracy, with the additional risk that the contamination of the velocity due to the transducer mass changes with position. Hence the use of non-contact vibration measurement is of paramount importance.

For industrial use in a factory, if a designer wishes to validate the sound power predictions, they must take the vehicle to a specially instrumented anechoic chamber. As an alternative, this thesis explores the possibility of just using rapid surface velocity measurements to complete this task with minimal building cost, requirements and time.

1.3 Research Objectives

Three objectives need to be achieved.

1. To investigate structural-acoustic characteristics of the automotive-type panels through experiment and corresponding Finite Element Analysis.
2. To develop alternative approaches to phase-lock measurement for the DIC apparatus using a low speed camera and investigate the correlation between DIC methods with structural- acoustics behaviour.
3. To develop prediction and modelling methods for obtaining the sound power from a vibrating plate using a DIC approach and validate it using experimental measurement.

1.4 Research Questions

This research will be conducted to answer several research questions:

1. What is the boundary condition effect on the plate results? For a reliable experiment, how easy is it to achieve a consistent boundary condition which can be compared to ideal, theoretical models?
2. How to predict sound radiation from vibrating structure? What is the accurate theory for that and the correct approach to correlate between DIC and structural acoustics characteristic?
3. How to use the low speed camera for measuring much higher frequencies of a vibrating structure? Is there any potential for improving measurement technique for capturing vibrating body?
4. What are the potential errors for structure borne sound between prediction and measurement? Is there any significant contribution of improvement or potential to be further used on real engineering cases?

1.5 Research Novelty

This research provides an alternative approach to a scanning laser Doppler vibrometer to operate a low speed Digital Correlation Camera (DIC) setup using a phase-lock measurement method which is the important stage for operating a low speed camera's DIC measurement, whilst still obtaining data on harmonic excitation. The method requires spatial position data and position of the repetitive measurement signal (excitation force) to be recorded at the respective phase after certain period of complete loop cycles. The new approach focuses more on mathematical prediction and how to implement this technique in a practical setting, with knowledge of limitations and disadvantages. It provides a method to obtain the sound power of a plate without a need for anechoic buildings or expensive equipment.

The study also proposes a comprehensive technique on calculation of the spatial average mean square velocity, from the DIC measurements. The best practice method to set up the automotive type panel for the DIC measurement, in order to obtain full-field measurements (with a displacement value on every point location at each sequence of images) are being tracked and captured using a proprietary software, with the data being output and passed through to a Matlab data analysis routine. Later, the data is processed using Matlab to produce the essential velocity required.

Finally, the research provides modelling prediction for sound radiation from a vibrating plate. The sound power assessment can be predicted based from full-field displacement value captured from a sequence of images of plate vibration. This new method of prediction improves the traditional approach by providing more accurate spatial average mean square velocity involving calculating a vast number of point locations for full-field measurement. This thesis shows the potential for obtaining validated measurements of an automotive trim panel and associated structure, using a relatively inexpensive digital camera setup.

1.6 Arrangement of the thesis

This thesis begins by introducing some fundamental explanation and problems that are later addressed in the thesis. It provides basic insight into general current techniques related to determining the structural and acoustics characteristics for sample panels. Moreover, it discusses the three objectives that are planned to be achieved, research questions that arise during the research period and novelty in the research itself.

Next, chapter 2 discusses the literature as background to both the analytical and numerical methods with additional further details covering specifically the following respective chapters. Few highlights within the literature survey are the background on vehicle noise and the existing techniques and theory covering from the late 20^{th} century to early 21^{st} century.

In chapter 3, investigation of the structural-acoustic characteristics of the automotive type panel are presented. Resonance frequency and the mode shape of the panel with clamped boundary condition were explored by experiment and analytical method, with additional numerical and finite element analysis done by NX NASTRAN. The resonance values from the modal experiments have been validated through analytical calculation of natural frequency and double validation being done by FEM to determine the frequency and the mode shape for early modes. In this chapter, objective number one was addressed where the respective mode shapes and resonance frequencies for the plate were captured.

The thesis continues with chapter 4 by exploring the usage of Digital Image Correlation as a tool to capture the deflection of the plate from vibration source. With the limitation of the low speed camera, some mathematical approach is also proposed as an alternative to phase-lock measurement stage in order to run the low speed DIC camera for vibration that have higher frequency compared to the maximum frame per second capability of the camera. The deformation image captured by the DIC was later validated using NX NASTRAN.

Next, in Chapter 5, a model from the DIC deformation data have been developed to predict the sound power radiated from the vibrating plate. The parameter measured from the DIC with additional analytical mathematic modelling value are later included in the calculation for predicting the sound power. The predicted value of the calculation was then validated by the sound power experiment value.

Finally in chapter 6, the overall conclusion for the whole thesis is discussed including findings in reference to the objectives that have been planned in chapter 1. Furthermore, few suggestions for potential future works that can be undertaken to improve the predicting accuracy are also discussed. The flowchart that represents the structure of the thesis content is shown in figure 1.1 below.

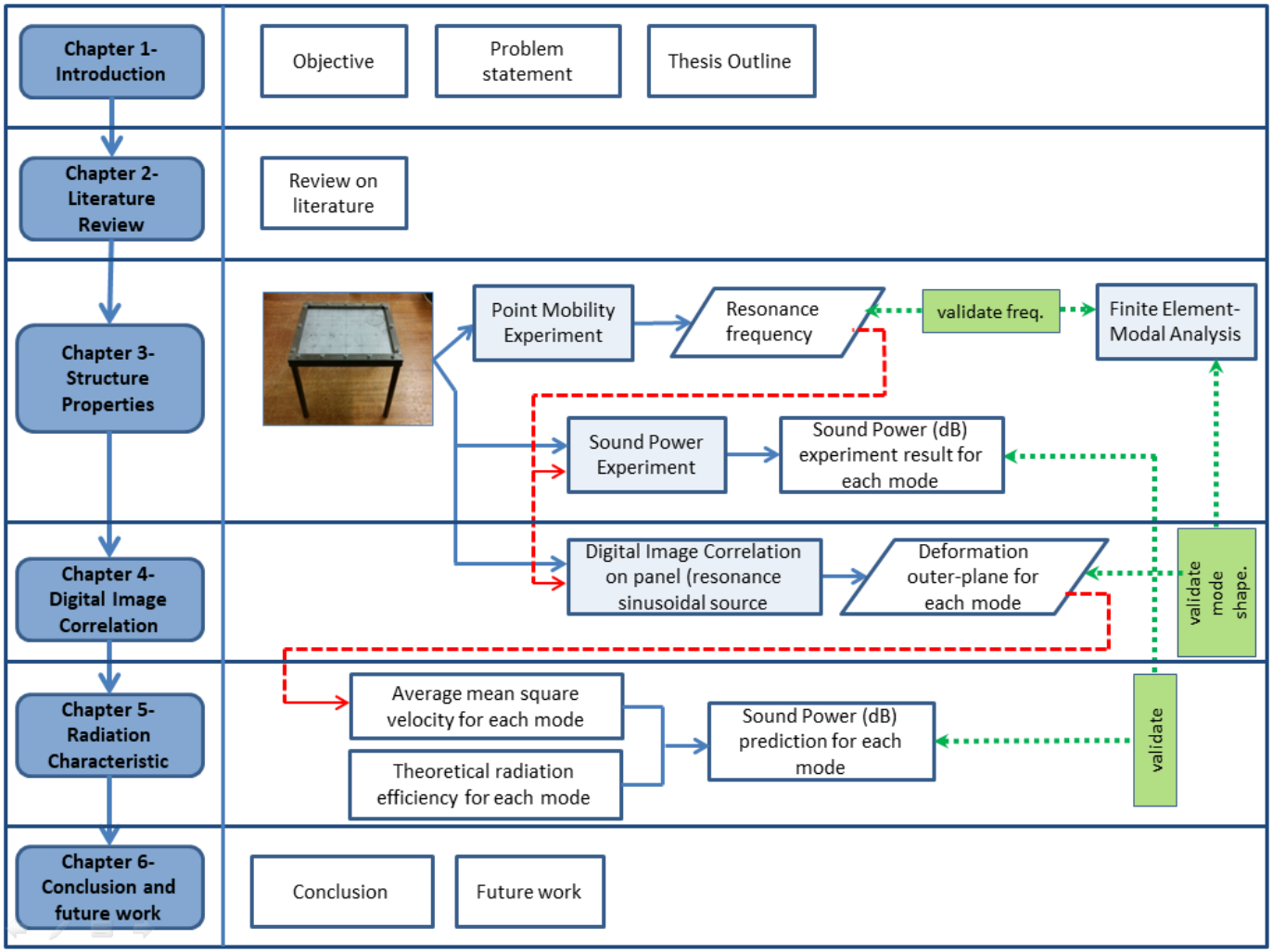

Figure 1.1 Flowchart of the thesis structure

CHAPTER 2
LITERATURE SURVEY

2.1 Introduction

This chapter contains an overall literature review starting by covering the main sources of vehicle noise such as engine, driveline, aerodynamic and tyre noise. Then the literature discussing noise path analysis and a few on current automotive sound packages to control noise, vibration and harshness (NVH) in automotive vehicles. The final part of the literature survey covers techniques in vehicle noise and vibration refinement such as experimental and simulation techniques which include digital image correlation (DIC) that will become the main method in determining the vibration response in this research.

2.2 Introduction to Vehicle Noise

Noise and vibration are truly important if consideration is to be given to the comfort level for the operator and passengers in any type of vehicle transportation. Noise and vibration energy are transferred to the end user or receiver from the source through specific paths, namely airborne and structure borne. This relationship might be simple but normally most of them are complex. Figure 2.1 shows the vehicle noise mechanism relationship from the source through the path and received by the receiver [11]. An example of relationship would be noise from an engine, propagating through the dashboard system and ending to the receiver as noise. A more complex relationship would be an aerodynamic noise going through a structural path and then emanating from the structure as an airborne noise.

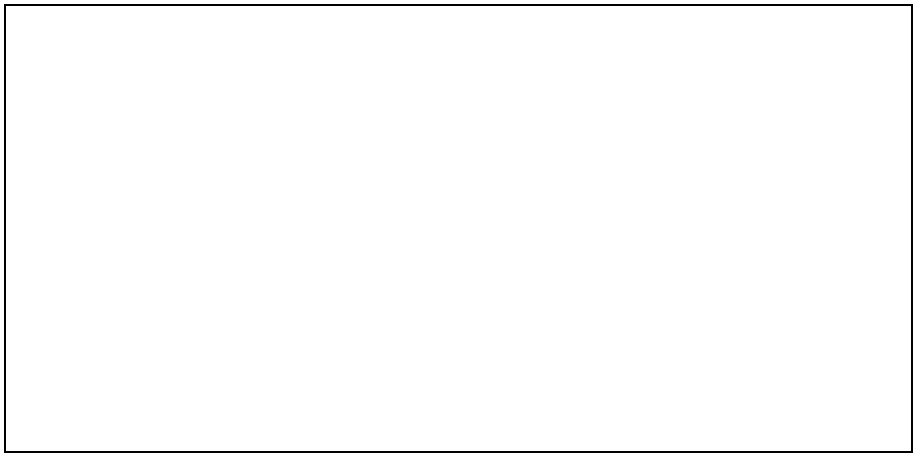

Figure 2.1 Image of vehicle noise mechanism (taken from ref.[11])

2.3 Vehicle Noise Source

There are numerous noise sources for any vehicle regarding interior or exterior noise. Generally, when discussing about impacts on the driver or passenger, interior noise is the main concern (without neglecting the other outside user who is exposed to exterior noise from vehicles, controlled by legislation through an ISO362 test). Interior noise in vehicle is caused by many and complex sources, primarily by engine, road and wind noise [12]. However, there are a lot of additional noise sources including transmission, driveline (driveshaft, differential, final drive), exhaust, brake, mechanical and electrical noise and others (squeak, rattle and tizz noises). In the past the engine was the most important, and the first NVH studies were applied to reduce noise and vibrations generated by the engine and powertrain. Due to the effort, both of the systems have improved a lot in terms of noise and vibration, thus making other sources that were less obvious previously more significant now.

2.3.1 Engine noise

The engine is the current essential requirement for an automobile and also one of the main recognized sources of noise. A conventional internal combustion engine (ICE) generates strong levels of noise and vibration which are composed of many components emitted from different sources as shown in figure 2.2 [13]. However, the vibrations from the engine are mainly

generated by the reciprocating and rotational masses such as the piston, connecting roads and shafts [14].

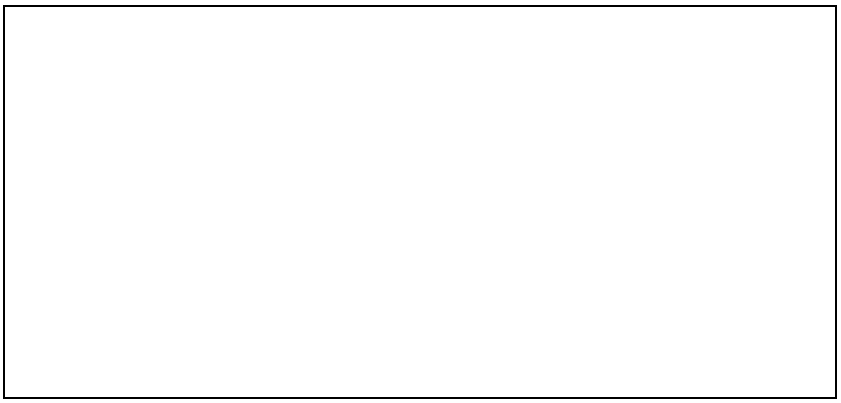

Figure 2.2 Image of an ICE engine noise source (taken from ref. [13])

The sources of engine noise contain combustion noise, mechanical noise and a combination of both. The relative mix of the two will vary between engines but as a general rule: i. Engine noise produced by spark ignition (gasoline) engines will be dominated by mechanical noise; while ii. Engine noise produced by compression ignition (diesel) engines will be having more contributors from combustion noise [15]. Combustion noise results from gas forces in the cylinder of the engine, causing vibration to occur which is then radiated as noise. While mechanical noise caused by the crank mechanism includes pistons, crankshaft and bearings with externally applied forces due to gas forces. It then also has initially generated forces due to its own inertia. Some researchers also include gas-flow as a primary source from the engine. Gas flow noise which is usually a low-frequency controlled source is associated with intake and exhaust processes including cooling fan movement and turbocharging [16] .

Diesel engines usually emit greater noise levels than gasoline engines at the same speed, which is caused by the higher in-cylinder pressure excitation [17]. Diesel engine produces a knocking, for instance impulsive and irregular noise, which has its own characteristic and unpleasant sound. Indeed the diesel engine sound quality is still lower than gasoline and the listener can differentiate easily between these two sounds [18]. In gasoline engines,

piston clearance is relatively small, thus mechanical noise tends to be dominated by impacts in the crankshafts.

Generally, the higher the engine speed, the higher the mechanical noise will be emitted regardless the size of the engine or fuel type. Head and Wade find that during transients, combustion noise is usually higher; typically of the range of 4-7 dBA [19]. Evangelos et.al noted that with the present of the injector, turbocharged diesel engines perform louder during acceleration compared with steady stated operation, up to almost 3 dBA [16].

2.3.2 Driveline noise

The drivetrain or driveline is the system in the vehicle that connects the transmission and delivers power to drive movement on the surface, whether its road, water or air. Figure 2.3 shows an example of BMW X-drive (4WD) driveline [20].

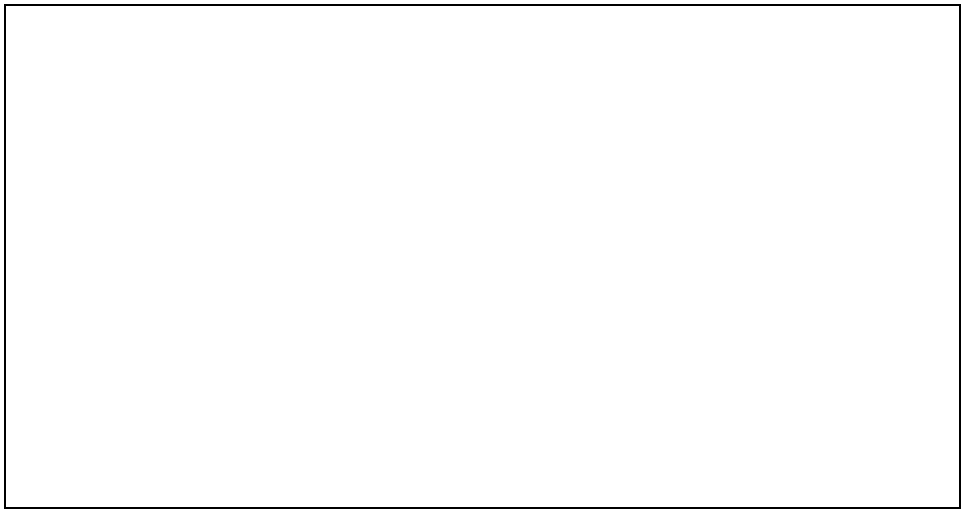

Figure 2.3 Image of an example of modern automobile's driveline (taken from ref.[20]).

The arrangement of the driveline can produce a diversity of NVH concerns across a broad frequency range. Rapid changes in the vehicle's load (for instance pedal tip-in/out) may be result in an objectionable vehicle shuffle

response, which is connected to the first natural frequency of the driveline. It is usually in the 2 Hz – 8 Hz frequency range (depending on the selected gear) [21]. Additionally, the dynamic mesh forces of a rear axle can be influenced by the driveline dynamics which results in axle whine, which is typically between 300 Hz – 1 kHz, while transmission whine can extend out to the 3 kHz - 4 kHz range. Figure 2.4 displays a list of most commonly encountered driveline NVH phenomena and their usual frequency range.

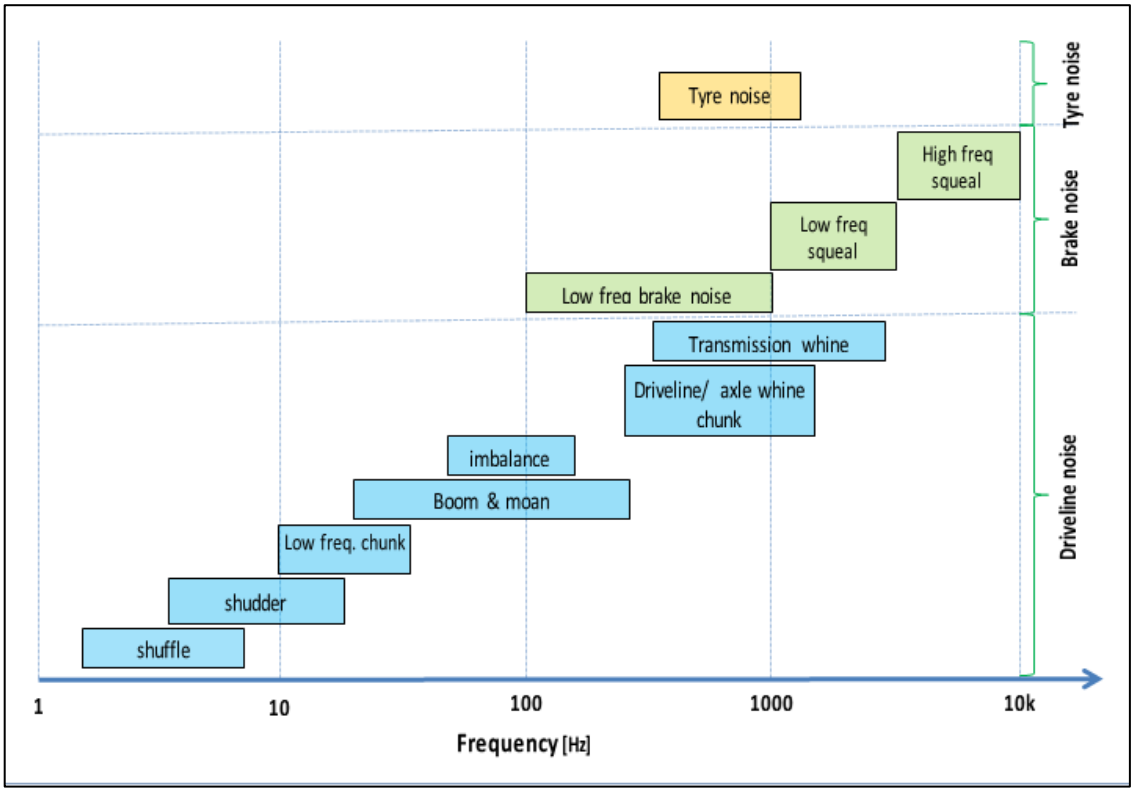

Figure 2.4 Typical frequency range of various automotive noise source.

2.3.3 Aerodynamic Noise/ Wind Noise

The aerodynamic or wind noise inside the cabin originate in the unsteady aerodynamic pressures generated by turbulent flow on the outside and underneath of the vehicle. Another important source can be the fluctuating pressures of the engine cooling fan, fans used to circulate air in the heating and air conditioning systems. These noise sources are mostly caused from turbulent flow separations, turbulent boundary layers, and natural turbulence

inherent in the oncoming airflow. Other typical noise sources also can result from the vortex shedding such as from antennae, side mirrors and as well as aspiration or leakage noise through the window and door seal [22].

Figure 2.5 (a) illustrates the origin of aerodynamic noise inside the car which is flow through grills, radiators and fans, and possible separation on the hood of the car, at the base of the windshield there is a separation where the air inlets for most cars are located. Then, in the area of the A-pillar, there is a strong vortex flow generated. Next on the side of the car around the windows there are a number of quasi-two dimensional separations behind various body parts and finally there are extremely complicated separated flows around the tyres and under the car in the locality of the engine compartment.

For a constant, high speed driving (> 100 km/h), the wind experienced by the moving vehicles will create most of the noise inside the cabin and will dominate other noise. Through ages, the new technology and vehicle refinement for the main sources (engine noise and road noise) have become more efficient; thus wind noise starts to be more noticeable and become a serious issue especially for all vehicle manufacturers. Wind tunnels are being used by the researchers to study vehicle wind noise, not only for crucial industries like airplanes and aerospace. However, Christian Peric et al. also recommend the importance of running on-the road conditions also due to the influence of large-scale turbulence inherent in the on-road wind environment [23].

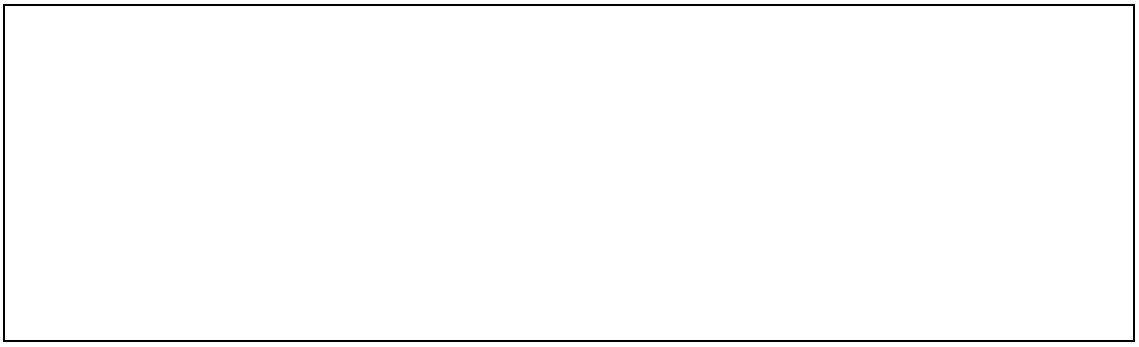

Figure 2.5 Image of (a) Flow around automobiles and some details of noise source regions; (b) possible aspiration/ leak noise source locations (taken from ref. [22]).

The performance of a vehicle door sealing system is crucial for the purpose of controlling wind noise. Doors on a vehicle may move outward at high speeds, because of the variance between the aerodynamic pressure outside and inside the vehicle cabin. As air can travel through the seal and cause aspiration if the door seal does not have enough ability to remain in tight contact with its mating surface, the sealing force must be high. Moreover, aspiration will occur if a seal takes more time to respond to its mating surface vibration. As soon as aspiration occurs, it can become one of the most dominant sources of wind noise in the passenger cabin. Figure 2.5 (b) shows some numerous locations where aspiration or leak noise can occur.

2.3.4 Road Noise/ Tyre Noise

Road noise is generally generated by events that occur at the pavement/ tyre interface. The source mechanisms are complex and change depending on tyre type and size, the road and pavement construction and vehicle operating condition [24]. The generation of road/tyre noise is complex but roughly they are due to an impacting mechanism, adhesion mechanism and air displacement mechanism (more or less related to structure-borne and airborne mechanism) and can be illustrated as in Figure 2.6 [25]. Tyre/road generation also can be amplified or reduced because of the horn effect, acoustical/mechanical impedance effect and tyre resonance [26].

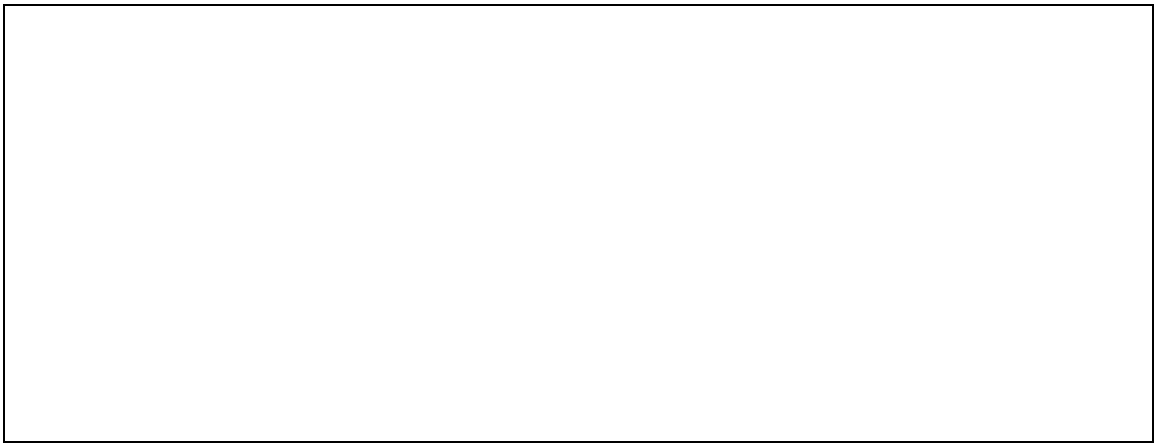

Figure 2.6: Image of a selection of tyre/road noise generation mechanisms (left); aerodynamic mechanisms (right) (taken from ref.[25])

Vehicles which do not have a proper-sealed floor and door structure can experience an airborne sound radiation either from the tread blocks and the sidewall of the tyre. However, most of the time, road noise is referred as a structure-borne noise. Vibrations that are caused by vehicle tyre/road surface impacts are transferred through the suspension, which then excite the vehicle structure to generate low frequency sound (<400 Hz). Furthermore, Keijiro in his study on mechanisms of tire/ road noise illustrate the contour map of sound intensity level from noise generating portions when the tire investigated under the coasting condition as shown in figure 2.7.

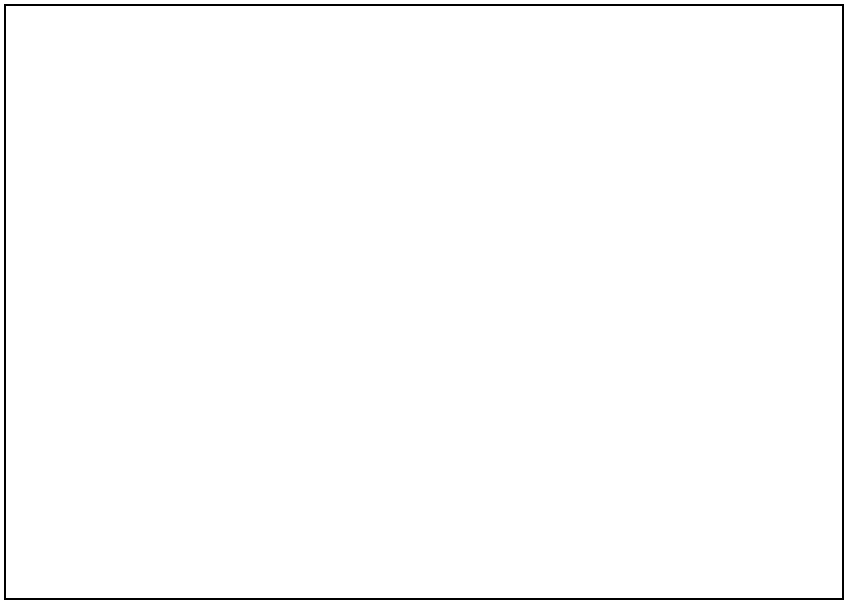

Figure 2.7 Image of contour map of sound intensity level (taken from ref.[27])

Road noise generally begins to be noticeable when vehicle speeds are more than 30 mph, but its contribution to overall interior noise happen between 40 and 60 mph and then decreases again, where aerodynamic noise becomes predominant. However, when compared with other mechanical noise (engine speed, engaged gear), tyre/road noise is 10 dB (A) higher than mechanical noise at 100 km/h in 5th gear [28].

2.3.5 Other Noise

Beside the entire primary noise source at vehicle, there is additional noise that exists and it's presence can be more noticeable, bothersome, indirect and sometime difficult to detect or mitigate such as droning, beat and brake squeal [29] . A lot of research is also being done to give some "desirable" and "quality" sound to this noise as one of their unique sound characterization (for instance – horn and alarm sound)

Brake noise – Brake noise remains a major concern all over the automotive industry regardless of efforts to reduce its occurrence. For instance, for decades brake squeal noise has been under investigation by automotive manufacturers due to consistent customer complaints and high warranty

costs, although in most cases this type of noise has little or no effect on the performance of the brake system.

Road vehicle vibration and brake noise can be classified according to its dominant frequency and its triggering conditions (such as decelerating or moving slowly while braking). Traditional categories are represented by judder, groan, moan and squeal, respectively corresponding to around 10 Hz, 100 Hz at very low vehicle speed (below 2 km/h), 100 Hz at higher speed (10-30 km/h) and more than 1 kHz vibration frequency phenomena [30].

Noises that reside in the range 100 to 1000 Hz are grunt, grind, groan and moan. This noise is produced by friction material excitation at the rotor and lining interface. Through the brake corner and coupling with other chassis components, the energy is transmitted as a vibratory response [31]. The low frequency squeal is generally classified as a noise having a narrow frequency bandwidth in the frequency range above 1000 Hz, but below the first in-plane mode of the rotor. This phenomenon referred to as ‘‘modal locking’’ that can be associated with frictional excitation coupled failure mode.

On the other hand, high-frequency brake squeal is described as a noise which is produced by friction induced excitation imparted by coupling resonances (closed spaced modes) of the rotor itself as well as other brake components. Typically, it is classified as squeal noise that occurs at frequencies above 5 kHz. High-frequency brake squeal is being considered as the most annoying type of noise because of its frequency range which affects a region of high sensitivity in the human ear.

Buzz, squeak, rattle and tizz noises - Buzz or tizz, squeak and rattle noise are indications of noise from structural vibrations and assemblies within the low frequency range and are categorized as structure-borne noise. Buzz or tizz noises are caused by high-frequency tactile vibration which means the sound wave emanating from the vibrating structure alone (such as that occurs

on the gear lever knob or noise from a tuning fork) and are relatively easy to find and cure.

Squeaks (which can be individual tick noises or sequences of ticks that sound like a squeak) are caused by relative motion between material pairs and these pairs can be buried deep within the fabric of the car interior (such as somewhere inside the dashboard assembly). When the static friction force is exceeded, the elastic deformation of the contact surfaces storing energy will be released [32]. Noise from vehicle suspension components, body panels and door hinges are typical examples of squeak. It is often noticed when the vehicle travels on bumpy road surfaces, where high suspension strokes are involved.

Rattle is noise because of the impact of one part on another and can be caused by loose fitting (and hard) interior trim items but also in the vehicle transmission line. The main causes of buzz, squeak and rattle (BSR) noise can be categorized as unsuited material pairs, structural deficiencies and poor geometrical alignment. For both squeak and rattle noises, the exciting force, which forces components to vibrate vertically is due mainly to the road surface [33].

Mechanical and Electrical Noise- The sound sources of modern road vehicles can be classified into three components, driving sound (sound generated through normal driving patterns and events), operating sound (sound generated through actuated components not related to driving), and generated synthetic sound (electronic warning / interactive feedback). The characteristic features of these sounds are dependent upon customer expectation and usage requirements [34]. Most of the mechanical and electrical noises are either operating sound or generated synthetic sound and sometimes known as secondary noises.

Manufacturers try to manipulate this “desirable” sound, especially as they generated synthetic or warning sounds as nice and as pleasant as possible

below irritation level, while maintaining a clear warning perception. Blinker indicator, seatbelt reminder, reverse gear, parking assistance signal and turn signal are needed to remind users about safety and provide a better and more comfortable to the driver (while meeting legal requirements).

On the other hand, operating sounds are focused on the reduction of the overall level of sound and elimination of high frequency metallic components. Motor operations such as electric sun roof, window regulator, self-locking, windshield wiper and HVAC produce their own noise level that can be problematic and annoyance to certain customer [35]. Subjective preference of window regulator sound quality is affected by band passes loudness and motor speed variations and customers tend to choose power window sounds with lower intensity levels, lower roughness which are low in fluctuation strength [36]. Noise from slamming a door, opening a door or even seat adjuster sounds can also emit unnecessary noise levels.

2.4 Vehicle noise path

Noise and vibration transmission to the interior of the vehicle from the source are generally referred as structure-borne or airborne paths. They are related to completely different mechanisms of energy transmission. Airborne noise paths in automobiles normally refer to sound generated outside the passenger cabin and transmitted through the vehicle panels to the interior space through the air medium. While structure borne paths are characterized by direct mechanical contacts through the structure to the panels on the surface of the passenger cabin where the energy is radiated as sound to the interior acoustical space.

In a common vehicle (like a car), experience shows that very often the structure-borne noise transmission path dominates at low frequencies (<200 Hz) while the airborne noise transmission path dominates above 500 Hz. In the mid-frequency range, both transmission paths have commonly the same level of importance [37].

2.4.1 Structure Borne Noise

The structure-borne path is a vibration transmission path, in which noise is emitted by the panels surrounding the internal cabin. The interaction between the tyre patch and the pavement is a common example of structure borne. Interaction between the road and tyre will generate vibration which is then later transmitted to the wheel and to the spindle. Next, the vibration energy from the spindle will go through numerous paths consisting of many different combinations of suspension components, chassis members and body panels. The dominant path may be different for different vehicles or a different operating condition.

Structure-borne noise tends to dominate the road noise from 300 to 500 Hz and might be important up to 800 Hz, for unibody automobile types depending on the source and the vehicle design. However, for a body on frame vehicle, the structure-borne noise may be dominant up to 300 Hz depending on the performance of the isolation system between the body and frame [38].

2.4.2 Air Borne Noise

Airborne sound transmission in vehicles is similar to the transmission loss behaviour in buildings. For road /tyre noise, the sound generated at the tyre spreads under the vehicle and is transmitted by airborne paths through the floor panels. Road noise also propagates around the vehicle body and is transmitted through windows, any leakage paths and passenger cabin panels.

Depending on the vehicle design, airborne noise can start to become important at frequencies from 300 to 800 Hz. Airborne noise tends to dominate the high-frequency band of road noise. Most wind noise is transmitted to the cabin through the airborne path normally through glass and panels.

2.5 Vehicle Noise Receiver

Vehicle interior noise perceived is one of the most important factors in a customer's determination of the quality and durability of the vehicle. There are many different reasons that affect the user's evaluation on the quality of automobiles and it is a very subjective decision. Therefore, car manufacturers depend on juries, experts or customer perceptive (either selective or random respondent) to determine their target goal.

Therefore, car manufacturers need to design a vehicle with a low interior noise by equipping it with absorption and insulation material, while at the same time, they also need to produce a lighter car that has a good fuel efficiency and is more environmentally friendly than the competition. The car should be well insulated but not all the sound should be absorbed as each car topology and brand has its own identifying sound- it is part of its appeal and must be carefully safeguarded [39].

2.5.1 Developing Acoustic Target

One of the crucial parts of designing and producing the best vehicle sound and vibration controlling package is developing the acoustic target. There are abundant solutions for vehicle noise control. In general, they can be controlled either at the source, along the propagation path to the receiver or within the receiving environment and normally each manufacturer has their own preference of where to put the most effort. To effectively utilize the sound package treatments, normally they should know how the acoustical material works, the importance of the path where the material used, how to judge the performance and some more [8]. This is to make sure the manufacturer selects the correct material and system for the vehicle. In doing so, manufacturers perform extensive benchmarking studies under various operating options and conditions.

Finally, is to ensure the sound package that has been developed is the best in term of value: cost, weight, durability, functionality, recyclability, environment impact, performance and ergonomics. The significant effort in developing the sound package treatments is to achieve the best suitable balance of performance between several of noise sources and operating condition combinations.

2.5.2 Sound Quality

The automotive acoustics designer recently discovered that “quieter” does not necessarily coincide with “more pleasant”. Analysis of acoustic signals alone is not necessarily sufficient to identify the level of sound quality inside the car [39]. Vehicle manufacturers are increasingly using psychoacoustics to better correlate their vehicle quality to customer perception.

In psychoacoustics, the actual sensations of human hearing are not being reflected by measurable physical quantities, such as the sound pressure. Several psychoacoustic parameters, such as the A-weighted sound pressure level, sharpness, loudness, fluctuation strength, roughness, annoyance, and many more have been proposed to quantitatively relate sound stimuli to human sensations [40].

However, every individual has their own concept of preferential sound and others depending on their cultural background, expectations, interests, emotions mood. In order to get these data, jury or expert testing are commonly used and then translated into measurable values. Mostly, for time and cost saving, many attempts are carried out to correlate the statistical data from the jury session with psychoacoustic metrics to obtain and define the specification of the sound that meet the customer expectation.

2.6 Introduction to Current Automotive Sound Package

The interior noise in the cabin spaces of vehicles is mainly caused by the engine, tyre/road interface, and wind/structure interaction. The strength of each source varies for every vehicle depending on the path, and vehicle operating conditions such as speed. Various well-known techniques are often being used in order to reduce airborne and structure-borne noise from reaching the vehicle's occupants, including (i) increasing structural damping, (ii) refining the transmission loss of body panels and windows, (iii) increasing the use of sound-absorbing materials in the engine, passenger, and luggage compartments, and (iv) isolation of the vibrating mechanical components [41].

2.6.1 Barrier Material

The acoustic isolation capability of the vehicle's panels and windows is very important for NVH performance, as most of the noise sources are external to the vehicle's cabin. This performance is measured by the transmission loss of the given panel or component. The performance of the whole vehicle is usually expressed in terms of acoustic transparency of the cabin, measuring the internal sound pressure level for some predefined positions of external noise sources [14]. This performance will depend on the transmission loss of all the components of the cabin, including panels, glass windows, acoustic treatments, seals and any other possible paths of transmission. Figure 2.8 shows a typical position where barrier materials are utilized in an automobile.

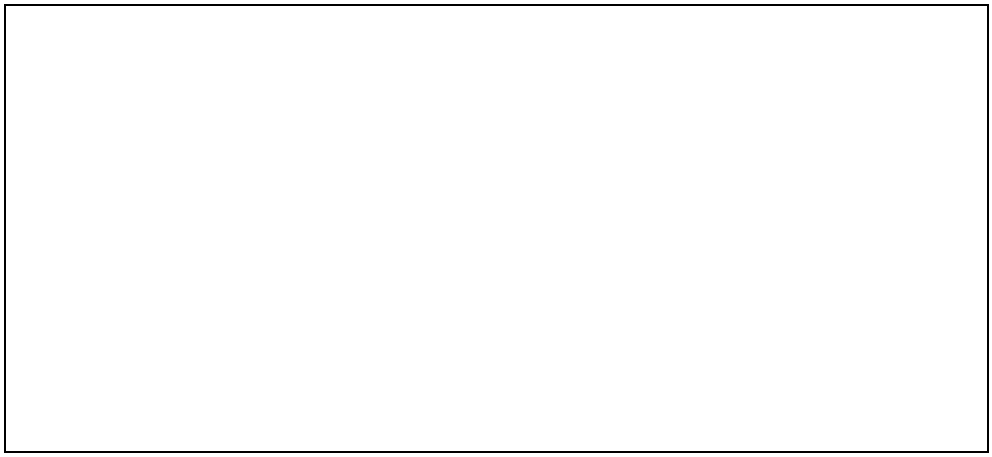

Figure 2.8 Image of typical locations in an automobile where ‘‘barrier’’ materials are utilized (taken from ref.[41]).

Panel/ Barrier

The sound insulation package often consists of a barrier and a decoupler. The barrier is a material that stop sound propagation from one area to another. These barriers are normally a limp, massive, and nonporous material and generally lay against a body panel (steel in most cases) of the car with the decoupler against the panel. Thus, the barrier and decoupler will form a double wall system with the body panel. The techniques in this thesis can be used to obtain the sound radiation coefficient for a plate with barrier coating.

Very common solutions in vehicle applications are made of a double wall composed of the metal panel and a so called ‘heavy layer’ (usually bitumen or heavy rubber), separated by a fibrous absorbing material: in this way the system works with a high level of transmission loss. Frequently the barrier is formed from Ethyl Vinyl Acetate (EVA), Poly Vinyl Chloride (PVC), or Thermo Plastic Olefin (TPO) materials (surface density 1.2-7.3 kg m^{-2}) glued with decouplers include cellular and fibrous (density ranges 64-80 kgm^{-3}) [42].

The important property is the behaviour of double walls. It is possible to obtain an equivalent transmission loss that is much higher than the summation of the transmission losses of the two separated walls. Also, by

filling the air gap with sound-absorbing material, it may further increase their performance. However, good care has to be taken to avoid resonance phenomena in which a double wall system adds to the critical frequencies of the two partitions with a third resonance, called the double wall resonance, at which the transmission loss shows a strong reduction. Figure 2.9 shows comparative results between single and double wall.

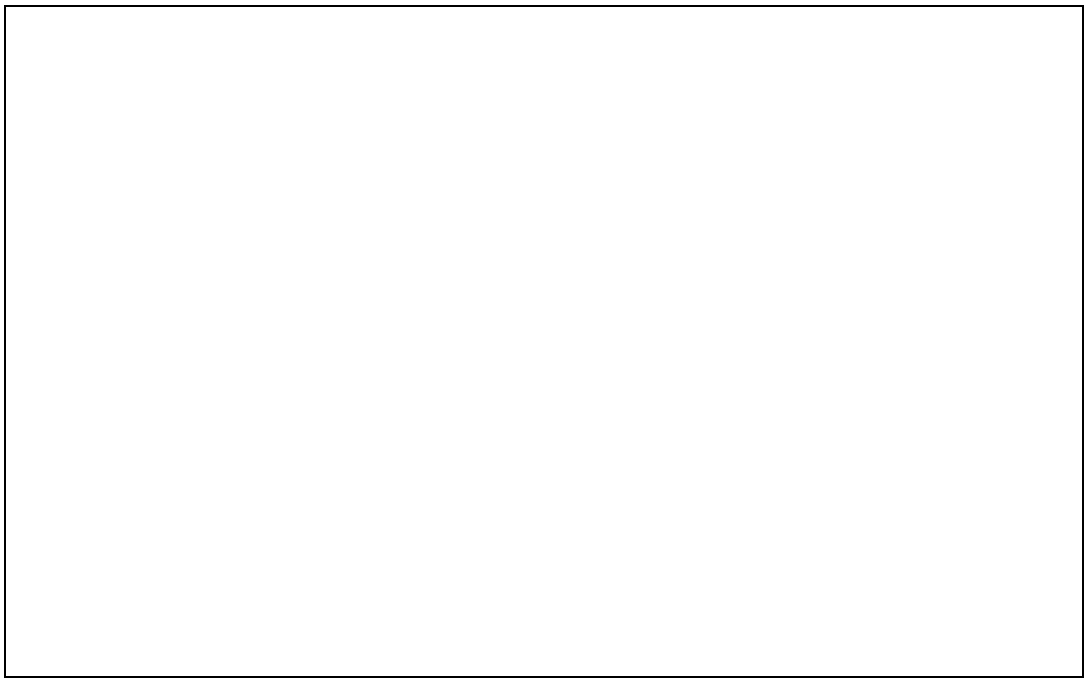

Figure 2.9 Image of Qualitative STL Performance of Single and Double wall Constructions (taken from ref.[43])

Acoustic barriers in cars are commonly applied to the dash mat, firewall, floor carpeting, and rear seat back strainer. Barrier type dash mats provide a barrier with a high acoustic reflection yet little on interior absorption. Saeed et al., proposed a new generation of dashmat which was constructed of an absorptive layer, a barrier, and another absorptive layer that can perform by blocking and absorbing the powertrain noise as well as the vehicle background noise [44]. From his finding, the new dashmat has a better noise reduction value in the frequency range from 500 to 8000 Hz compared with the normal dashmat.

Shivle et al. also suggested modifications to the firewall by introducing foam, heavy layer and non-woven insulated material as filler for acoustic insulation. They found an improvement in the noise reduction by adding foam and the heavy layer by around 1.5-2 dB in a frequency band of 400 Hz- 1000 Hz and around 4-8 dB in a frequency band of 1250 Hz to 8000 Hz as compared to the bare firewall [45]. However, he also mentioned that maybe the weight will become a drawback since it will increase the total weight.

Glass Window

Glass windows on vehicles cannot be treated with added mass or double walls (double glazing is not suitable for vehicle applications), and their coincidence frequency is in a frequency range (near 3000 Hz) where the contributions of noise sources are substantial [14]. These make it as the easiest way for noise to penetrate and difficult to control.

Callister et al. ran studies on different types of window for finding the best option for restraining transmission of noise. He ran the bench-scale flow noise tests, full scale wind tunnel flow noise tests, and acoustic tests were performed for six types of windows. In his research, he found the laminated side window design would provide acoustic improvement compared to the current production side window. Yet, the other designs also showed acoustic benefits but were less desirable because of cost, weight, or manufacturability reasons [46].

2.6.2 Sound Absorption Material

Noise absorption is the absorption of the energy associated with the acoustic waves for the purpose reducing noise. This is possible thanks to the sound absorption properties shown by some materials. Noise absorption materials are common use in current vehicle especially to cater medium to higher frequency of noise attenuated by air borne.

To design an acoustic absorbing treatment, it is essential to have a good knowledge of the physical properties of the materials: by optimizing their flow resistance, porosity, density, tortuosity, etc. It is possible to optimize the acoustic absorption of a given treatment in the selected frequency range according to the defined targets, keeping the weight to the minimum required.

Figure 2.10 Image of (a) the absorption of sound by vehicle interior trim [47], (b) typical locations in an automobile where sound-absorbing materials are utilized (taken from ref.[41]).

The seats and the headliner absorb most of the sound because of their large surface areas and their suitable flow resistance (neither too high so as to appear reflective, nor too low so as to appear acoustically transparent) [47]. Figure 2.10 (a) show an estimation of the proportion of absorption of sound by vehicle interior trim while figure 2.10 (b) illustrated typical locations of sound absorbing material in automobiles.

Nowadays, with the demand from customer and society, industry needs to address issues related to fuel consumption, vehicle emissions, consumption of non-renewable materials, and recycling of waste materials. Many researcher have tried to promote natural fibres as absorption material in automotive applications [48][49]. Parikh et al. suggests to use non-woven natural fibre as a floor covering in vehicle to control interior noise. Floor coverings using natural fibres (kenaf, jute, waste cotton, and flax) in blends with polypropylene (PP) and polyester (PET) were developed as carded needle-punched nonwovens. Boyer in his paper gives a good overview of recent advances in new acoustic materials based on recycled and sustainable sources

for “environmental” vehicle sound packages that address NVH and trim acoustics requirements [50].

Seat

In order to maximise the total absorption of the cabin, most of the time absorbing treatments in cars are often applied to all the available surfaces of the cabin. The most important part has to be taken are the seat since it will absorb half of the total absorption in the passenger compartment. For a porous material to absorb sound, the thickness of the material should be large relative to the wavelength of the sound. Typically, the thickness needs to be 1/4 of the wavelength to achieve effective absorption.

To optimize the performance of seats essential parameters are seat fabrics/leathers, foams types used in cushions etc [51]. A seat cover is typically a laminate (i.e., face material bonded to slab foam). Chen P in his research found cloth seats have superior noise absorbing capability compared to leather/vinyl seats and also perforation on leather/vinyl can improve the noise absorption of leather/vinyl seats.

Later, McMullan A. et al. investigated various seat cover materials to determine their acoustic characteristics on the same polyurethane foam sample. They found that fabrics with lower airflow resistivity and specific airflow resistance values have greater average absorption coefficients. Furthermore, the vinyl and leather fabrics without perforations have little to no absorption while those with perforations are better but are still generally out-performed by most cloth seat fabrics [52]. Moreover, Jain in his research also found fabric seats have superior noise absorbing capability compared to leather/vinyl seats. He also looks into effects of various seat configurations on operator ear Sound Pressure Levels (SPL) at the driver/passenger ear location inside a typical car cabin studied using the Boundary Element Method (BEM) simulation [53].

The selection of the materials for the seats and seat cover is very significant for the entire acoustic behaviour of the cabin. Generally most of the seats are using polyurethane foams. It has a high sound absorption coefficient (0.8 – 1.0) in high frequencies ranging from 300 to 10000Hz while it is found to be low (0 to 0.5) at low frequencies (10 to 200 Hz). Gayatri proposed new polyurethane based porous composites rising polymerization of polyol and diisocyanate in the presence of fillers such as nano silica, crumb rubber and nano clay. The sound absorption coefficient of filling PU foams is found to be increasing from 0.5 to 0.8 with increasing frequency from 100 to 200 Hz at higher content of the fillers employed [54].

Headliner

Another important component for absorption is the headliner. It must be carefully designed from the point of view of acoustic absorption because of its large surface area. The area for it can reach up to 25% of the total absorption of the passenger compartment. Qian has mentioned in his paper that the typical headliner outer facings must not only have a good appearance, but should also be sufficiently permeable, to allow air to pass through to the porous layers behind and the adhesives necessary to bind layers together. In addition, it also should not block pores that can impede airflow, reflecting sound, and thus weakening absorption that might be offered by subsequent layers [47]. In his paper, he studied the effect of different headliners on random incident absorption; in vehicle reverberation time and also how different manufacturing processes will consequently alter the noise absorption value.

Boyer mentioned a thermo-formed carrier with a 100% PET substrate, soft touch foam (acoustic enhancer), PET face fabric and PET non-woven scrim can be fully recycled following shredding and pelletizing. It can also incorporate PUR chip-foam blocks, moulded and plain, as absorbers and sealers. He claimed this eco-designed product offers superior sound absorption characteristics [50].

2.6.3 Damping Material

Damping materials are commonly more effective at reducing structure-borne vibration rather than at decreasing the airborne sound transmitted through the panels. Spray-on damping material is easiest to apply on the damping approaches, but a constrained damping layer comprised of a viscoelastic layer constrained by a thin surface layer normally provides higher damping for the same weight or less weight through shearing action in the viscoelastic layer [41].

Water-based spray-on damping materials are also used in automobile manufacture. Among the advantages of this technique is the area covered by it where it has the possibility to spray on the most difficult area to reach such as wheel housing if sprayed robotically. It is believed that the use of the body and floor panel damping is effective mostly on reducing structure borne interior automobile noise in the 100- to 500- Hz range.

Damping material applied to the radiating panels also plays a major part in dropping the vibration levels. Although damping material mass may also influence vibration levels, the damping loss factor has the primary effect in controlling vibration levels. Figure 2.11 below shows the location where treatment for damping is often applied.

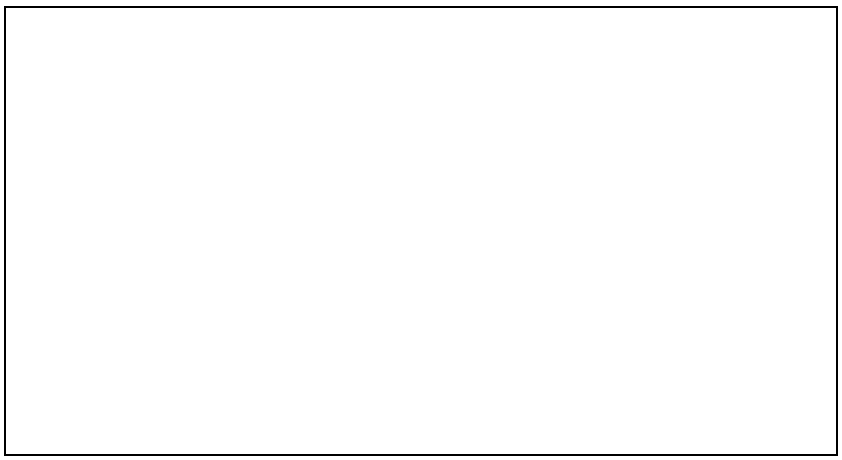

Figure 2.11 Image of Locations in a typical automobile where damping treatments are often applied (taken from ref.[41]).

Gur in one of his papers showed that increasing dash damping loss factor value from 4% to 25% increases predicted vehicle engine noise reduction by up to 1.7 dB [55]. On that paper, his study focused on only the dash sheet metal and it's damping properties. Da Silva et al. have compared the characteristics of two materials of floorpan treatments (deadeners): an asphalt melt sheet (bitumen pads) and a waterborne material (LASD - Liquid Applied Sprayable Damper - AcusticCol) as damping material in their intensive paper [56]. They found, on certain criteria, LASD is superior compared to asphalt melts sheet.

2.6.4 Other component's Material

Seals mainly on doors and windows are very important for the reduction especially from aerodynamic noise. A very intensive care has to be taken on geometric tolerances and on the dynamic behaviour of compressed seals to reduce possible noise transmission through them, both with and without net flow. There are two circumstances related with this, in the first condition, the aerodynamic pressures are strong enough to deform the sealant and it becomes detached from the door or body surface, allowing an airflow passage. As a result, this noise source will behave as a very efficient monopole source. In the second condition, the aerodynamic pressures acting on the seal surface make it move and the vibrating seal surface on the interior side acts as an acoustic source [14].

Rocha in his paper has investigated the correct balance between the mass added to treat vehicle panels and sealing content [57]. His method is using two steps to reduce the interior noise which is applying noise treatments in potential weak areas and improving sealing (including the addition of secondary bulb seal and expandable foam baffles).

Lilley on his studies looks at different innovative materials applied to the body structure, their design and placement of them to support a quiet interior; (baffles, sealers, barriers, dampers and structural reinforcements)

with the emphasis on finding a low cost, low mass and highly/optimized performance solution [58].

2.7 Techniques in Vehicle Noise and Vibration Analysis

2.7.1 Statistical Energy Analysis (SEA)

Statistical Energy Analysis (SEA) was first applied in the automotive industry to study vehicle interior noise a long time ago. SEA was originally developed in the 1960s as a technique of predicting the high-frequency response of dynamic structures. Since then, it has been developed as a tool for design and development of sound package in automobiles [59].

The majority of automotive OEMS and suppliers have now been using SEA for airborne interior noise prediction as part of production modelling. Normally any model will comprise of major structural and acoustic components that are important for the transmission, along with the sound package, leakage paths and pass-through [60]. In principle, SEA can also be used to model structure-born noise in vehicles.

Advanced modelling approaches for airborne SEA are still being improved, not like the basic method which is well established. However, more comprehensive developments of sound packages are now possible and models of poro-elastic materials continue to advance. For instance, the addition of explicit perforated layers and resistive screens to sound package definitions [61]. Moreover, predicting the interior acoustic field surrounding a vehicle with the use of an improved method is one of the most interesting areas for researchers. One of them is the use of Fast Multipole Boundary Element Method to define the inputs to airborne SEA models as discussed in [62].

The Hybrid FE-SEA method [63],[64],[65] (for rigorously coupling Finite Elements and SEA in the same model) also has an application in improving existing airborne SEA models; sometimes it is referred as a Hybrid SEA-FE

methods. One of the method examples is by including and updating the transmission loss of complex panels and pass-through in a system level SEA model using information computed from local Hybrid models [66]. This approach provides a rapid approach to improve “SEA acoustics and trim” to the existing FE structural models. In addition, for detailed FE models of the body structure, this approach can also be used to couple SEA descriptions of the interior cavities and sound package. This provides a “quick and approximate” technique to model trim without needing a complete geometric description of the sound package.

Musser, in his studies had performed an acoustic analysis with SEA relative to cost and weight. Considerations began with a validated full vehicle SEA model to find the solutions for the best-performing sound packages relative to cost and weight considerations [67]. Musser in another paper also discussed the assumptions used to generate a typical model of a vehicle cabin interior and surrounding structure. He also mentioned an SEA model can account for the side-to-side, front-to-back, and upper-to-lower differences of interior vehicle SPL by sectioning the vehicle cabin into several acoustic spaces [68].

2.7.2 Transfer path analysis (TPA)

Transfer path analysis (TPA) is a simulation-based or test-based procedure which allows outlining the flow of vibro-acoustic energy from the source to a receiver location through a set of known (either) structures and air-borne transfer pathways or both of them. Experimental transfer path analysis (TPA) is a technique, for estimating and identifying individual low-frequency noise or vibration contributions through different structural transmission paths. TPA can also be used at higher frequencies (above 150-200 Hz) in road vehicles. However, it may be practical to introduce a different formulation based on the response statistics of multimodal vibro-acoustic systems with strong modal overlap [69].

On the basis of the interior structure-borne noise transfer path identification, Lingyuan et al. proposed a novel method to control the interior noise by controlling the structure-borne noise transfer function of the subsystem. In his studies, the noise was caused by engine excitation. Firstly, his method utilizes the Finite Element method to establish the dynamics model coupling the power train-body subsystem. Then it will predict the vehicle interior structure-borne noise through the mounting system to the body [70].

Plunt in his article discussed the use of experimental transfer path analysis (TPA) to find the optimized solutions of NVH problems in vehicle development stages. Four practical case histories have been discussed to demonstrate how TPA, FE models and practical experiments can supplement each other efficiently for finding the optimum and attribute-balanced solutions to complex NVH issues during the development process [71].

2.7.3 Finite Element/ Boundary Element Methods

Finite Element models can provide a good way to describe the interior noise at the lower frequencies. Traditional low frequency FE models typically focus on the body in white. That type of model can be used to designate low frequency powertrain/suspension/body interaction. It is also often used to design isolation systems to avoid modal line-up and impedance matching. Traditional low frequency FE is not particularly well suited to predicting interior noise in a fully trimmed vehicle [60], partially due to the variability in boundary conditions inherent in assembled models. More explanation about it can be found in the paper.

Describing the sound package explicitly using a series of shell and volume poroelastic elements is one of basic approach. The impedance of the sound package is accounted for explicitly when coupling the structural and acoustic meshes. The development of automated mesh projection algorithms for detecting the coupling surfaces between non-compatible structural, acoustic and trim meshes is very important to this method.

Shorter et al. has reviewed a number of methods that have been proposed for predicting the vibro-acoustic response of an automobile in the mid frequency range [72]. He classified FE as a low frequency deterministic approach and has some of the disadvantages for mid frequency such as sensitivity of response not accounted for in analysis, difficulty in interpreting results and computational expense.

Courtois, T et al. proposed a methodology for the efficient inclusion of the effect of trim parts into the FE models. The use of virtual NVH development has been presented, together with its implementation and full integration into commercial FE solvers [73].

According to Georgiev, normally the existing full vehicle vibro-acoustic models have more than one million degrees of freedom. It consequentially will take a long time to be developed and solved. In this regard, Boundary Element Methods have been considered as a valuable alternative because via the boundary surface integral representation, it can decrease the dimensions of the problem, in addition to only needing to mesh the surfaces, rather than the volumes. Subsequently, the final system of equations is much less than an equivalent FEM model. However, by using the BEM method, the coefficient matrix can be fully populated and is non-symmetric. As the result, BEM technique can be slower to solve [74].

2.7.4 Active Noise Control

Several practical applications, for instance the engine or exhaust noise control in vehicles, ships, turbo machinery, aircraft and vibration isolation systems have used the feed forward strategy in active noise and vibration control [75].

Yoon Hee Lee has studied an Active Noise Control system for passenger vehicles. The system was designed to cancel the engine booming noise which

has been implemented using a digital signal processor based control unit including four microphones and two actuators (speakers). Their study shows a reduction of 10 dB in engine booming noise at 2000-3000 RPM of engine speed, which is the normal standard cruise range of commercial cars [76].

On the other hand, Schirmacher et al. have discussed some practical aspects of implementing active noise systems on their research paper. They had suggested to consider some uncertainty and variations of the acoustical environment either to be measured and / or modelled [77]. Emanuele Bianchini in his research has studied the potential of active vibration control for automotive like panels. He claimed a reduction of 10 to 15 dB was obtained over the frequency range of interest [78].

Next, in order to decrease not only the booming noise but also the noise and the vibration over a wide frequency band, Togashi has established a new control method for the comfortable vehicle interior space purpose. The method which by modifying Least Mean Square algorithm can determine the feedback gain according to numerous circumstances [79].

Stephan Tewes in his doctorate thesis investigated a new active structural acoustic control (ASAC) concept based on an active trim panel suspension. However, the research was focused on an aircraft application [80]. Insoo Kim also in his paper presented a method for controlling the sound transmission actively through an aircraft trim panel by using a hybrid feedforward / feedback control technique [81]. Yet, both of the knowledge is not limited to the aircraft application only.

2.7.5 Digital Image Correlation

Today, optical full-field measuring systems are progressively being utilized as a part of examination and industry as advancement and outline instruments for enhanced portrayal of materials and parts. One of the techniques is the Digital Image Correlation (DIC) method which is widely used to examine a

diverse range of material specimens including examining strain in materials testing, crack tip and crack propagation studies, identifying damage development in composites, structural deflections and dynamic vibrational analysis [82].

Images taken from a stereo pair of charge coupled device (CCD) cameras can be used to determine surface geometry and displacement in three dimensions of any object whose surface has had a contrasting speckle pattern applied to it. This non-contact full-field technique can take measurements at thousands of points on the surface of an object in a single snapshot. Deformation measurements with very high resolution are possible even under the presence of large deformation amplitudes and macroscopic rigid body movements, since the system determines the absolute position and displacement of the object in space [83].

A high speed camera is normally used for the DIC purpose when dealing with the higher frequency of movement or vibration. Thorsten on his paper present examples of the analysis of harmonic vibration and transient events from material research and industrial applications by using high-speed cameras (Nanosense MK III) with 1280 x 1024 pixels resolution. The maximum frame rate at full resolution of these cameras is 1000Hz [84]. Then, Thorseten et al. also measured the mode shapes of a car bonnet frame structure made out of fibre reinforced thermoplastic composite material, excited by single frequency excitation using a shaker. The results are compared with modal analysis based on accelerometer and simulations based on the CAD model using FE analysis techniques [85].

Helfrick presents some preliminary results for the test/analysis/correlation of data measured using the DIC approach along with traditional accelerometers and a scanning laser vibrometer for comparison to a finite element model dryer cabinet panel [86]. Theunis in his thesis, explores more use of DIC in vehicle dynamics application especially on measuring side-slip angle, longitudinal tyre slip ratio and fidelity terrain profiles [87]

2.8 Conclusion

This chapter contains a discussion on the general literature survey from the type of noise in automotive vehicles, the noise transfer path and current automotive sound packages. The final part for this chapter is covering a few techniques in noise and vibration refinement including the DIC which will become the main method in this thesis. DIC is simple to use and cost effective compared to other techniques such as speckle interferometry, or laser Doppler vibrometer experiments and is more accurate and objective than manual measurement methods, leading to a huge range of possible applications. Furthermore, there hasn't been sufficient development of vibroacoustic experimental methods using DIC and with the advances in methods, the use of low speed camera in the DIC procedure instead of a high speed camera can result in lower costs. In order to achieve that potential, the DIC have been chosen and the usage of it to be explored in this research. More detail on the procedure and investigation of the vibration response of a typical automotive plate structure using the DIC will be discussed later on chapter 4.

CHAPTER 3
STRUCTURAL PROPERTIES IN AUTOMOTIVE TYPE PANELS

3.1 Introduction

This chapter covers the structural properties of a single panel in terms of vibration properties and acoustics radiation, especially on the experiment stage before comparing it with theoretical and Finite Element Analysis (FEA). It begins by discussing the classical solution of the natural frequencies and mode shapes for a single rectangular plate. A flat single rectangular plate was used as it is commonly representing an automotive type panel. The theoretical calculation includes details on three different edge boundary conditions which are clamped, simply supported and a free condition for comparison purposes on different boundaries conditions. Next, the point mobility experiment was carried out and the experimental result was compared with the theoretical value. After that, discussions continue with the results from numerical / finite element solutions for a single plate with clamped-clamped boundary condition, in order to understand what a typical numerical accuracy might be. This resonance frequency result from point mobility will be used to generate the source of frequency later for sound power experiment and DIC measurement in Chapter 4. The final part in this chapter is discussion of sound power to measure sound radiation by using the sound intensity method. This sound power value based on modal excitation will be use then as validation purpose that will be discussed more in Chapter 5.

3.2 Classical Solution

A single flat rectangular plate was chosen as the mathematical calculation for a rectangular plate is already well known and the plate also can frequently represent the automotive type panels. Hood, bonnet, roof and the automotive body generally is a flat plate and covers a big area for an automotive vehicle. For a rectangular plate having sides with lengths *a* and *b* as shown in figure 3.1 and

thickness h, the vibration form must satisfy the boundary condition and also the plate equation [88] in equation 3.1.

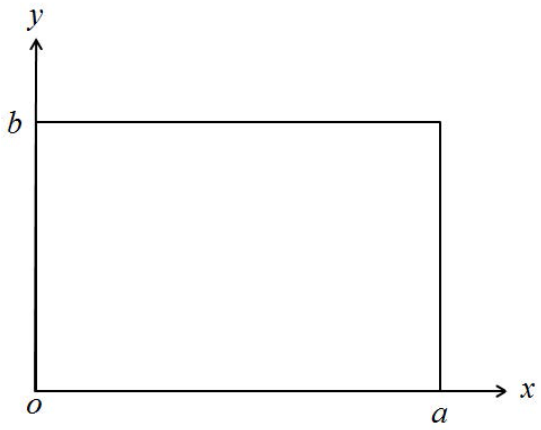

Figure 3.1: Dimension of rectangular plate

$$\frac{\partial^4 w}{\partial x^4} + 2\frac{\partial^4 w}{\partial x^2 \partial y^2} + \frac{\partial^4 w}{\partial y^4} + \frac{12\rho(1-v^2)}{Egh^2}\frac{\partial^2 w}{\partial t^2} = 0 \qquad (3.1)$$

Where ρ is plate density, v is the Poisson ratio and w, the displacement at any point (x,y) at time t, g is gravity is given by

$$w = Wsin\,\omega t = AX(x)Y(y)\sin\omega t \qquad (3.2)$$

With A is an amplitude coefficient. Warburton [89] presents the first comprehensive list of solutions for rectangular plates for a variety of boundary conditions. Using the Rayleigh method, the deflection functions of the plate can be presented as the product of beam functions [90]

$$W(x; y) = X(x)\,Y(y) \qquad (3.3)$$

where *X(x)* and *Y (y)* are the fundamental mode shapes of beams having the boundary conditions of the plate. The choice of beam functions in Eq. (3.3) satisfies almost all the boundary conditions for the plate. In this report, solutions for clamped boundary conditions are discussed, but a complete list of solutions for

all the remaining boundary conditions can be found in Warburton's paper [89]. Here the clamped boundary condition cases are used to demonstrate the analytical analysis of a flat plate shown in Fig. 3.1 as summarised by Warburton.

1. Clamped at *x=0, x=a*

$$X(x) = \cos\gamma_1\left(\frac{x}{a} - \frac{1}{2}\right) + \frac{\sin\frac{\gamma_1}{2}}{\sinh\frac{\gamma_1}{2}}\cosh\gamma_1\left(\frac{x}{a} - \frac{1}{2}\right); (m = 2,4,6 \ldots.) \qquad (3.4a)$$

$$X(x) = \sin\ \gamma_2\left(\frac{x}{a} - \frac{1}{2}\right) + \frac{\sin\frac{\gamma_2}{2}}{\sinh\frac{\gamma_2}{2}}\sinh\gamma_2\left(\frac{x}{a} - \frac{1}{2}\right); (m = 3,5,7 \ldots.) \qquad (3.4b)$$

With the value of γ_1 and γ_2 are obtained as roots of

$$tan\ \frac{\gamma_1}{2} + \ tanh\ \frac{\gamma_1}{2} = 0 \qquad \text{and} \qquad tan\ \frac{\gamma_2}{2} + \ tanh\ \frac{\gamma_2}{2} = 0$$

Then, similarly, the function Y(y) can be obtained by replacing x with y, a with b and m with n in equations (3.4a) and (3.4b) for boundary conditions at y=o and y=b for clamped boundary condition. The terms m and n are the number of nodal lines in the x- and y-direction.

3.2.1 Natural frequencies of a rectangular plate

Equation in 3.3 can provide solutions where consistent sets of conditions are applied for example all clamped (equation 3.4), however when mixed sets of condition are implemented it is necessary to use alternative formulation. Warbutton has rearranged and simplified the equation to calculate the natural frequencies. The natural frequencies for different boundary conditions of the rectangular plate can be calculated by using the following equation 3.5 [89]:

$$f_{ij} = \frac{\pi}{2}\left[\frac{{G_x}^4}{a^4} + \frac{{G_y}^4}{b^4} + \frac{2J_xJ_y + 2v\left(H_xH_y - J_xJ_y\right)}{a^2b^2}\right]^{1/2}\left[\frac{Eh^3}{12\gamma(1-v^2)}\right]^{1/2} \quad (3.5)$$

with i and j = 1,2,3

Where γ is the mass per unit area of the plate and the coefficients G_x, H_x, and J_x can be determined from the Table 3.2 with their boundary conditions. Likewise, the remaining G_y, H_y and J_y can be determined by replacing x with y. The automotive-type panel used for the preliminary study is a rectangular plate and the dimensions and material properties for the panel are shown in Table 3.1 below.

Table 3.1 Dimension and material properties of the panel used for theoretical analysis.

Length (a)	297 mm
Width (b)	198 mm
Thickness (h)	1.2 mm
Young's Modulus (E)	2.05 x 10^{11} N/m^2
Poisson's Ratio (v)	0.27
Density (ρ)	7817 kg/m^3

Table 3.2 Coefficients describe in equation 3.1.

Boundary Condition	**Mode, m**	**G_x**	**H_x**	**J_x**
Clamped-Clamped ***(CC)***	1	1.506	1.248	1.248
	2	2.5	4.658	4.658
	m *(m>1)*	$m + \frac{1}{2}$	$\left(m+\frac{1}{2}\right)^2\left[1 - \frac{2}{\left(m+\frac{1}{2}\right)\pi}\right]$	H=J
Simply Supported-Simply supported ***(SS)***	1	1	1	1
	2	2	4	4
	m	m	m^2	H=J
Free-Free ***(FF)***	1	0	0	$12/\pi^2$
	2	1.506	1.248	5.017
	m *(m>2)*	$m - \frac{1}{2}$	$\left(m-\frac{1}{2}\right)^2\left[1 - \frac{2}{\left(m-\frac{1}{2}\right)\pi}\right]$	$\left(m-\frac{1}{2}\right)^2\left[1 - \frac{6}{\left(m-\frac{1}{2}\right)\pi}\right]$

Reference : R. D. Blevins, Leissa [90][91]

3.2.2 Theoretical Result

The analytical approach to solving the field problem directly is a classical method undertaken by forming governing differential equations based on

fundamental principles of science. It can be divided into two types of solution which are exact solutions or approximate solutions. Most of the time, exact solutions are only applicable for simple cases either in geometry, boundary conditions or loads and even then often require some level of approximation or simplification. For approximate solutions, it is desirable to resemble real life engineering problems through the use of simplified geometric shapes, ideal boundary conditions and loads.

The natural frequencies for three cases; clamped-clamped, simply supported-simply supported and free-free boundary conditions for the simple flat panel are calculated using equation 3.5 previously shown. Results from the theoretical calculation are shown in Table 3.3 which indicates the calculated natural frequency for three different boundary conditions with their respective mode shape.

Table 3.3 Comparison theoretically calculated natural frequency (in Hz) of the test panel under different boundary conditions (note for free-free condition frequency is arranged ascendingly according to mode)

		Frequency		
m	n	Simply Supported	Clamped	Free-free
1	1	106	203	72
2	1	205	313	164
1	2	328	497	223
3	1	369	501	299
2	2	426	601	353
3	2	590	775	521
4	1	599	759	495
1	3	697	940	514
2	3	796	1042	651
4	2	820	1023	736

3.3 Point Mobility Measurement

A point mobility measurement is a transfer path technique that measures and compares the input signal and output signal, in this case, the ratio of the acceleration of the plate normal to the surface with the input force (again, normal to the surface). A thin flat panel is used to represent the type of automotive-panel found in floorpan or door panel structures.

To match the boundary conditions of the analytical results and achieve a consistent and representative baseline measurement, it is necessary to construct a jig to hold the plate in place. In order to achieve the clamped boundary condition; the experimental panel for the preliminary study was placed inside a metal frame, which was initially designed and used in a previous PhD research [92], details of the test rig are presented in figure 3.2. However, the rig was iteratively modified by increasing the number of bolts to achieve as close as possible a clamped boundary condition. The modifications include increasing the number of bolt that connected between upper frame and lower frame from 16 bolts to 28 bolts. The bolts were added in order to achieve as close as possible clamped boundary conditions to avoid other type of boundary that may lead to changing the resonance of the plate.

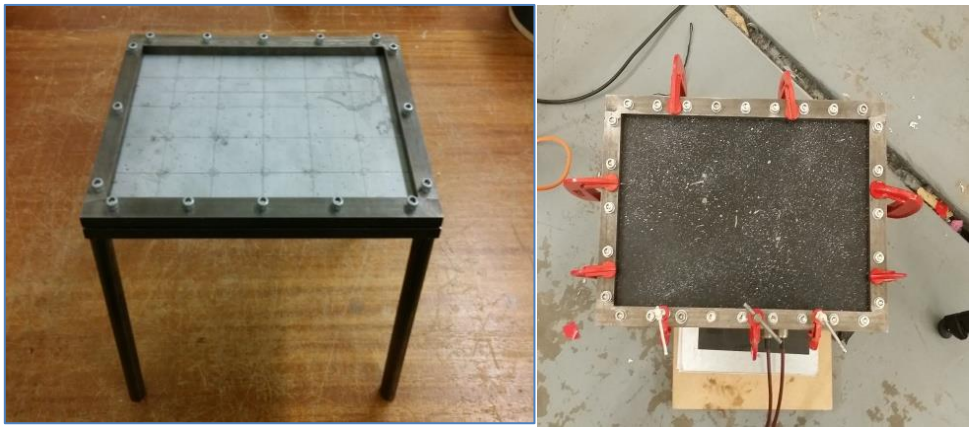

Figure 3.2 (a) Test rig used to achieve a clamped boundary conditions- before 16 bolts (b) –after 28 bolts with additional 9 G-clamps.

This experience partly shows how difficult it is to obtain an exact clamped boundary condition. Despite the presence of a lip at the plate edge, clamps and bolts applying an out of plane distributed load, an academically perfect clamped condition is unlikely to be formed. Further descriptions are therefore provided.

The test panel was placed between the two sub-frames and clamped using 28 bolts. The lower sub-frame has grooves around its periphery to firmly hold the surface of the panel groove. The upper sub frame is then placed over the panel and clamped with the help of bolts applying a normal pre-load. Detail of the original test rig can be seen in figure 3.3.

Nevertheless, for simulation and theoretical calculation, the width of the groove for each side was taken into consideration. Thus, originally the panel size was 307mm x 208mm, but the effective area that being calculated was 297mm x 198mm with 5mm groove for each side.

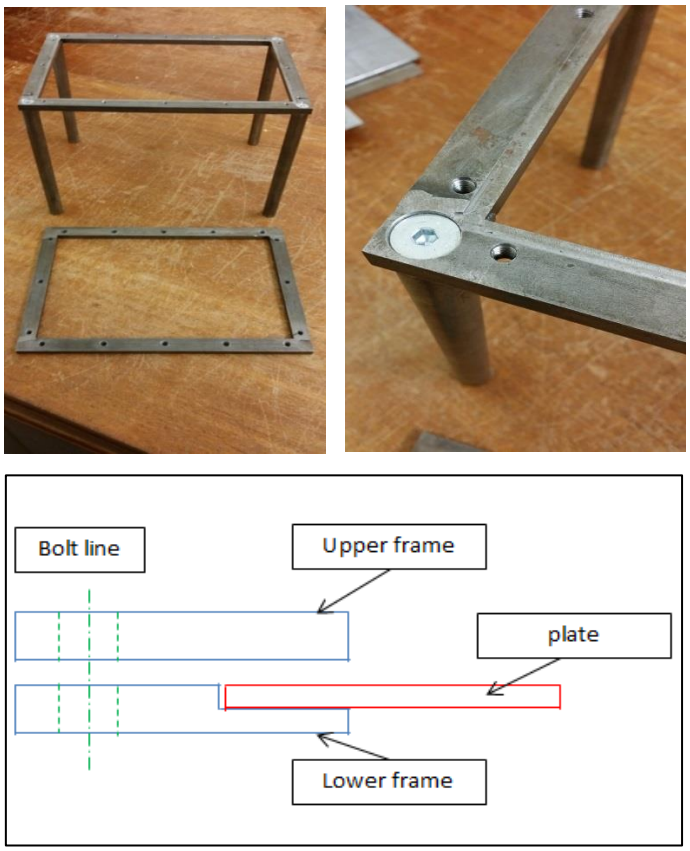

Figure 3.3 Two sub-frames used (with section view) as the test rig with grooves can be seen in lower sub-frame.

The panel is excited over the frequency range (white noise) of 0 to 1250 Hz using an electrodynamic shaker with an input signal of broad-band white noise at the bottom side of the measured panel and the resulting acceleration normal to the plate surface measured with an accelerometer placed on the upper side of it to capture the vibration. A low mass, small, shear accelerometer (PCB Piezotronics 352C44) was used to measure the acceleration and a similarly sized force transducer (B&K ICP 8230) used for capturing the force with the data acquisition equipment, a B&K photon+ analyser. The average number of measurements was 10. Both of the accelerometer and force transducer are fitted with internal charge amplifiers converting the charge on the piezoelectric element to a voltage of sufficient amplitude for measurement. The data acquisition system also provided the initial current for powering the internal electrics. The location of excitation is 110mm in the x-direction and 80mm in the y-direction, assuming from left bottom corner of the panel for both accelerometer and force transducer. The block diagram of the experiment setup is shown in figure 3.4 below to illustrate the apparatus needed for the experimental setup.

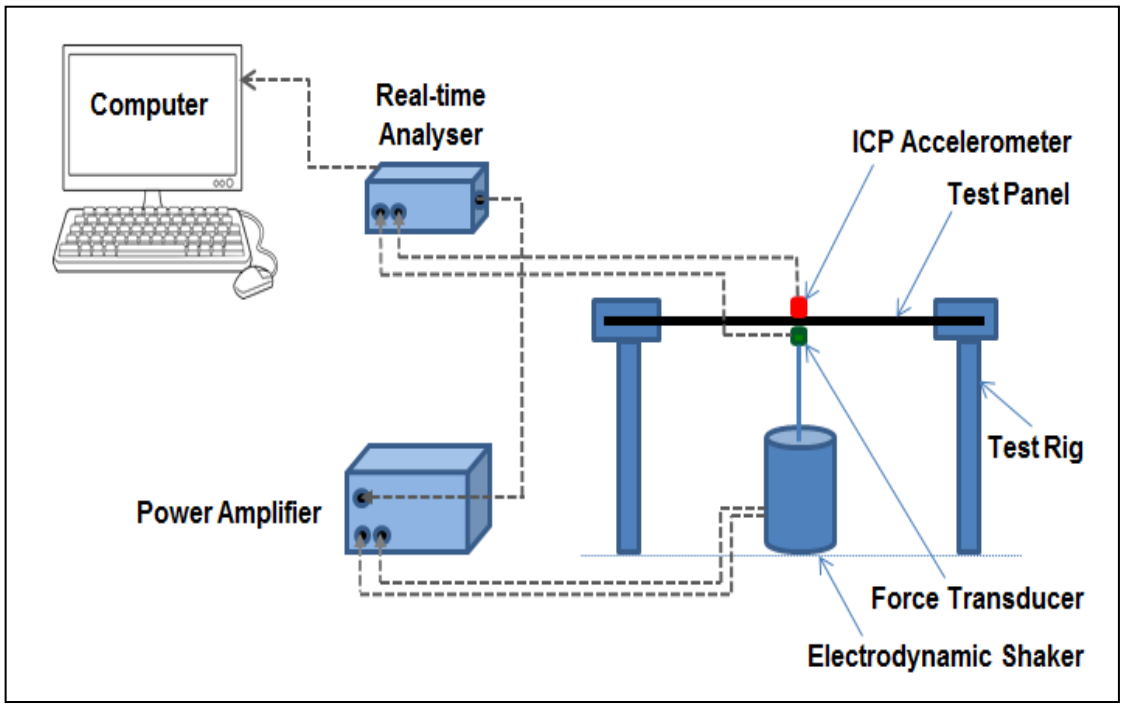

Figure 3.4 Schematic representation of the experimental setup.

3.3.1 Experiment Result -Mobility Experiment

The measure of the structure's vibrational response (velocity normal to the surface, out of plane) when given by changing load (again, applied normal to the surface) is called mobility. Furthermore, there is a term called point mobility where the excitation point coincides with the measurement point; otherwise the response is called transfer mobility. Whilst excitation in-plane is also important, for sound radiation and surface vibration, the out of plane excitation is of paramount importance.

Figure 3.5 (a) shows the experimental setup to calculate the point mobility for the flat panel. The location of excitation point and the measurement points are at the same location x=110mm, and y= 80mm from left bottom of the panel. Figure 3.5 (b) illustrates the *Graphic User Interface (GUI)* display during the experimental process.

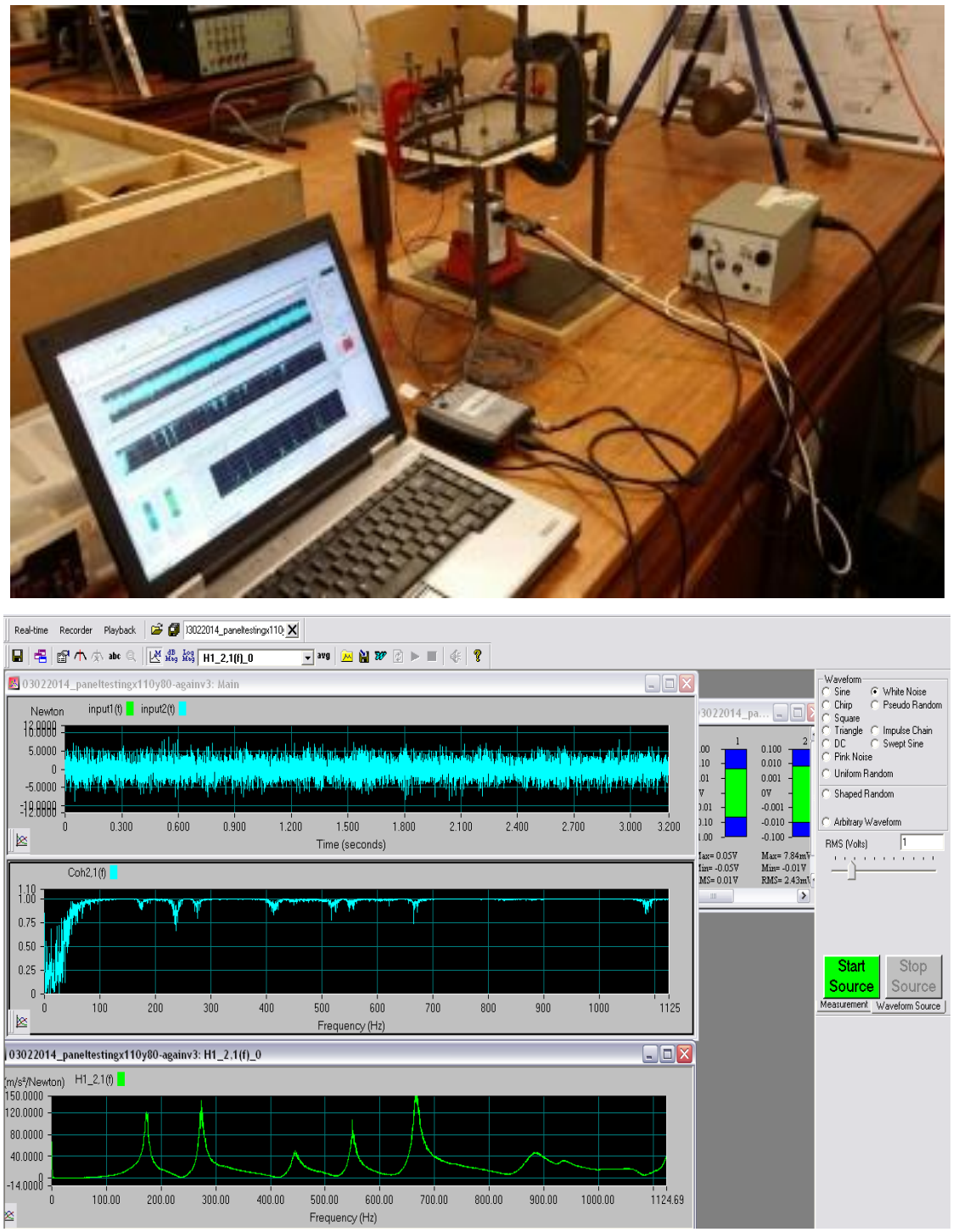

Figure 3.5 (a) example experimental setup for testing panel with clamped boundary conditions (b) *Graphic User Interface (GUI)* for the measured data.

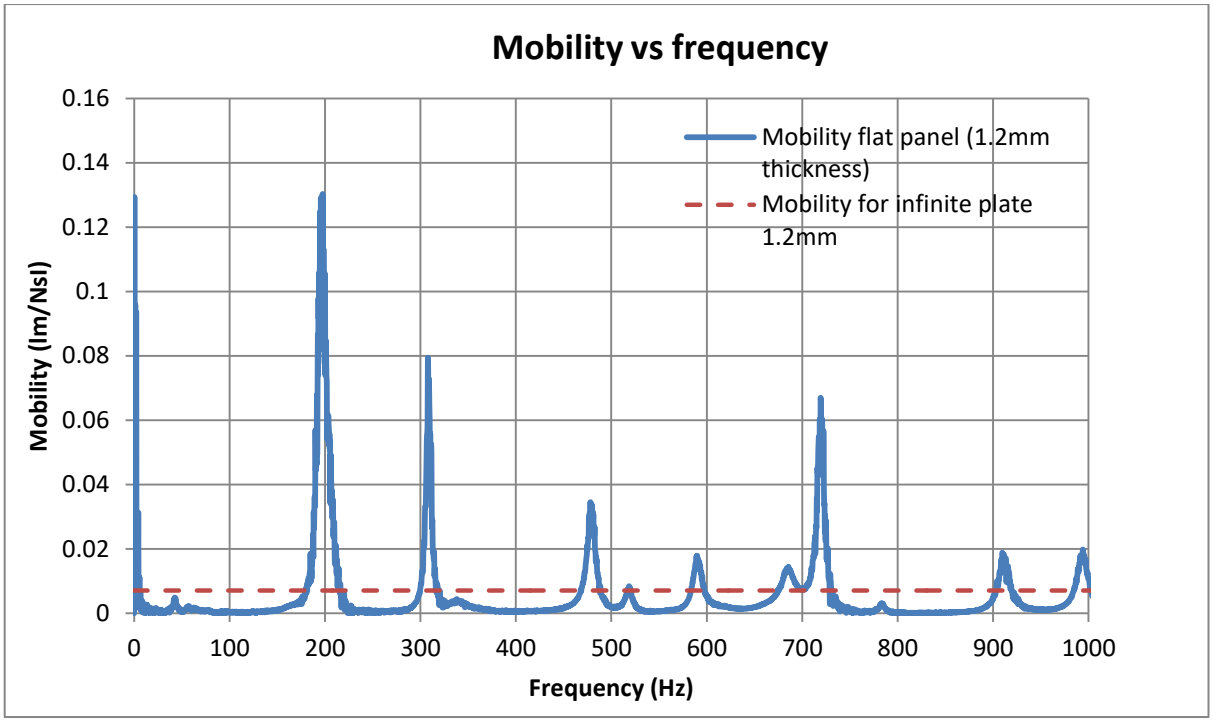

Figure 3.6 Measured mobility of the flat panel with the reference of infinite plate mobility values

The mobility of an infinite plate is frequently used as a guideline to have an overview and check the accuracy of the mobility function that being calculated. The equation to calculate the infinite plate point mobility is given by 3.6 below:

$$Y_{inf} = \frac{1}{8\sqrt{D\rho h}} \tag{3.6}$$

With D, ρ and *h* are flexural rigidity, density and thickness for the plate respectively [92]. Figure 3.6 displays the result of the measured mobility of the flat panel with the reference of infinite plate mobility values. Based from the experimental result, the resonance frequency from experiment and theoretical result show a small difference only especially at the lower mode. More discussion between the difference is covered later on section 3.5.

3.4 Finite Element Analysis

The panel has been investigated using finite element analysis through the NX 8.5 software containing a version of Nastran and a pre/post processor built in. The panel was designed according to the dimensions of the plate that is being used in the experiments. The solver used was SOL 103 Real Eigenvalues for-normal modes analysis with all edges clamped as the boundary condition. Whilst a SOL 108 Direct Frequency Response solution is a frequency by frequency analysis capable of resolving the internal damping more accurately, the modal solution from SOL 103 yields natural frequencies, of interest to this study, in a fast and computationally efficient manner by just using the mass and stiffness matrices. Element type used was CTETRA (tetrahedron) with element size of 5 mm. Total number of elements is 4306 and total number of nodes is 9075. Figure 3.7 below shows an example of the mode shape of the (2,1) mode under a perfect clamped boundary condition and the list of natural frequencies which correspond to the mode shape.

Clamped Boundary Condition

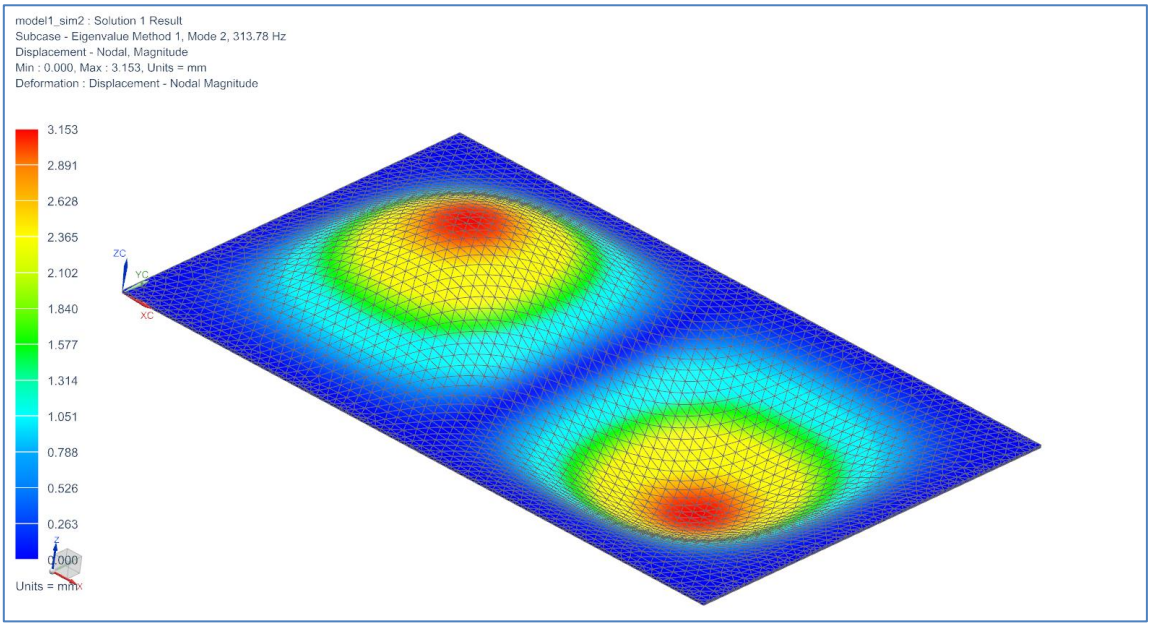

Figure 3.7 Example of a mode shape (2,1) of the natural frequency for a flat panel and a table of the flat panel model shapes with it respective frequency value.

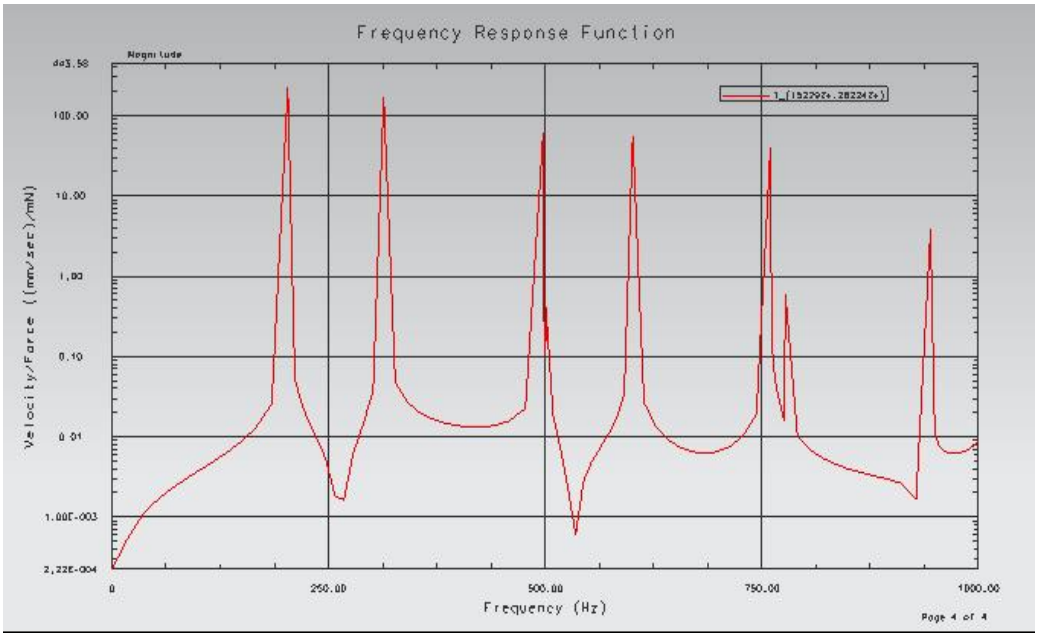

Figure 3.8 Example of graph showing frequency response function for the flat panel at the location of x=110mm and y=80mm

As this is a modal solution, no damping is considered in the solution of the finite element method, only mass and stiffness matrices are included. A small amount of modal damping is then included to obtain frequency response functions (FRF) however, as this is for an undamped plate, the material damping will be low. It is likely that more damping will occur at the boundary where the clamping takes place.

Furthermore, from the finite element analysis, the frequency response function for the flat panel at the location of x= 100 mm and y=80 mm can be determined as shown in figure 3.8. More simulation results can be found in chapter 4 later.

3.5 Comparison between Theoretical, Experimental and Finite Element Analysis.

All the data from the finite element analysis, theoretical and experimental measurements, are compared against each other for every respective mode as shown in table 3.4 for a clamped boundary condition. Based on the data, the accuracy of the frequency from the FEA shows a small different in terms of value

when comparing with theoretical, perhaps as the theoretical case neglects the consideration of rotary inertia and shear deformation in the thickness of the plate. That gives a good confident level with the accuracy of modelling in FEA and theoretical part which is good as a start for the next level step. The small discrepancy could be because of the slightly different value of the material properties used by the software and theoretical calculation.

Table 3.4 Comparison mode shapes with the frequency to the respective method for clamped boundary conditions.

Mode		Frequency (Hz)		
m	n	FEA	Theory	Experiment
1	1	203	203	200
2	1	313	313	310
1	2	497	497	480
3	1	501	501	515
2	2	601	601	590
3	2	777	775	720
4	1	760	759	685
1	3	944	940	938

In additional, the results from the experiment also show a good compromise with an error below 5% when comparing with the theoretical value for each resonant frequency. Although it gives a good confidence level between experimental and numerical results, the accuracy between both of the methods still have some space to be improved.

First, the exact properties for the panel need to be calculated. Presently, for the theoretical and numerical cases, the material properties used are based on the general material properties and few measured properties. The majority of materials have a range of values of properties for Young Modulus, density or

Poisson ratio. Dimensions and weights of the panel need to be measured accurately to acquire a correct density and stress-strain tests can be carried out to calculate the exact Young's Modulus. On the other hand, the mesh size for numerical analysis also can be decreased to increase accuracy of numerical analysis.

3.6 Measurement of Sound Radiation

The sound power level of a radiated structure can be measured by few ways, according to their test environment and need with the respective standard [93]. The sound radiation efficiency is the measurement of how efficiently surface vibration waves of a given frequency can propagate from a vibrating structure into acoustic waves. Generally the measurement can be accomplished using either multiple measurements of sound pressure around a given shape or sound intensity measurement with some of the standard respectively [94,95] and [96,97].

The sound pressure measurement method is based on measuring sound pressure at many different points in the shape of a hemisphere or parallelepiped according to the corresponding standard and test setup. However, this method requires a high number of channels for data acquisition and a corresponding number of microphones if it needs to be completely run in a short time of measurement simultaneously. Alternatively, the sound pressure measurements at a single point can be taken with a low number of channels, moving the microphone from one point to another with the assumption that the test object isn't changing between measurements (or that the phase of the different measurements is not coherent). It also assumes that the movement of the sensor doesn't affect the test structure. The sound intensity measurement method is used and discussed in this chapter to measure the sound power level and later will be used to compare with the predicted value calculated based from the DIC result.

Sound intensity is defined as the power carried by sound waves per unit area. In order to determine sound intensity, it is required for the sound pressure and particle velocity to be measured at the same point. Currently, there are two categories of a probe in widespread use to measure it. The first is "p-u" probe,

which combines a pressure transducer with a particle velocity transducer. A second option is a “p-p” probe that is made up of two matched microphones separated by a spacer for measuring sound pressure and particle velocity [98]. The measurement in this chapter is based from the “p-p” type of probe as shown in Figure 3.9, using a Bruel & Kjaer sound intensity probe kit type 3599 including sound intensity microphone pair type 4197 and dual preamplifier type 2683. The sound intensity can be calculated from the cross-spectrum of the sound pressure signal of the two microphones from the probe using the following equation 3.7 given by Fahy [99]:

$$I_n(\omega) = \frac{1}{\rho_0 \omega d} \mathrm{Im}\left[G_{p2p1}(\omega)\right] \tag{3.7}$$

where I_n Indicates normal intensity (with *n* defined by the orientation of the intensity probe), ρ_0 is the density for the acoustic medium, *d* is length of the spacer in the probe (or space between the two microphones) and $\mathrm{Im}\left[G_{p2p1}(\omega)\right]$ is the imaginary part of the cross spectrum for the two microphones. The test was conducted in the anechoic chamber so the back ground noise level is insignificant compared to the experiment.

Figure 3.9: Image of sound Intensity Equipment (a) remote control ZH 0632 (b) complete setup – image taken from B&K ref.[100])

3.6.1 Experimental Setup using Sound Intensity Method

The sound intensity method with measurement by scanning as described in BS EN ISO 9614 revised 2002 was selected to measure the sound power level and has been conducted in the Loughborough University anechoic chamber. The setup was based around the frame with a clamped plate at the centre of the lab. An addition homemade wireframe (anechoicly invisible) was added to enclose the plate and to be a guideline to control the scanning distance and surface area as shown in Figure 3.10 (a). The normal intensity of each part of the surface area was measured by placing the two microphones of the intensity probe perpendicular to each surface. The intensity probe was simply swept over the selected surface to determine the spatial average of the intensity measured normal to the surface as shown in Figure 3.10 (b). Afterward, the partial sound power for each surface is calculated by multiplying the spatial average normal intensity with the area of measurement surface. Finally, the total sound power is then calculated by adding the sound power of all part surfaces.

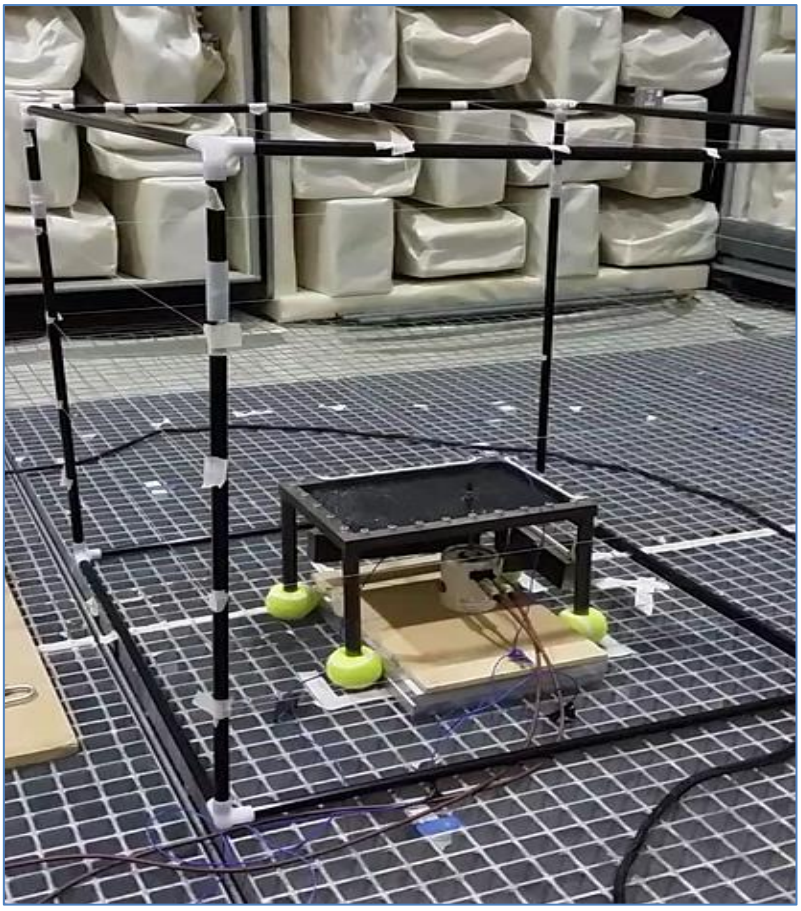

Figure 3.10: Sound Intensity Frame setup (a) clamped plate with additional wireframe (b) swept measurement over a surface – image taken from B&K sound intensity ref. [101]

3.6.2 Measuring Equipment for Sound Intensity Method

For the acquirement and analysis of the results, RT pro signal analysis software together with a 4 channel *Photon+* portable analyser has been used. The general connectivity setup of the measuring equipment was shown systematically in Figure 3.11 below.

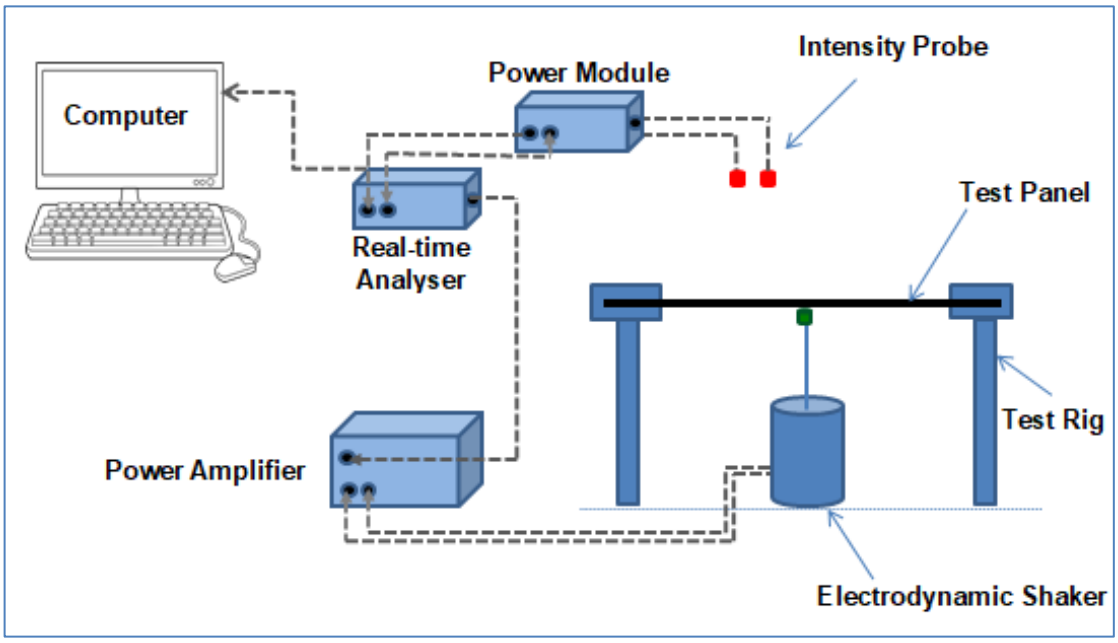

Figure 3.11 Setup of the measuring equipment for measuring sound intensity from a test structure according to relevant standards.

An electrodynamic shaker was driven by the output of the analyser through the power amplifier and was placed under the test rig to excite the plate. The shaker was excited by a sinusoidal source at a frequency that was predetermined first through point mobility experiment as discussed in the previous section 3.3.1. As mentioned in the section, the plate was already excited with a broad band source to find the response frequencies and amplitude through the modal analysis. Based from the finding, the frequency of peaks of each resonance frequency will be used as the sinusoidal source for the sound power measurement. Therefore, the sound intensity measured corresponds exactly to the sound radiated at one particular frequency.

The intensity measurement carried by the B&K intensity probe was connected to G.R.A.S 12 A power module for polarisation before being connected to the input in the signal analyser. Each of the microphones at the intensity probe was calibrated first using a sound calibrator to ensure the measurement data was captured accurately. Finally, the RT Pro analysis software was performed on the time signals captured by the *Photon+* portable analyser. The results from the measurements on the test plate are shown in the next section.

3.6.3 Sound Power for a selected mode using Sound Intensity Method

The Digital Image Correlation method is typically applied to structures using a high speed camera to obtain data on the vibration response of a surface. This is expensive and requires highly accurate data processing hardware with high speed precision. In this thesis, the novel aspect of using the DIC with a low speed camera is investigated. Whilst this has been used before, the capabilities and application are investigated in this thesis to show what can be achieved and to what accuracy.

The DIC setup with two low speed cameras (see next section 4.3) does not have the capability to capture a high vibration image because of the low frame per second (fps) value. However, if the low speed camera is used for a high frequency vibration experiment, an additional step needs to be taken called phase-locked measurement with a limitation to capture only at a sinusoidal and repeatable source. Thus, in order to measure and compare with the responding sound power, the measurement of sound power level was done under the same sinusoidal type of vibrating source, not the white noise type one that is normally done when measuring point mobility. The repeating sinusoidal source frequency was determined earlier from the frequency response function experiment. Here are some of the selected modes that were being considered.

Mode (1,1)

The plate was excited by the electromagnetic shaker vibrating at the first resonance response frequency and the result of sound power was shown in Figure 3.12 below. Mode 1,1 is the lowest mode shape determine by the point mobility experiment where the damped natural frequency is calculated to be 200 Hz.

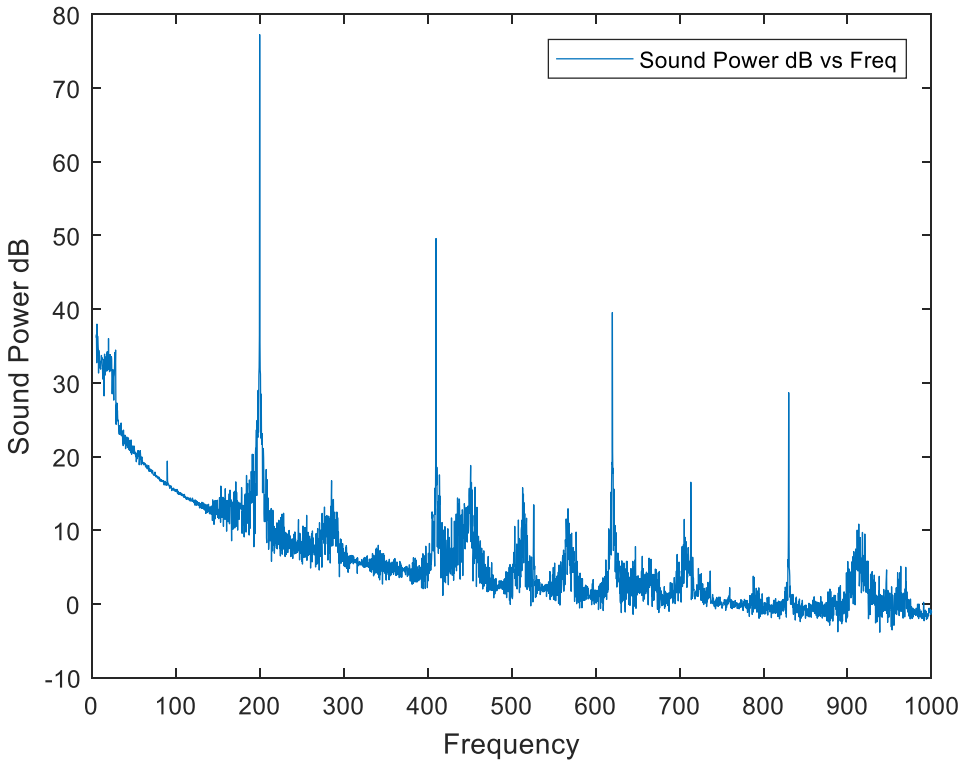

Figure 3.12: Sound Power Level for mode 1,1

From the figure, four main peaks of resonance of the plate can be seen with the highest plate resonance occurring at the first mode which is the frequency of the vibrating source. The sound power value of the first peak is 77.25 dB.

Harmonics of the primary resonance still appear at relative high amplitude with the response at other excitation frequencies very low. Despite not being excited with broad band noise, some energy over a wider frequency range

does generate additional responses in the plate, albeit at a relatively low level.

Mode (2,1)

The plate was then excited at the second resonance frequency corresponding to mode (2,1) and the result of sound power was shown in Figure 3.13 below. From the figure, three main peaks of resonance of the plate can be seen with the highest plate resonance occur at the frequency of the vibrating source, 310 Hz at 77.4 dB. When excited at this frequency too, it also results in three main peaks with the differences between each adjoining peak being almost the same as the frequency vibrating source. Hence, it is also believed that the effect of standing waves causes these three peaks and results in the dominant sound power level.

Although the broad band noise peaks appear high in amplitude, due to the decibel scale, the amplitude is very low.

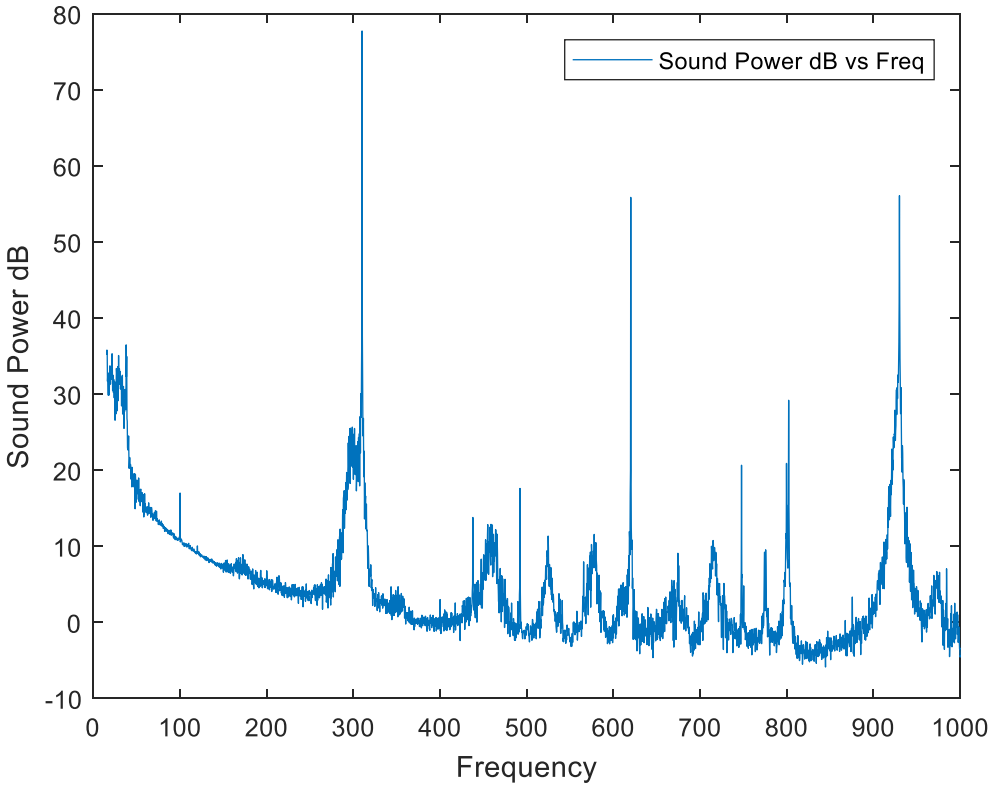

Figure 3.13: Sound Power Level for mode 2,1

Mode (2,2)

Then, the plate was excited at a frequency of 590 Hz, which corresponds to mode 2,2 and the result of sound power is shown in Figure 3.14 below.

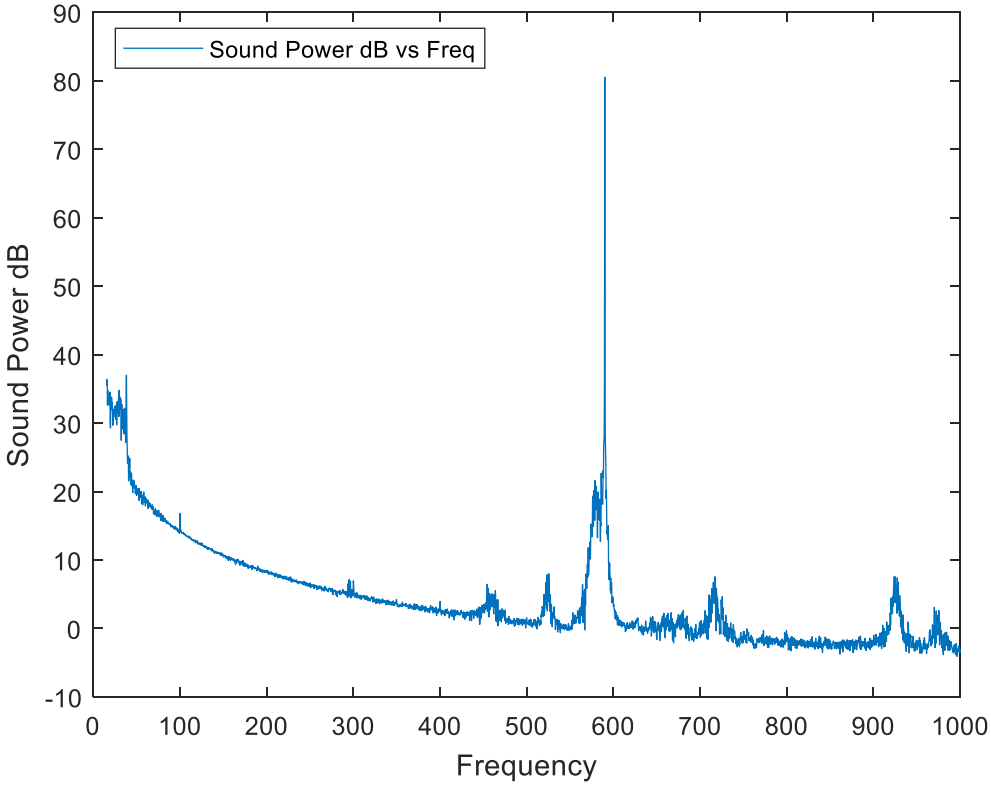

Figure 3.14: Sound Power Level for mode 2,2

From the figure, only one main peak of the plate can be seen clearly which is the frequency of vibrating source, where the harmonics are above the visible range shown. The overall sound power level is 80.5 dB showing a consistency of mode amplitude with frequency (implying that the amount of energy going into the plate is similar, and that radiation efficiency is also likely to be similar).

3.7 Conclusion

This chapter explore the characteristic of structural properties for automotive type panel in terms of resonance frequency and mode shape. The resonance frequencies throughout experiment were validating theoretically and computationally using FEM Nastran. Then, the characteristics of modal sound power for the plate for lower modes was experimentally obtained using sinusoidal resonance frequency as a vibration source. This modal sound power value will later be used to validate the prediction model that will be discussed more in Chapter 5.

CHAPTER 4
Digital Image Correlation Technique

4.1 Introduction

Digital Image Correlation (DIC) is a modern non-contact, full-field optical technique that is being used for the measurement of static and dynamic displacement problems, material testing and fracture mechanics. In particular, three dimensional (3D) DIC is able to measure the out-of-plane vibration mode shapes and deformation of a vibrating structure. The 3D DIC in this thesis will be used as a tool to measure the surface displacement for the plate when given specific resonance frequency vibration from a shaker. DIC works by comparing digital photographs of a component or test piece at different stages of deformation. By tracking blocks of pixels, the system can measure surface displacement and build up full field 2D and 3D deformation vector fields and strain maps.

Experimental modal analysis will be performed together with digital image correlation methods. These sets of sequence deformation image will represent the mode shape of the plate and can be validated with the FEM result from chapter 3. Moreover, this set sequence of surface displacement images for particular modes will be analysed, to be used in developing the predicted sound power model in chapter 5. One important parameter that is required in order to predict the sound power is the average mean square velocity for the surface displacement. This calculation will be based from the deformation image captured by the DIC equipment in this chapter.

This chapter begin with a discussion about the Digital Image Correlation (DIC) method through a background, and details how the method is applied, how the DIC equipment is used to obtain information about the distribution of surface velocity on an object, as well as the experimental setup, which can be considered best practice. Then, the discussion continues on sample preparation and the

additional steps which are required called phase lock measurement if the experiment runs using a low speed capability camera. Finally selected mode shapes result based from the DIC measurement will be compared with the simulation run using FEM as validation purpose.

4.2 Digital Image Correlation overview

Traditional methods for collecting experimental structural dynamics measurements involve using individual sensors, which provide measurements at discrete points by contacting the device under test (accelerometers and strain gauges for example). However, this traditional method will result in adding relative mass to the test subject when using a lot of sensors, thus it opens more opportunities for the development of non-contact testing.

As the design of high-performance structures has become more innovative, the expansion of non-contact full-field measurement methods has received more consideration. There is an increasing need for experimental techniques capable of measuring the response at a large number of degrees of freedom without modifying the structural response significantly, due to complex geometries and the light weight nature of these structures. The vibration testing industry is also increasingly performing tests to failure, and it is important to capture the strains that are leading to these failures. It is also important to capture full-field measurements that are able to capture complex shape information to correlate with uncertain regions of computational models with large degrees of freedom.

Techniques such as Laser Doppler Vibrometry (LDV), and high-speed Three-dimensional Digital Image Correlation (high-speed 3D DIC) have been developed to meet this current need [102]. Non-contacting techniques, such as scanning laser Doppler Vibrometry (SLDV) have become well recognized in the modal testing community, while other optical techniques, such as digital image correlation (DIC), are relatively new in structural dynamics. A lot of researchers have established the use of LDV techniques or continuous scanning LDV on modal testing, [103-106] and

some of them compare results with the findings from the high speed camera DIC measurement [107,108].

Reu et al. [107], when comparing between the high speed DIC and LDV mentioned few disadvantages of LDV such as acquisition time taking hours compared with seconds only for high speed digital DIC and the LDV cost which are relatively higher (around two times total cost), which opens the chance for DIC to grow more. Helfrick et al. [109] in his paper mentioned that the data collected using DIC can provide useful empirical data for correlation with finite element models. Niezrecki et al. indicates that it was possible to measure all of the points on the structure simultaneously using DIC, but only one mode at a time [110]. Beberniss et al. in his paper review some recent advancements and limitations on high speed 3D DIC vibration measurement such as the ability to capture good mode shape results and less sensitivity to detect higher frequency displacement [111].

However, most of the research on structural dynamics or vibration testing for DIC are using dual high speed cameras to acquire 3D vibration measurement due to the nature of dealing with high frequency. Therefore, there are some potential growth to reduce more on the DIC cost but the research related to it is currently limited. Yu et al. implement a single camera high speed stereo-digital image correlation method using a four-mirror adapter for full field 3D vibration measurement [112]. Lopez et al. also proposed pseudo-stereo portable system that employs a mirror system integrated in a flexible device for a straight forward application [113]. Warburton et al. use conventional camera (not the-speed) for DIC experiment via the use of a stroboscopic lamp and ancillary circuits [114], while Mat Tahir et al. implemented the phase lock measurement methods [115] and Fruehmann et al. using the lock-in amplifier to apply DIC to cyclically loaded components [116].

The fundamental measurement made is of digitized light intensity values across a rectangular array of pixels embedded in the CCD cameras. Every individual cell of the array stores a numerical gray-scale value related to the intensity of the light reflected from the object. Through a correlation process, a computer is able to recognize and track a specific point defined by its surrounding light intensity

values on a series of images. By tracking discrete points in images taken by a stereo pair of cameras and applying photogrammetric principles, shape, strain, and displacement can be measured [109]. The geometries involved in a stereo camera setup are described in Figure 4.1.

Figure 4.1 Image of two image planes corresponding to one object surface under a stereo camera pair (taken from ref.[109]).

Calibration panels with a series of dots on a rigid flat surface are typically included with the DIC packages. The calibration panel is sized so that it fills the desired field-of-view for the measurements to follow. The known distance between the dots is input into the software. Snapshots of the calibration panel are analyzed by the DIC software allowing the position of the cameras relative to each other and the internal distortion parameters of each lens to be accounted for. A series of image pairs are taken during the course of an experiment. The first pair of images is set as the reference stage to which all subsequent stages are compared. The computer divides the images into overlapping subsets, typically 10–20 pixels square.

The corners of each subset must be coordinated within the surrounding of light intensity values for the correlation to work. This is why a speckle pattern is applied to the object prior to imaging. Studies of vibrations often require the

measurement of minor movements, therefore, the sensitivity of DIC measurement must be understood, especially for measurements in the out-of-plane direction. The relation of the pixel size to the object sample size must be known. This is typically done by dividing the width of the field-of-view by the number of active pixels across the width of the pixel array to obtain a distance per pixel. The sensitivity will decrease as this number gets larger. These sensitivity values vary depending on a number of factors including lighting and speckle pattern uniformity.

Designated 3D-DIC, a typical stereovision system employs two or more cameras to record digital images of a common object region from two or more viewpoints. Using DIC to perform cross-camera subset matching, a calibrated stereovision system theoretically can obtain the true, three-dimensional (3D) position of each point on a non-planar object.

4.3 Digital Image Correlation Measurement

The digital image recording is done via a CCD (charge coupled device) camera which converts photons to electric charge based on the photoelectric effect. Two set of cameras with 5MP (megapixel) sensor resolved with 12bit states was used for the DIC experiment. The distance between the camera system and the specimen was determined by the available lenses. The short lenses are generally easier to work with and can give somewhat better results. The distance is set so that the specimen fills the field of view. If the specimen is larger than the field of view, data is lost at the edges; if the specimen is much smaller, the spatial resolution suffers [117].

Figure 4.2 DIC setup between the camera and plate with the additional lamp.

Figure 4.2 shows the DIC setup for between the camera and the test panel with the additional lighting. Davis 8.2.1 software from Lavision was used as a tool to capture and post processing the entire seized image. The user selected colour resolution is used by the mapping from pixel intensity or vector length to the colour in which the pixel/vector is displayed on screen. In DaVis software there are 256 colours, indexed from 0 to 255, which are arranged in the order of the active palette. It contains intensity values from 0 to 65535 counts, which have to be displayed with 256 colours. Therefore the software maps the 65536 intensity values to the 256 colours [118].

The practical limitation on the oscillation frequency is dependent on camera sensitivity and lighting. The software has the ability of 64K intensity for 256 colours. However, because of light source limitation and the need to capture the lowest exposure time to “freeze” the motion, the intensity count was reduced to

1K. This means, it will lead to a new colour after interval of four counts. Thus, the exposure time of 100μs can be achieved. By reducing the colour of depth, the transition between each colour result become less smooth, but it is reasonable since the results expected are not focusing on the small area or spatial resolution but at the size of plate overall. In order to increase the experimental accuracy, additional lamps were used to provide extra light to capture the image in a very small exposure time.

4.3.1 Sample preparation

The sample surface has to exhibit certain properties which consist of grey contrasts to be able to run the process. The ideal surface texture should therefore be isotropic and not have specific orientation. The speckle pattern should be non-periodic and avoiding any repeating textures (ideally random). The plate was sprayed completely with black paint before white sparkle paint was applied to the surface. The white sparkle position will be used by the camera and the software as guideline to tracking the movement while running the experiment. Figure 4.3 represents an example of the panel with white sparkle that being used for measurement.

Figure 4.3 Sample plate with white sparkle

4.3.2 Phase locked measurement

Ideally, when dealing with a higher vibration frequency, a high speed camera should be used to capture the movement of the plate. However, this thesis is concerned with the setup using the low speed camera. Since the camera's frame rate may not be fast enough to capture several images in a single cycle, it is necessary to skip several cycles before advancing to the next attempt to obtain an image, but locked to the same phase as the original. Thus the signal is accurately tracked by the phase locking. Phase locked measurements method required a trigger signal generated from known position in the cycle to be sent for the system to capture the image by tracking the phase locking logic. Figure 4.4 below represent by knowing and controlling the camera frame rate, we can replicate a single wave cycle.

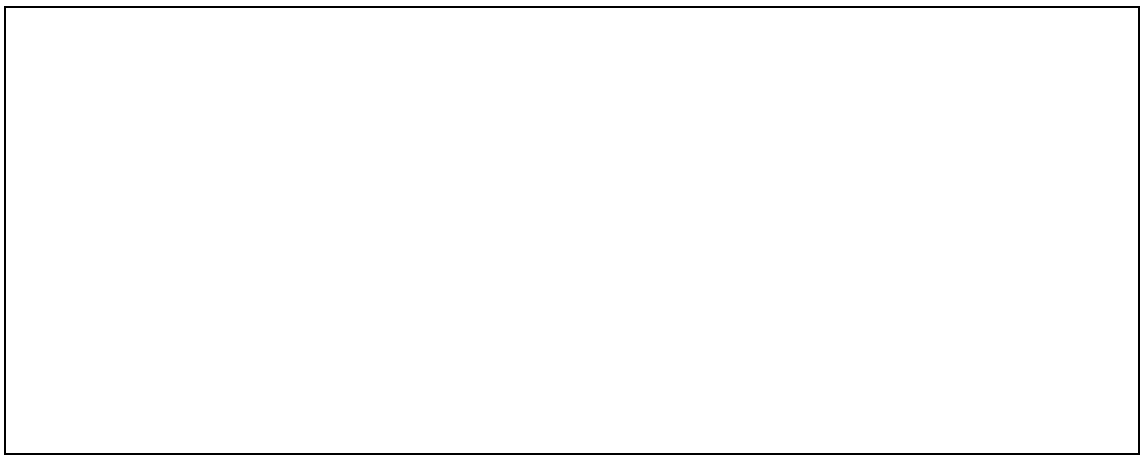

Figure 4.4 :Image of replication of single wave signal from purely cyclical motion (taken from ref.[117])

The red line represents the frequency of vibration experienced by the panel and the dot represents the position of the wave for each image taken. By series of knowing the image position and the order in which images are taken, the replication of single wave signal images can be created.

However, for a simplified case, the modification to the locking system can be run under mathematic calculation formula (entered prior to starting the experiment) to control the camera recording frequency (depending on the

maximum capability of the camera). This step can reduce the usage of cable and trigger systems which may reduce the extra cost. One assumption that needs to be made is, the signal from purely cyclical motion is maintained the same in the whole process without changing the amplitude or speed of wave. This is to say that the generated motion is entirely linear and fully periodic.

4.3.3 Complete test setup for DIC

The Davis 8.2.1 systems were being controlled separately from the Photon Plus data acquisition hardware arrangement. However, the voltage reading from the shaker was captured by the analogue to digital converter to represent the location of shaker movement for each picture taken. The previously conducted measurements on point mobility for the clamped plate provided the knowledge of the location of resonant frequencies.

The experiment was started by doing a calibration test. It was done by capturing an image of a calibration plate by putting it onto the panel. This step controls the camera lens for the required focusing distance and reasonable aperture size. The image must be set to have a good focus and sharp image and the exposure time are not over or under-exposed.

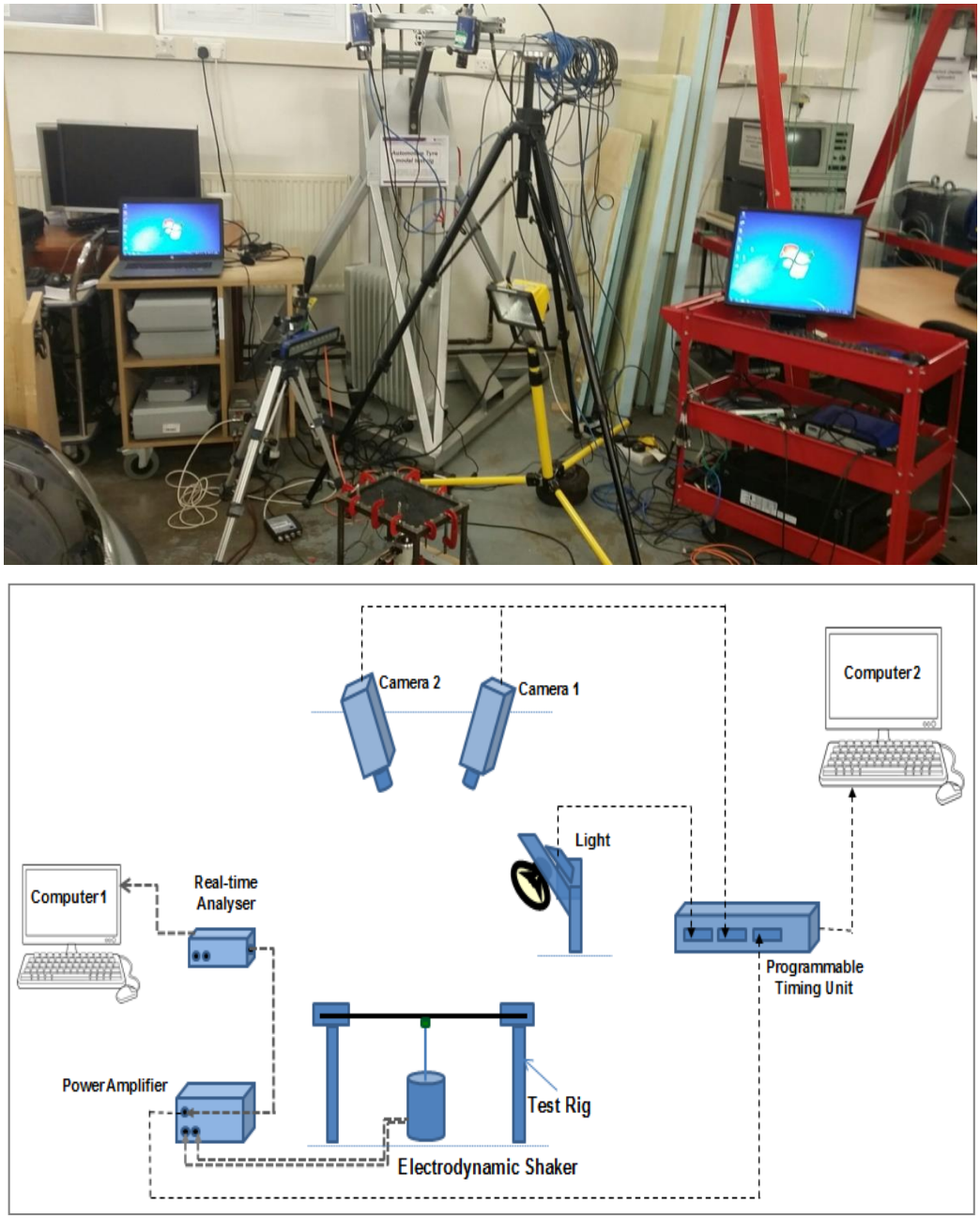

Figure 4.5: Complete setup between the DIC equipment and Photon setup

Then, after the calibration image is captured correctly, at least one static image of the plate was taken as the baseline to be compared with the image taken during the subsequent dynamic test. Figure 4.5 demonstrates the setup for the complete DIC testing and the panel vibration with shaker underneath the plate as a vibration source.

A sinusoidal vibration source underneath the plate at a chosen frequency is provided according to the resonance frequency determined earlier. Next, a

set of 42 sequence images of the plate were captured according to the frame rate that was fixed in the software. The number of images can be determined according to the user preference. A lot of images taken can represent a good replication of single wave signal but it also will take a lot of memory space for storage and computational processing time, which can potentially contradict the ambition of a low cost, non-contact measurement system as it leads to an increase in computational and therefore wasted staff time. The series of images are post-processed, beginning by appending the static image with the series of dynamic images. This static image will be the base comparison of the plate's displacement when given the load.

4.4 Digital Image Correlation Results

4.4.1 First Mode (1, 1)

The graph in figure 4.6 below shows a sequence of 43 images (42 images plus 1 static image as base reference) taken respectively with the voltage provided to the shaker from the power amplifier at the first mode. Every point/image captured by the low speed camera represents the location of the shaker movement (higher frequency) which then can replicate the single wave signal image.

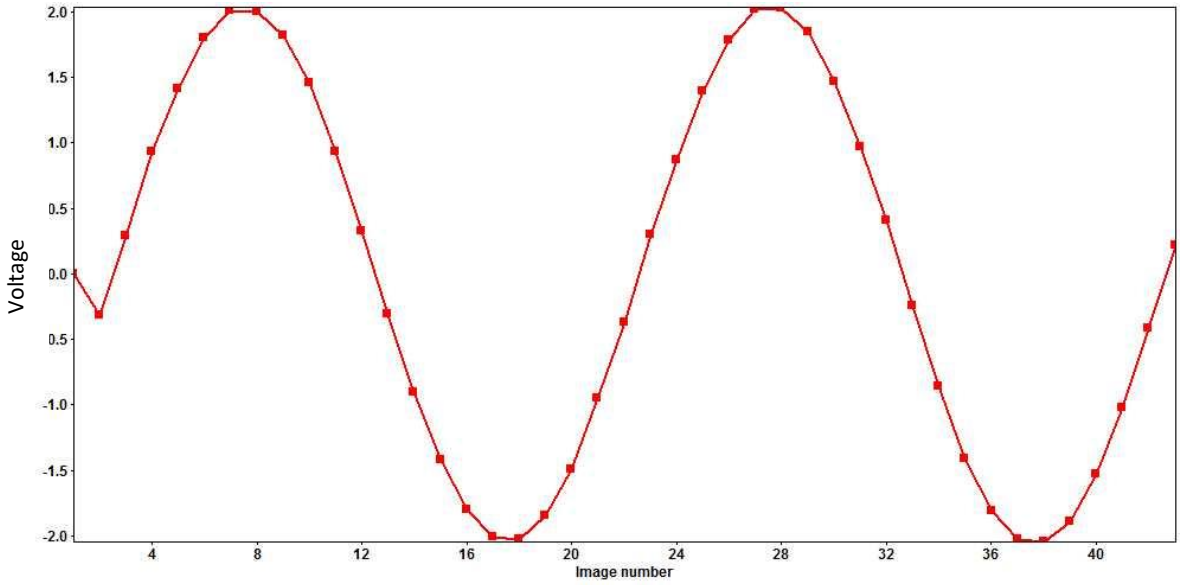

Figure 4.6 : Graph number of image versus voltage value from shaker for mode (1, 1).

Figure 4.7 below shows the series of selected images (for 2 complete cycle) that represent the behaviour of the mode at the given frequency. The full image capturing by the DIC can be seen in the Appendix. The image number 2 shows a value near 0 voltage expressing the neutral behaviour of the panel with deformation almost distributed evenly on the panel. Then when the voltage was increasing and reaches the highest value, the maximum of the plate can be seen at the centre of the plate as shown in image 7. Next, the voltages start decreasing and reaches the lowest value, the maximum deflection in negative –z direction (will be known as minimum) deflection of the panel can be seen near the centre of the plate as shown in image 18.

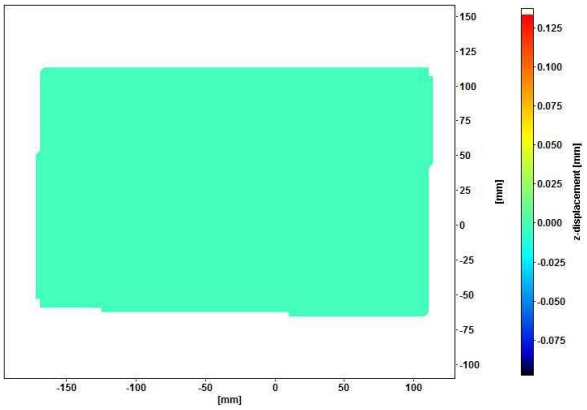

Image no 1

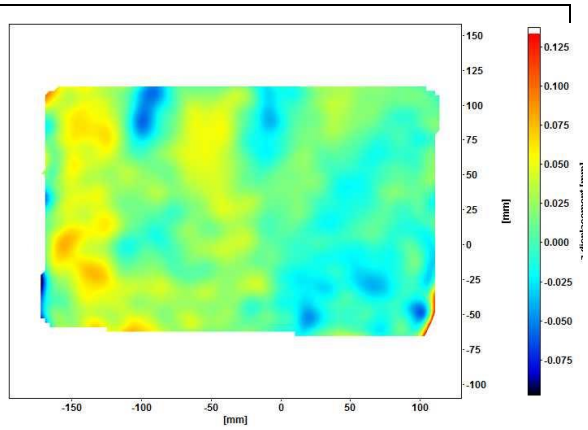

Image no 2

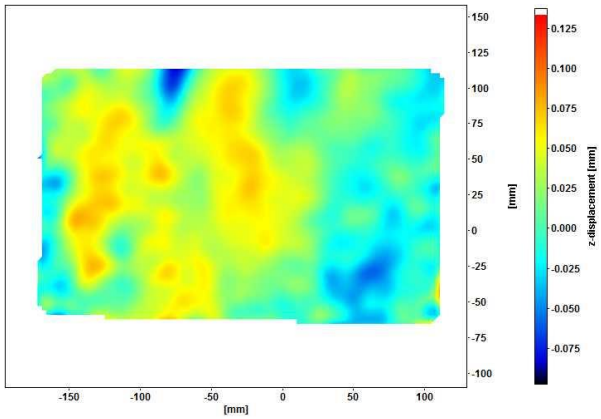

Image no 3

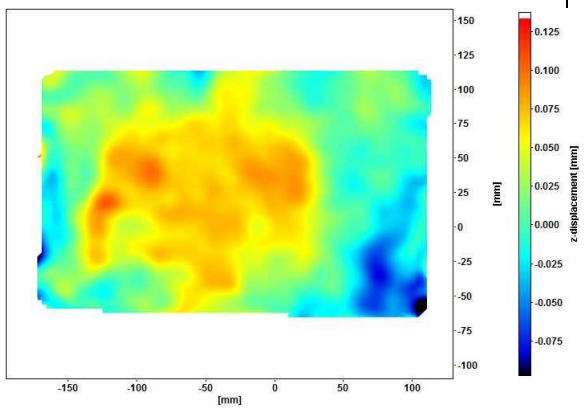

Image no 4

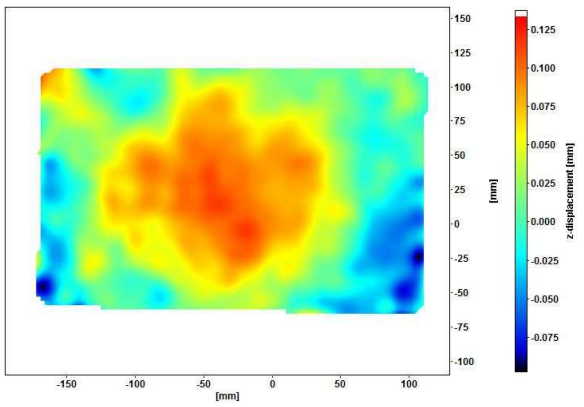

Image no 5

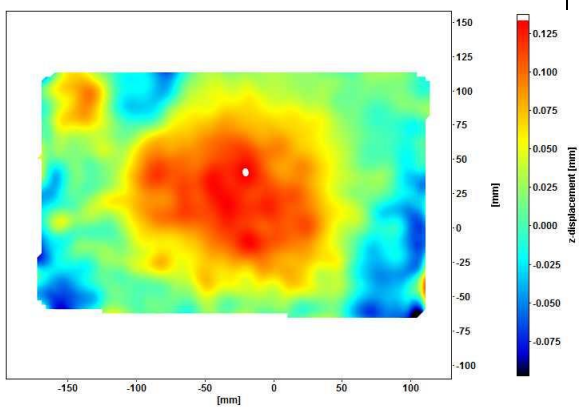

Image no 6

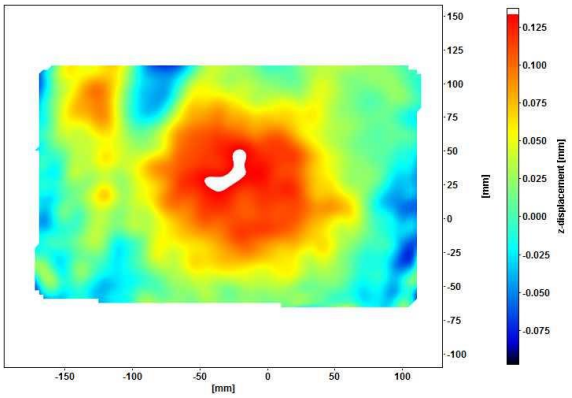

Image no 7

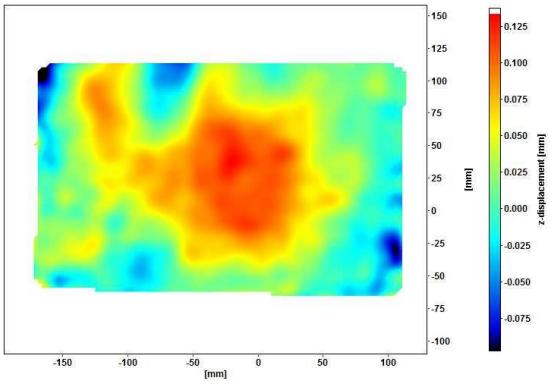

Image no 8

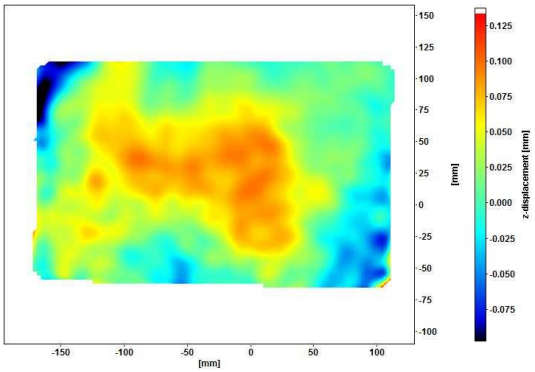

Image no 9

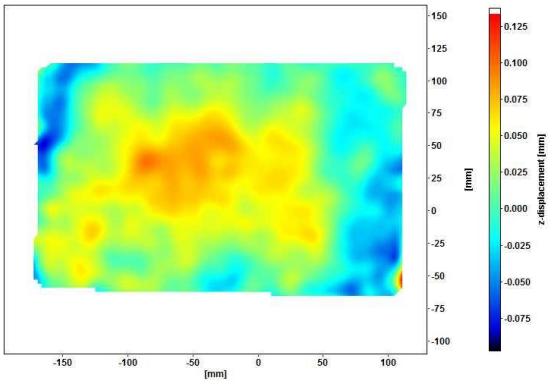

Image no 10

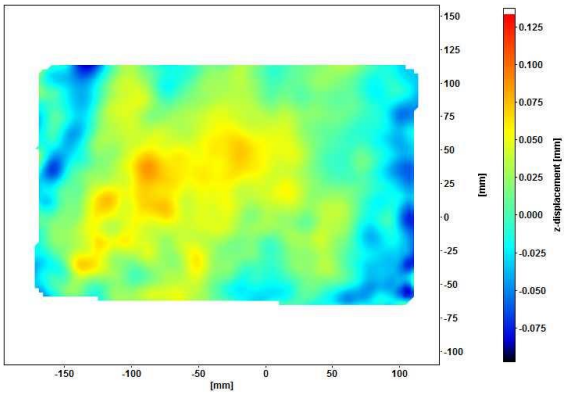

Image no 11

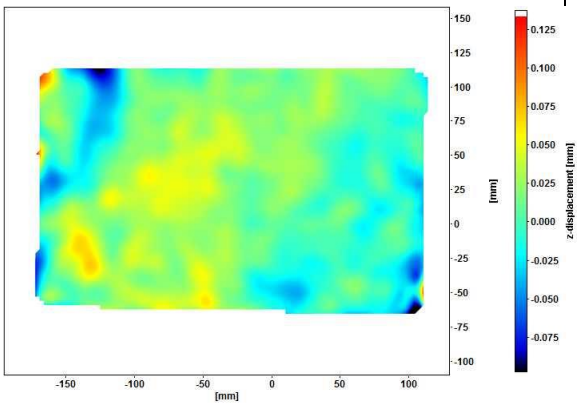

Image no 12

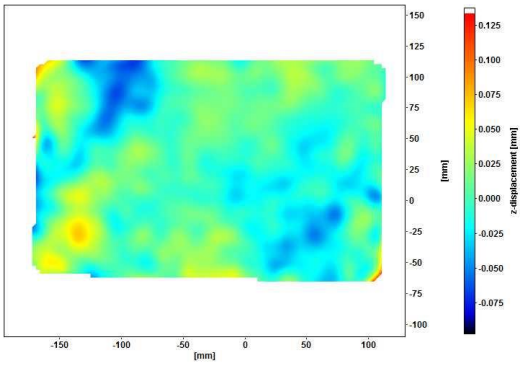

Image no 13

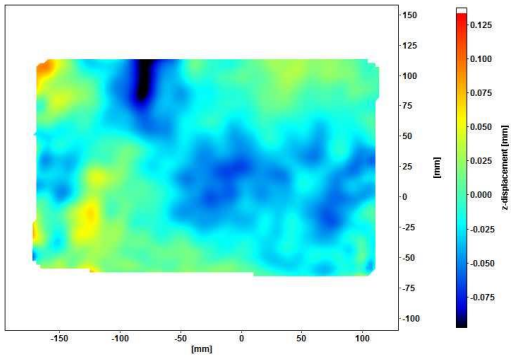

Image no 14

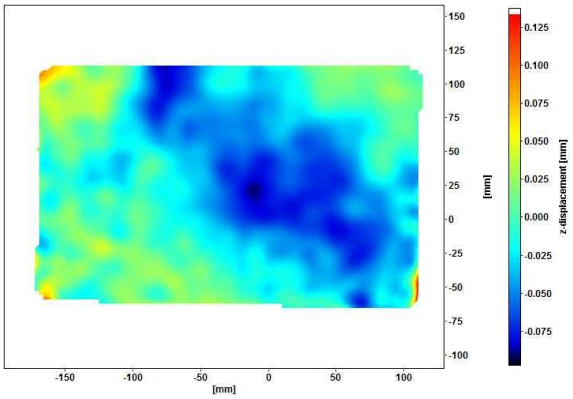

Image no 15

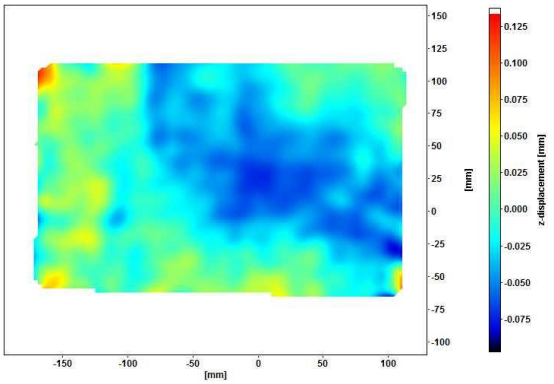

Image no 16

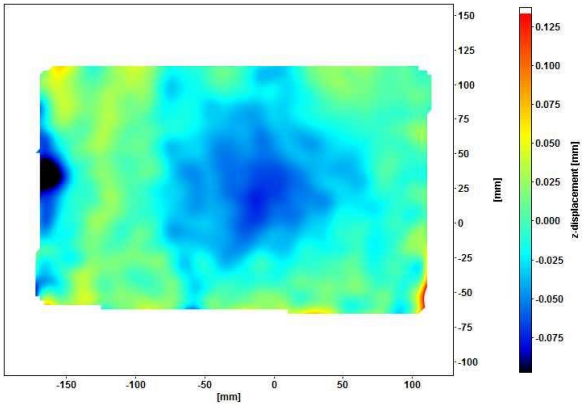

Image no 17

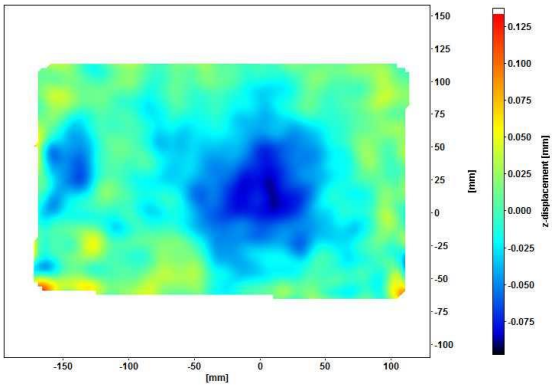

Image no 18

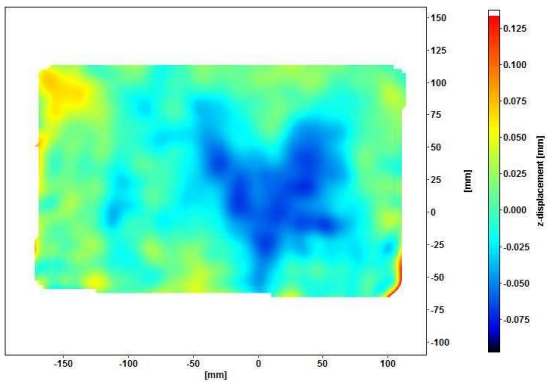

Image no 19

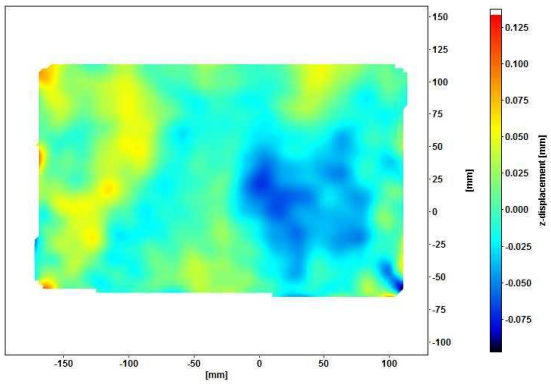

Image no 20

Figure 4.7: DIC image showing one complete cycle from image 1 until 20.

Generally, the behaviour captured by the DIC camera represents the same predicted mode shape results from the FEM simulation for the first mode shape as shown in figure 4.8 below. The mode shape in simulation show a circular one peak and bottom at the centre alternating, the DIC also displays an image of one peak and bottom at the center alternating. However, from the DIC result, the actual plate shows an interesting non-uniformity of vibration against the finite element method.

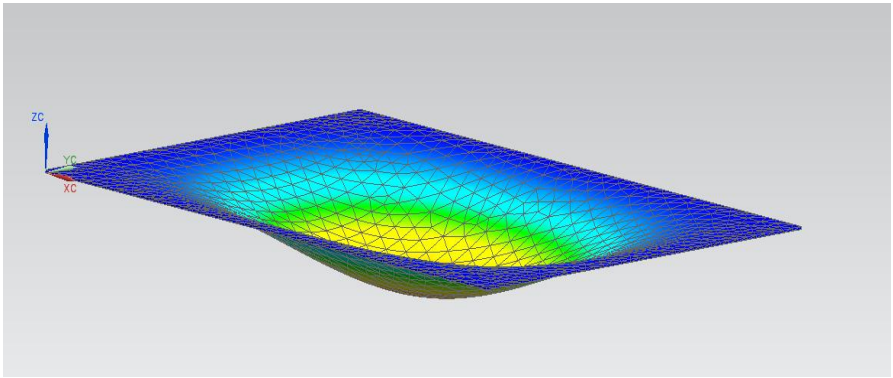

Figure 4.8 Mode shape (1,1) from FEM analysis

For a perfect mode shape (1,1), the maximum and minimum will happen at the centre of the plate with the displacement reducing evenly towards the edge. Thus, as can be seen in simulation at figure 4.8, every edge or the border of the plate shows the same displacement value which theoretically is

zero. Though, from the DIC figure 4.8 (image no. 18), the bottom of the peak is occuring in the centre, but there are small existing blue colours (representing z displacement downward) happening toward the left of the panel.

The odd lower displacement reading may happen due to the noise of the image resulting from extra dazzled light sources which are exposed by the shining plate because of scratches. Other possibility may be because of the non-uniformity in the nature of the boundary condition which may not be fully in “clamped” condition and / or a potential resulting pin join condition between each bolt. This is typical of the type of panel behaviour which will be likely seen in real life, as spot welds / adhesive joints rarely follow idealistic behaviour. This non-uniformity may also happen because of the possibility of additional vibration at the panel rig itself. The setup was done in fully anechoic chamber with all the setup was put on the wired mesh. Vibration from the shaker may have a small influence to vibrate the panel rig. In this sensitive optical camera DIC experiment, any small changes can influence the accuracy of measurement.

4.4.2 Second Mode (2, 1)

The graph in figure 4.9 below shows the sequence of a number of images taken respectively with the voltage provided to the shaker from the power amplifier for mode (2,1). The graph shows a series of selected images that represent the behaviour of the mode during the given frequency.

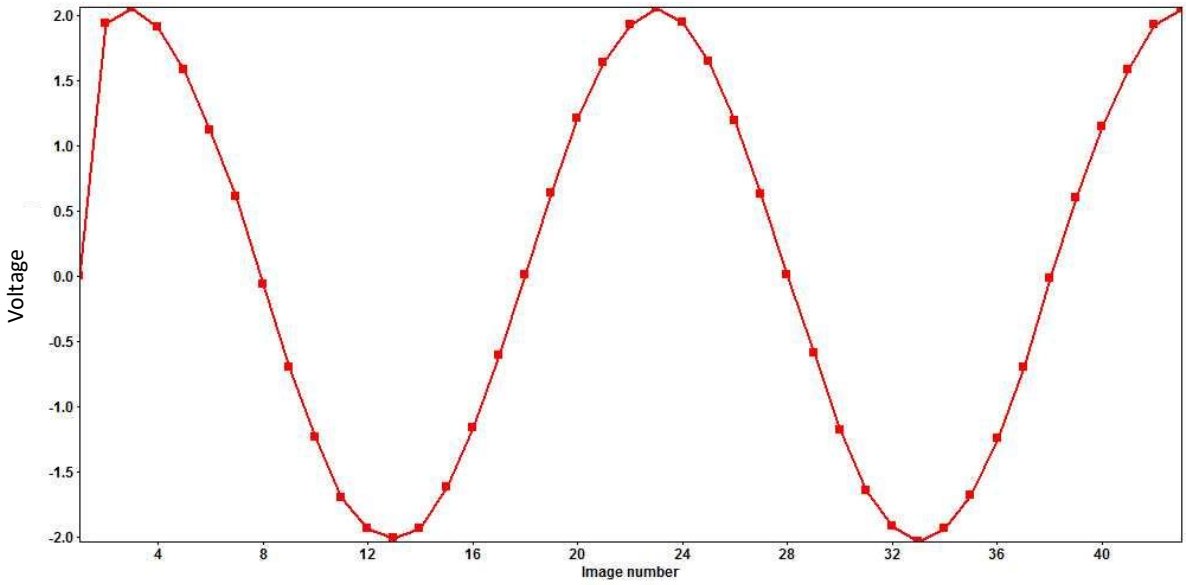

Figure 4.9: Graph number of image vs voltage value from shaker for mode (2,1)

The sequence of images in figure 4.10 below represent three images captured during the mode shape behaviour. The complete image of the cycle can be found at the Appendix. Image number 7 shows a value near 0 voltage expressing the neutral behaviour of the panel with deformation almost distributed evenly on the surface. Then, the voltages were decreasing and reach the lowest value. The minimum deflection of the plate can be seen at the lower part (blue colour) of the panel and the peak can be seen (red colour) at the maximum deflection of the panel as shown in image 13. Next, the voltages start increasing and reach at the highest value, the peak and bottom alternate oppositely from image 13 before as shown in image 24.

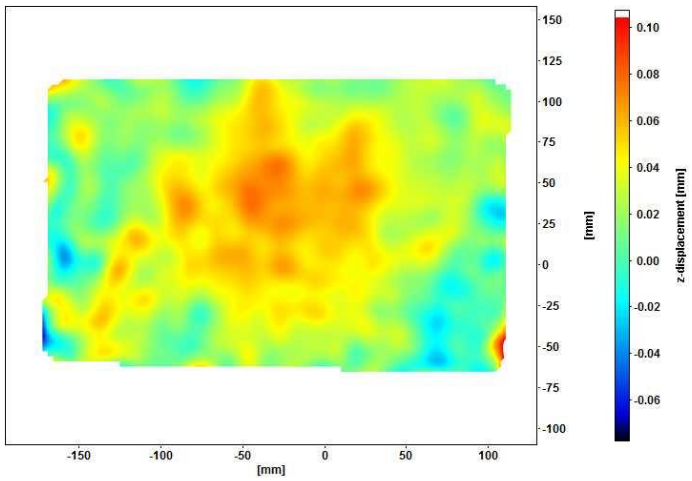	Image no 7
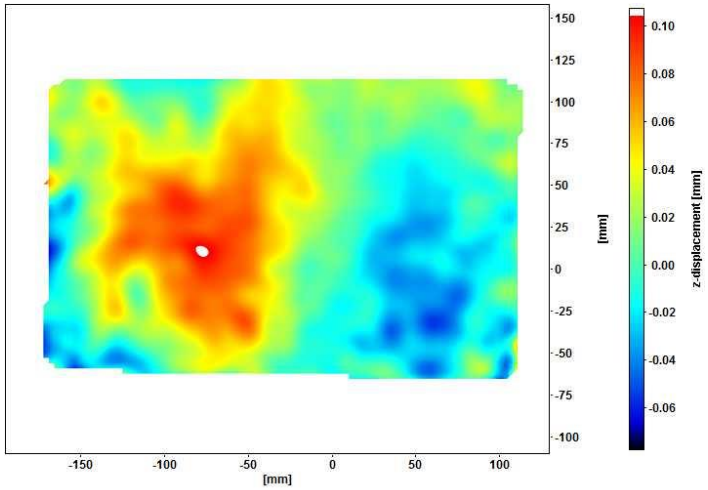	Image no 13
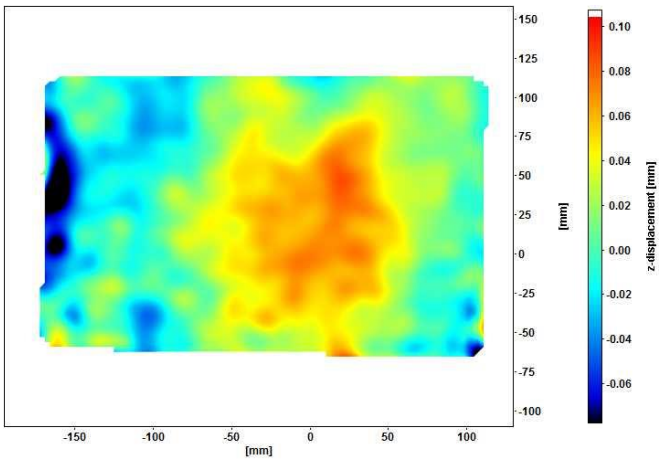	Image no 24

Figure 4.10: From top- image number 7, image number 13 and image number 24 for mode (2,1)

The behaviour captured by the DIC camera represent the same predicted mode shape results from the FEM simulation for mode (2,1) as shown in figure 4.11 below.

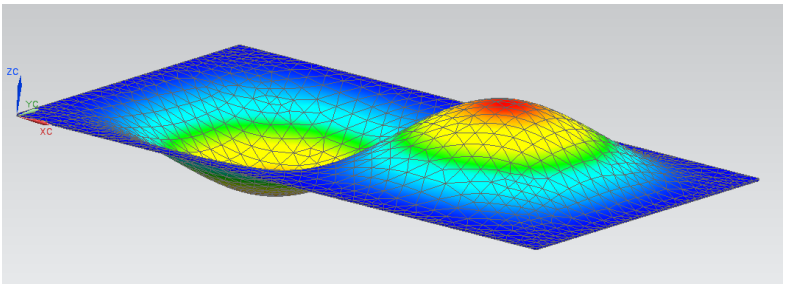

Figure 4.11 Mode shape (2,1) from FEM analysis

4.5 Conclusion

The digital image correlation has produced a good mode shape result when compared with simulation results. The nodal lines for mode (1, 1) and mode (2, 1) can be seen from the DIC result where the peak of the deformation is represented by a red colour and the corresponding bottom amplitude by the blue colour. For instance, from the mode (1, 1) result, image number 7 and 18 which is the position almost opposite each other on the amplitude against voltage graph, which produces a contrast result to show the movement of the mode shape from maximum to the minimum. The peak also happens at the centre of the plate. For mode (2,1), image number 13 and 24 show almost an opposite position where the peak can be seen at the left on image 13 and almost at the right on image 24. Thus, the DIC result can produce a good deflection or deformation product. In the next chapter, this information can be used to produce spatial average mean square velocity result.

The other major advantage of this monitoring is that it captures the non-uniformity in real structures, whereas the analytical models will always be idealistic test cases.

CHAPTER 5
RADIATION CHARACTERISTICS OF AUTOMOTIVE TYPE PANELS

5.1 Introduction

This chapter contains an initial discussion of what sound radiation is and what an experimental setup for measuring the sound power level (SPW) looks like for plate vibration. This SPW measurement from the experiment for each mode is compared and validated with predicted values calculated from the DIC measurements. A vehicle designer might well have prototype plates on vehicles or assemblies, often in a factory, industrial unit or design office. While it is possible to take direct sound pressure measurements, these are unlikely to be in anechoic environments. Indirectly inferring the sound pressure or sound power from visual methods (which are not affected by the background noise) allows the designer to have the option to predict the sound power just through the use of a camera setup.

To begin the prediction, the discussions continue by looking at the radiation efficiency for a plate. The theoretical value of radiation efficiency of two different types of boundary condition; baffled and unbaffled for a simply supported case have been elaborated. Moreover, the discussion continues with comparing the radiation efficiency for the baffled case between simply supported and clamped edges for each different modes. This radiation efficiency value of the baffled case will be used together as one of the parameters to predict a numerical SPW. In addition, the other parameter to calculate SPW is the spatial average mean square velocity.

Thus, the section continues by proposing a method and calculation of spatial mean average velocity of a plate based on the different displacement locations for a set sequence of image generated from the DIC for each mode. This calculated spatial mean average velocity together with the theoretical value of radiation efficiency with respect to each mode will be used as a basic calculation to predict the SPW.

Finally, the predicted SPW values will be compared back with the measured SPW value from the experiment. To conclude, this chapter will end by discussing the differences between predicted and measured SPW values.

5.2 Radiation Efficiency for Baffled Plate

The radiation efficiency is defined as the ratio of the acoustic power radiated by an arbitrary vibrating surface with a vibrating flat surface having the same surface area. The radiation efficiency of a plate is a substantial indicator in noise and vibration control since it not only provides information on the response of a plate due to random excitation but also on the radiated sound power from the structure. It can be represented in mathematic as [119,120,121]:

$$\sigma = \frac{W}{\rho c S \langle \overline{v^2} \rangle} \tag{5.1}$$

Where W is the acoustic power, ρ is the density of medium enclosing the structure, c is the speed of the sound in the fluid, S is the surface area of the structure, $\langle \overline{v^2} \rangle$ is the spatially averaged mean square velocity of the plate and $\langle .. \rangle$ denotes a spatial average.

The radiation efficiency depends on the structure dimension and shape, density and speed of sound in the medium, the nature of the boundary conditions and distribution of vibration velocity over the surface. As a general rule, the value of the radiation efficiency is small at lower frequencies ($\sigma << 1$) and tends towards unity with the increasing frequency.

5.2.1 Theory of the Radiation Efficiency of a Baffled Plate

In order to understand how the mathematics is formulated, consider the complex acoustic pressure in the far-field represented by Rayleigh's [122] equation towards of a plate or panel. A panel, simply supported in infinite baffle is assumed to be vibrating with simple harmonic motion in one of its natural modes and can be given by:

$$p(\boldsymbol{r}) = \frac{jk\rho c}{2\pi} \int_s v(\boldsymbol{x}) \frac{e^{-jkr'}}{r'} d\boldsymbol{x} \tag{5.2}$$

where ρ is the air density, c is the speed sound, $v(\boldsymbol{x})$ is the complex surface velocity amplitude at location $\mathbf{x} = (x,y)$, $k = \omega/c$ is the acoustic wave number, S denotes the surface area of the plate and $r' = |\boldsymbol{r} - \boldsymbol{x}|$, the distance from the source point to the acoustic response point. By integrating the far acoustic intensity over a hemisphere of radius **r**, the total acoustic power radiated from the plate can be obtained as:

$$W = \int_0^{2\pi} \int_0^{\frac{\pi}{2}} \frac{|p(\boldsymbol{r})|^2}{2\rho c} r^2 sin\theta \, d\theta \, d\emptyset \tag{5.3}$$

With $p(\boldsymbol{r})$ is the complex acoustic pressure amplitude at a location in space expressed in spherical coordinates, $\boldsymbol{r} = (r, \theta, \emptyset)$ at frequency ω.

At any location **x** on the structure, the complex velocity surface can be found by considering modal contribution as:

$$v(x) = \sum_{m=1}^{\infty} \sum_{n=1}^{\infty} v_{mn} \varphi_{mn}(x) \tag{5.4}$$

Where v_{mn} is the complex velocity amplitude of the mode (m,n), φ_{mn} (**x**) is the value of the associated mode shape function at the location **x**, m and n indices the modes. The mode shape function φ_{mn} (**x**) for simply supported plate can be written as:

$$\varphi_{mn}(x,y) = \sin\left(\frac{m\pi x}{a}\right) sin\left(\frac{n\pi y}{b}\right) \tag{5.5}$$

With a is the dimension of the plate in x direction and b dimension in y direction. Substituting equation 5.4 into 5.2, the acoustic pressure is given by;

$$p(\boldsymbol{r}) = \frac{jk\rho c}{2\pi} \int \sum_{m=1}^{\infty} \sum_{n=1}^{\infty} v_{mn} \varphi_{mn}(x) \frac{e^{-jkr'}}{r} dS \tag{5.6}$$

Rearrange and it will become

$$p(\boldsymbol{r}) = \sum_{m=1}^{\infty}\sum_{n=1}^{\infty} v_{mn}\left\{\frac{jk\rho c}{2\pi}\int \varphi_{mn}(x)\frac{e^{-jkr\prime}}{r}dS\right\} \tag{5.7}$$

Or it also can be expressed as;

$$p(\boldsymbol{r}) = \sum_{m=1}^{\infty}\sum_{n=1}^{\infty} v_{mn}\, A_{mn}(\boldsymbol{r}) \tag{5.8}$$

Wallace [120],has produced an analytical solution for the integral in the brackets, $A_{mn}(\boldsymbol{r})$ which will result

$$A_{mn}(\boldsymbol{r}) = jk\rho c\frac{e^{-jkr}}{2\pi r}\frac{ab}{\pi^2 mn}\left[\frac{(-1)^m e^{j\alpha}-1}{\left(\frac{\alpha}{m\pi}\right)^2-1}\right]\left[\frac{(-1)^n e^{j\beta}-1}{\left(\frac{\beta}{n\pi}\right)^2-1}\right] \tag{5.9}$$

With α = *ka sin* θ *cos* φ and *β= kb sin* θ *sin* φ, while r is $|\boldsymbol{r}|$ **.**

Next, since $p.p^*=|p|^2$ (related with equation 5.3) the total acoustic power radiated from the plate can be obtained by integrating the far-field acoustic intensity by substituting 5.8 in 5.3 [123]:

$$W = \int_0^{2\pi}\int_0^{\pi/2} \frac{p(\boldsymbol{r})p^*(\boldsymbol{r})}{2\rho c} r^2\, d\theta\, d\emptyset$$

$$W = \int_0^{2\pi}\int_0^{\pi/2} \frac{\sum_{m=1}^{\infty}\sum_{n=1}^{\infty} v_{mn}\, A_{mn}(\boldsymbol{r})\sum_{m\prime=1}^{\infty}\sum_{n\prime=1}^{\infty} v *_{m\prime n\prime} A *_{m\prime n\prime}(\boldsymbol{r})}{2\rho c} r^2\, d\theta\, d\emptyset$$

$$W = \sum_{m=1}^{\infty}\sum_{n=1}^{\infty}\sum_{m'=1}^{\infty}\sum_{n'=1}^{\infty} v_{mn} v \; *_{m'n'}\left\{\int_0^{2\pi}\int_0^{\pi/2} \frac{A_{mn}(\boldsymbol{r})A *_{m'n'}(\boldsymbol{r})}{2\rho c} r^2\, d\theta\, d\emptyset\right\} \tag{5.10}$$

Where $p^*(r)$ is the conjugate of the sound $p(r)$, m' and n' are used to distinguish m and n in the conjugate. From equation 5.10, it can be seen that total radiated power depends on the involvement of combination modes. The involvement is usually denoted as self-modal radiation for $m = m'$ and $n = n'$ and cross-modal radiation for either $m \neq m'$ and $n \neq n'$.

5.2.2 Response to Point Force

Consider a point force applied to a plate at location (x_0, y_0). Creamer [121] states that the modal velocity amplitude is given by:

$$v_{mn} = \frac{j\omega P \varphi_{mn}(x_0, y_0)}{[\omega^2{}_{mn}(1 - j\eta) - \omega^2]M_{mn}} \tag{5.11}$$

Where ω_{mn} is the natural frequency, P is the force amplitude, η is the damping loss factor, M_{mn} is the modal mass and φ_{mn} is the mode shape function. The modal mass for a simply supported plate is given by

$$M_{mn} = \int_s \rho_s h \, \varphi^2{}_{mn}(x, y) dS = \frac{1}{4}\rho_s hab = \frac{M}{4} \tag{5.12}$$

With ρ_s is plate density and h is the thickness of the plate. M is the mass of the plate and φ_{mn} is the form of simply supported from equation 5.7.

The natural frequencies, ω_{mn} are given by;

$$\omega_{mn} = \left(\frac{B}{\rho_s h}\right)^{1/2} \left[\left(\frac{m\pi}{a}\right)^2 + \left(\frac{n\pi}{b}\right)^2\right] \tag{5.13}$$

With B being the bending stiffness of the plate.

In order to determine general guideline for total radiated power, the average of all the possible locations of the uncorrelated point forces on the plate is considered. The average total radiated power can be written as (G.Xie [122]):

$$\bar{W} = \frac{1}{ab}\int_0^a \int_0^b W dx_0 dy_0$$

$$\bar{W} = \sum_{m=1}^{\infty}\sum_{n=1}^{\infty}\sum_{m'=1}^{\infty}\sum_{n'=1}^{\infty}\left\{\frac{1}{ab}\int_0^a\int_0^b v_{mn}v^*{}_{m'n'}dx_0dy_0 \int_0^{2\pi}\int_0^{\pi/2}\frac{A_{mn}(\boldsymbol{r})A^*{}_{m'n'}(\boldsymbol{r})}{2\rho c}r^2\,d\theta\,d\emptyset\right\} \quad (5.14)$$

Where

$$\int_0^a\int_0^b v_{mn}v^*{}_{m'n'}dx_0dy_0 = \int_0^a\int_0^b\left[\frac{j\omega P\varphi_{mn}(x_0,y_0)}{[\omega^2{}_{mn}(1-j\eta)-\omega^2]M_{mn}} - \frac{j\omega P\varphi_{m'n'}(x_0,y_0)}{[\omega^2{}_{m'n'}(1-j\eta)-\omega^2]M_{m'n'}}\right]dx_0dy_0$$

However, because of the orthogonality of Eigen functions,

$$\int_0^a\int_0^b \varphi_{mn}(x_0,y_0)\,\varphi_{m\prime n\prime}(x_0,y_0)\,dx_0dy_0 = 0 \qquad \text{for } m = m' and\ n = n'.$$

And equation 5.14 can be simplified as:

$$\bar{W} = \sum_{m=1}^{\infty}\sum_{n=1}^{\infty}\left\{\frac{1}{ab}\int_0^a\int_0^b v_{mn}v^*{}_{m'n'}dx_0dy_0 \int_0^{2\pi}\int_0^{\pi/2}\frac{A_{mn}(\boldsymbol{r})A^*{}_{m'n'}(\boldsymbol{r})}{2\rho c}r^2\,d\theta\,d\emptyset\right\} \quad (5.15)$$

Where each term is in the sum of the power radiated by single mode and it can be written as:

$$\bar{W} = \sum_{m=1}^{\infty}\sum_{n=1}^{\infty}\bar{W}_{mn} \quad (5.16)$$

With $\bar{W}_{mn}$ is expressed as

$$\bar{W} = \overline{|v_{mn}|^2} \int_0^{2\pi} \int_0^{\pi/2} \frac{A_{mn}(\boldsymbol{r}) A^*{}_{m'n'}(\boldsymbol{r})}{2\rho c} r^2 \, d\theta \, d\emptyset \tag{5.17}$$

Where $\overline{|v_{mn}|^2}$ is the modulus squared of the velocity amplitude v_{mn}, averaged over all the force position.

The average modulus squared of the velocity amplitude$\overline{|v_{mn}|^2}$ is given by

$$\overline{|v_{mn}|^2} = \frac{1}{ab} \int_0^a \int_0^b v_{mn} v^*{}_{mn} \, dx_0 dy_0$$

$$= \frac{1}{ab} \int_0^a \int_0^b \frac{\omega^2 P^2 \varphi^2{}_{mn}(x_0, y_0)}{[(\omega^2{}_{mn} - \omega^2) + \eta^2 \omega^4] M^2{}_{mn}} dx_0 dy_0$$

$$= \frac{\omega^2 P^2}{ab\rho_p h[(\omega^2{}_{mn} - \omega^2)^2 + \eta^2 \omega^4] M_{mn}}$$

$$= \frac{4\omega^2 P^2}{M^2[(\omega^2{}_{mn} - \omega^2)^2 + \eta^2 \omega^4]} \tag{5.18}$$

The power radiated by the mode (*m*,*n*) can also be represented by radiation efficiency terms based from equation 5.1.

$$\bar{W} = \sigma_{mn} \rho c ab \overline{\langle v_{mn}{}^2 \rangle} \tag{5.19}$$

Where $\overline{\langle v_{mn}{}^2 \rangle}$ represents spatially-averaged mean square velocity in mode (*m*,*n*) averaged over all possible force position.

In order to calculate $\langle\overline{\overline{v_{mn}{}^2}}\rangle$, it is required to first know $\langle\overline{v_{mn}{}^2}\rangle$.The spatially-averaged mean square velocity amplitude in mode (*m*,*n*) due to a point force at (x_0,y_0) is defined by

$$\langle\overline{v_{mn}{}^2}\rangle = \frac{1}{S}\int_S \left[\frac{1}{T}\int_0^T |v_{mn}(x,y,t)|^2\right] dS \tag{5.20}$$

With *T* is the period of time over which to estimate the mean square velocity at any position on the plate, and S is the area of the plate. Next, for simplification, consider the application for a current simply supported case and with $v_{mn}$from equation (5.11), the equation will become:

$$\langle\overline{v_{mn}{}^2}\rangle = \frac{1}{S}\int_S \left[\frac{1}{2}|v_{mn}(x,y)|^2\right] dxdy$$

$$= \frac{1}{2S}|v_{mn}|^2 \int_S \varphi^2{}_{mn}(x,y)\, dxdy$$

$$= \frac{1}{8}|v_{mn}|^2$$

$$= \frac{1}{8}\frac{\omega^2 P^2 \varphi^2{}_{mn}(x_0,y_0)}{[(\omega^2{}_{mn}-\omega^2)^2+\eta^2\omega^4]M^2{}_{mn}} \tag{5.21}$$

If the average is taken over all possible force location, the average spatially-averaged mean square velocity is given by

$$\langle\overline{\overline{v_{mn}{}^2}}\rangle = \frac{1}{S}\int_S \langle\overline{v_{mn}{}^2}\rangle\, dx_0 dy_0$$

$$= \frac{1}{S}\int_S \frac{1}{8}\frac{\omega^2 P^2 \varphi^2{}_{mn}(x_0,y_0)}{[(\omega^2{}_{mn}-\omega^2)^2+\eta^2\omega^4]M^2{}_{mn}}\, dx_0 dy_0$$

$$= \frac{1}{8M} \frac{\omega^2 P^2}{[(\omega^2{}_{mn} - \omega^2)^2 + \eta^2\omega^4] M_{mn}} \tag{5.22}$$

With $M_{mn} = \frac{M}{4}$ from equation (5.12), it will become:

$$= \frac{1}{2M^2} \frac{\omega^2 P^2}{[(\omega^2{}_{mn} - \omega^2)^2 + \eta^2\omega^4]} \tag{5.23}$$

From equation (5.23) and (5.18), it can be seen that

$$8\,\overline{\langle \overline{v_{mn}{}^2} \rangle} = \overline{|v_{mn}|^2} \tag{5.24}$$

The equation mentioned by Xie [122] in (5.24) has a good similarity with the calculation made by Wallace [120].

After obtaining the total radiated power in the expression of summation of mode radiated power, the average radiation efficiency can be rewritten from the equation (5.1) to become:

$$\sigma = \frac{\sum_{m=1}^{\infty} \sum_{n=1}^{\infty} \overline{W}_{mn}}{\rho cab \overline{\langle \overline{v^2} \rangle}}$$

$$= \frac{\sum_{m=1}^{\infty} \sum_{n=1}^{\infty} \rho cab \sigma_{mn} \overline{\langle \overline{v_{mn}{}^2} \rangle}}{\rho cab \overline{\langle \overline{v^2} \rangle}}$$

$$= \frac{\sum_{m=1}^{\infty} \sum_{n=1}^{\infty} \sigma_{mn} \overline{\langle \overline{v_{mn}{}^2} \rangle}}{\overline{\langle \overline{v^2} \rangle}} \tag{5.25}$$

Where according to Cremer et.al [121], $\overline{\langle \overline{v^2} \rangle}$ is the result of summation of the average spatial modal square velocity $\overline{\langle \overline{v_{mn}{}^2} \rangle}$ averaged over forcing location.

$$\overline{\langle \overline{v^2} \rangle} = \frac{\omega^2 P^2}{2M^2} \sum_{m=1}^{\infty} \sum_{n=1}^{\infty} \frac{1}{[(\omega^2{}_{mn} - \omega^2)^2 + \eta^2\omega^4]}$$

$$= \sum_{m=1}^{\infty} \sum_{n=1}^{\infty} \overline{\langle v_{mn}{}^2 \rangle} \tag{5.26}$$

Equation (5.26) indicates that, as the cross-modal contributions vanish due to averaging over forcing locations, the modal responses are uncorrelated. In other words, the modes act individually, and are all excited with the same input power.

Thus, the average radiation efficiency in equation 5.25 will become:

$$\sigma = \frac{\sum_{m=1}^{\infty} \sum_{n=1}^{\infty} \sigma_{mn} [(\omega^2{}_{mn} - \omega^2)^2 + \eta^2 \omega^4]^{-1}}{\sum_{m=1}^{\infty} \sum_{n=1}^{\infty} [(\omega^2{}_{mn} - \omega^2)^2 + \eta^2 \omega^4]^{-1}} \tag{5.27}$$

From equation (5.27) it can be noted that the average radiation efficiency depends only on the self-modal radiations due to the averaging over all possible force locations.

5.2.3 Radiation Efficiency and Spatially Averaged Mean Square Velocity for the case of a plate which has baffled boundary conditions

A MATLAB program has been produced to evaluate equation (5.27) and equation (5.26) for average multi-mode for radiation efficiency and spatially averaged mean square velocity. However, to calculate the equation, radiation efficiency for single mode need to be calculated first based from Wallace equation as shown in equation (5.30) and the coding using Matlab is shown in the Appendix .The dimension of the rectangular plate is 0.297 x 0.198m with thickness of 1.2mm and simply supported boundary condition. The damping loss factor is assumed to be 0.1, which is higher than just the material loss factor, but it is assumed that the boundary conditions reduce the amplitude of incident waves due to microfriction close to the edge thus, density 7817 kg/m^3 and Young's Modulus 2.05 x 10^{11} N/m^2. The calculations are carried out in the frequency range between 1Hz until 10 kHz. Three selective early modes, mode (1, 1), mode (2, 1) and mode (2, 2) were also shown as examples and later become a base for parameter values that can be used in predicting the radiation power.

Mode (1, 1)

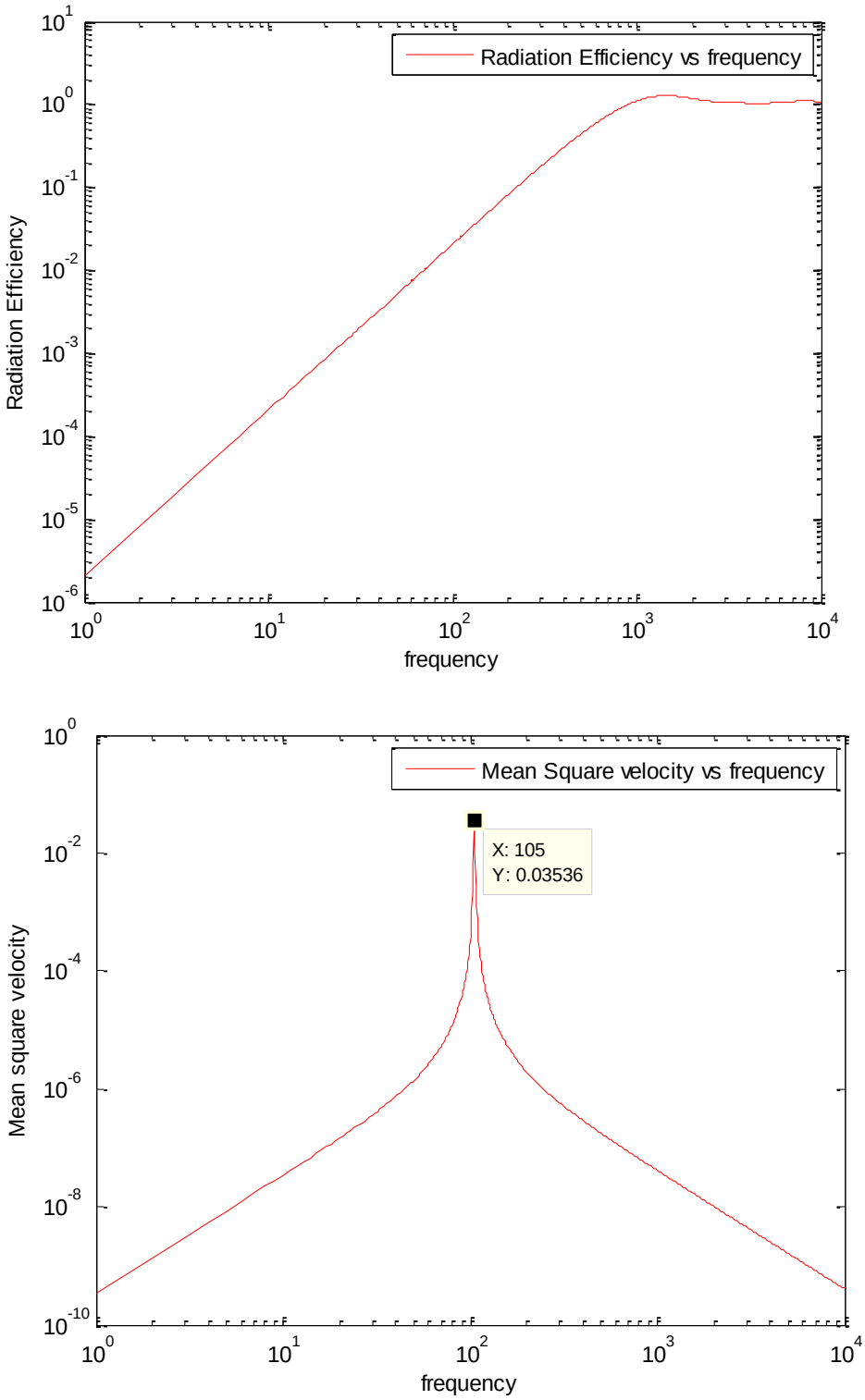

Figure 5.1: Radiation efficiency and spatially averaged mean square velocity for mode (1, 1)

From Figure 5.1, which shows spatially averaged mean square velocity, it can be seen that the peak for the mean-square velocity point will occur at the resonance frequency for the plate. The value will increase exponentially until it reaches the peak, the first resonance which is the first mode, (1, 1) at 105Hz and later will drop exponentially.

On radiation efficiency, there will be a big difference in the amplitude of radiation efficiency for lower frequencies (below 1000Hz). The value will increase from 10^{-6} to 1 and become approximately constant which means at higher frequencies, the ratio of the acoustic power radiated by a vibrating surface compared with a vibrating flat surface for the same area (sound radiation value) is the same.

Mode (2, 1)

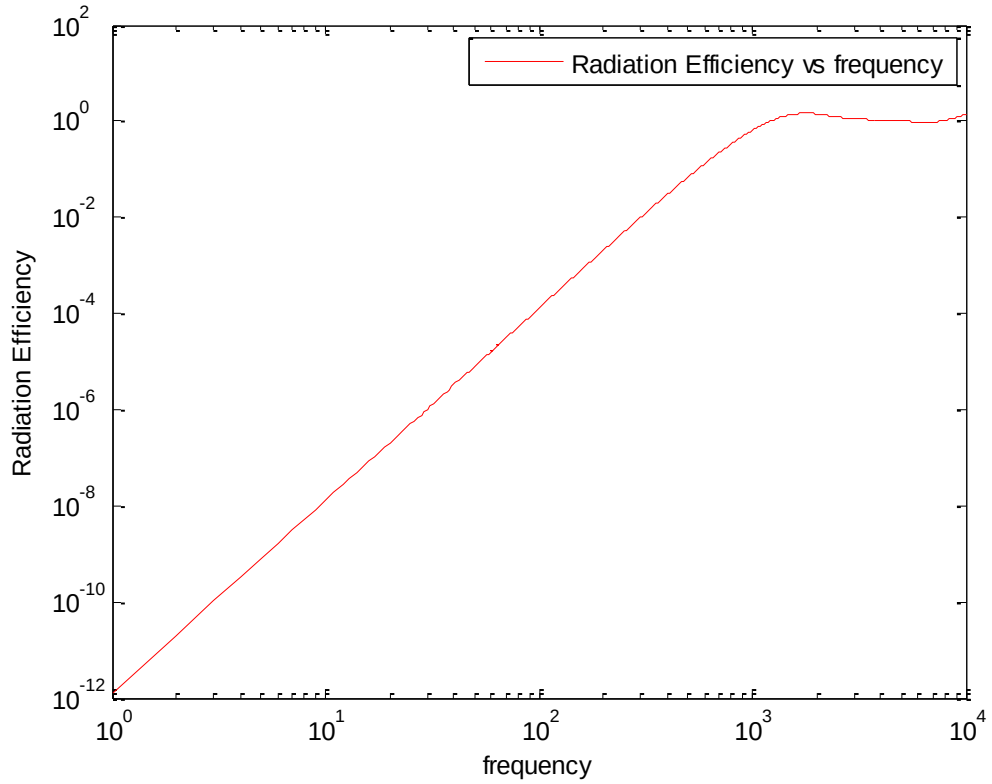

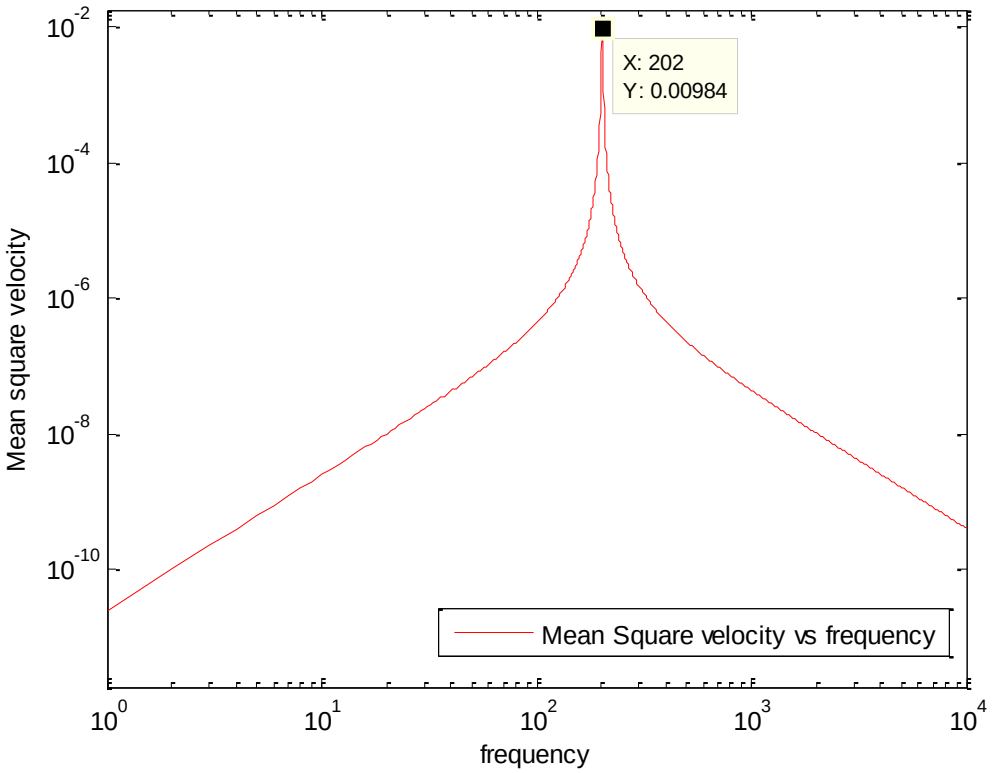

Figure 5.2: Radiation efficiency and spatially averaged mean square velocity for mode (2, 1)

Mode (2, 2)

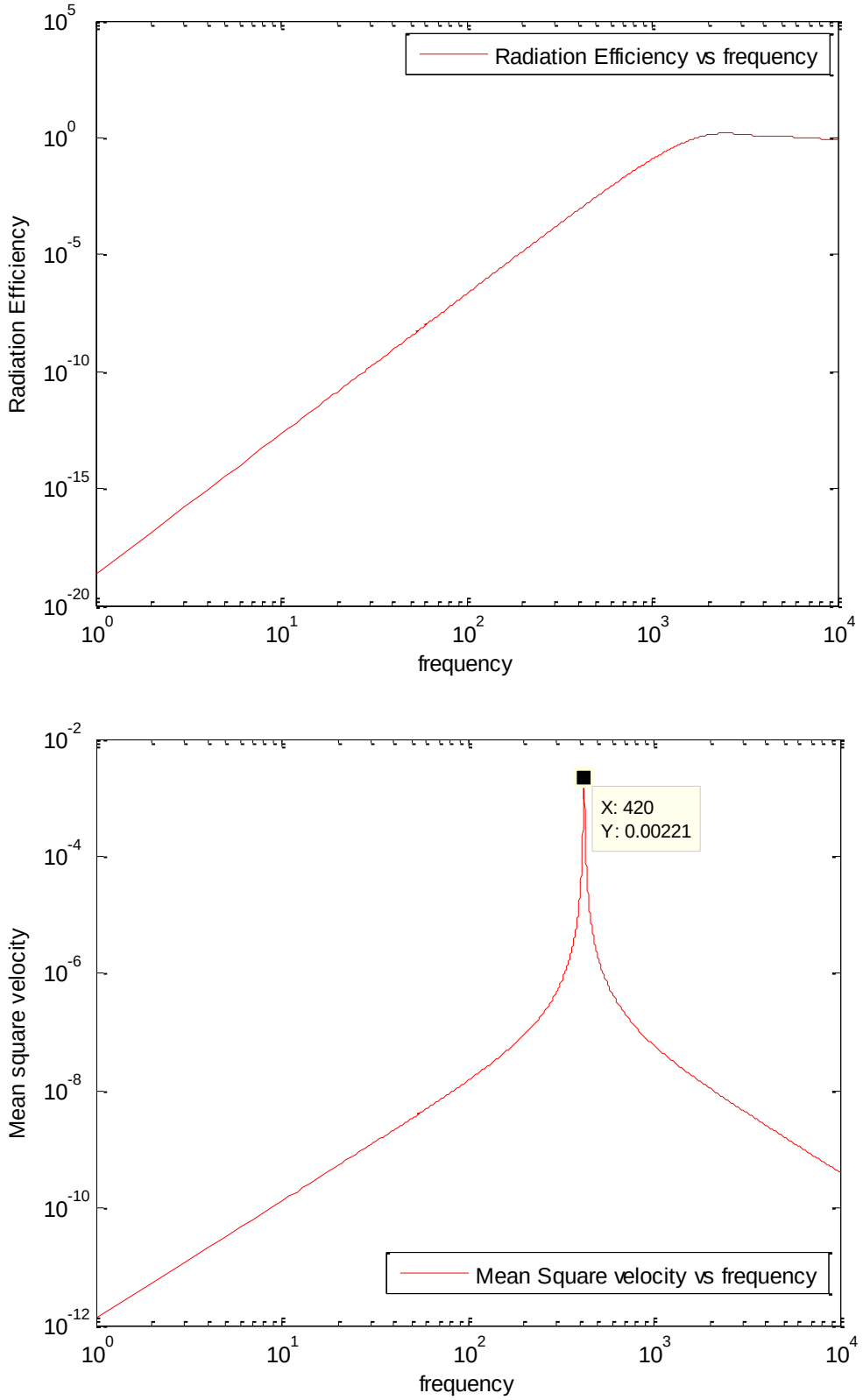

Figure 5.3: Radiation efficiency and spatially averaged mean square velocity for mode (2, 2)

Figure 5.2 and 5.3, showing the spatially averaged mean square velocity; this shows the same result with as Figure in 5.1. The peak for the mean-square velocity point for both modes will occur at the respective resonance frequency for the plate. The value will increase exponentially until reach at the peak, for mode (2,1) is at 202 Hz and mode (2,2) at 402 Hz,and later will drop exponentially.

On radiation efficiency, there is a significant difference in radiation efficiency for lower frequencies (below 1000 Hz). When the mode number is increasing, the difference in radiation efficiency at lower frequencies becomes bigger. The value will increase from 10^{-12} to 1 and 10^{-20} to 1 for mode (2,1) and mode (2,2) correspondingly.

Average of multi modal mode

As previously discussed, the MATLAB program has been programmed to evaluate equations (5.26) and (5.27) to provide the average multi-mode for radiation efficiency and spatially averaged mean square velocity. In theory, the average radiation efficiency over many modes can be analysed. The frequency resolution is one point for every frequency, which is sufficient to resolve the amplitude of a metal plate with a low loss factor.

However, to calculate the sound power using the equation, the value of σ_{mn} needs to be found first through rearrangement of 5.19

$$\sigma_{mn} = \frac{\bar{W}}{\rho c a b \langle \overline{\overline{v_{mn}{}^2}} \rangle} \tag{5.28}$$

Equation 5.28 then can be solved by using equation 5.17, 5.18 and 5.23 to yield

$$\sigma_{mn} = \frac{4 \int_0^{2\rho c} \int_0^{\pi/2} A_{mn}(\boldsymbol{r}) A^*{}_{m'n'}(\boldsymbol{r}) r^2 \, d\theta \, d\emptyset}{(\rho c)^2 a b} \tag{5.29}$$

After some algebraic manipulation to equation 5.18, according to the expression given by Wallace [120], the modal radiation efficiency σ_{mn} is

$$\sigma_{mn} = \frac{64k^2ab}{\pi^6 m^2 n^2} \int_0^{\pi/2} \int_0^{\pi/2} \left\{ \frac{\begin{matrix} cos \\ sin \end{matrix}\left(\frac{\alpha}{2}\right) \begin{matrix} cos \\ sin \end{matrix}\left(\frac{\beta}{2}\right)}{\left[\left(\frac{\alpha}{m\pi}\right)^2 - 1\right]\left[\left(\frac{\beta}{n\pi}\right)^2 - 1\right]} \right\}^2 \sin\theta d\theta d\vartheta \qquad (5.30)$$

The shape factor *cos* $\left(\frac{\alpha}{2}\right)$ is used when *m* is an odd integer and *sin* $\left(\frac{\alpha}{2}\right)$ is used when *m* is an even integer. Similarly *cos* $\left(\frac{\beta}{2}\right)$ is used when *n* is an odd integer and *sin* $\left(\frac{\beta}{2}\right)$ is used when *n* is an even integer. $\alpha = \sin\theta\cos\vartheta$ and $\beta = \sin\theta\sin\vartheta$ with $k = \frac{\omega}{c}$ being the wave number.

The approximate expression for the modal radiation efficiencies from equation 5.30 at arbitrary frequencies below the critical frequency were also given by Wallace [120] as

$$\sigma_{mn} \cong \frac{32(ka)(kb)}{\pi^5 m^2 n^2}\left\{1 - \frac{k^2 ab}{12}\left[\left(1 - \frac{8}{(m\pi)^2}\right)\frac{a}{b} + \left(1 - \frac{8}{(n\pi)^2}\right)\frac{b}{a}\right]\right\} \qquad 5.31$$

$$\sigma_{mn} \cong \frac{8(ka)(kb)^3}{\pi^5 3m^2 n^2}\left\{1 - \frac{k^2 ab}{20}\left[\left(1 - \frac{8}{(m\pi)^2}\right)\frac{a}{b} + \left(1 - \frac{24}{(n\pi)^2}\right)\frac{b}{a}\right]\right\} \qquad 5.32$$

$$\sigma_{mn} \cong \frac{2(ka)^2(kb)^3}{\pi^5 15m^2 n^2}\left\{1 - \frac{5k^2 ab}{64}\left[\left(1 - \frac{24}{(m\pi)^2}\right)\frac{a}{b} + \left(1 - \frac{24}{(n\pi)^2}\right)\frac{b}{a}\right]\right\} \qquad 5.33$$

Equation 5.31 is used when *m,n* is odd, 5.32 when *m* is odd and *n* is even, 5.33 when *m,n* is even. From the power of *k* in these expressions, it can be seen that odd-odd modes are most effective in radiation and even-even modes are least effective. From a visual point of view, it may be because of the odds are symmetrical so the plate moves in one direction while the evens are asymmetrical so one side of the plate cancels the other, generating a directional dipole sound field.

Figure 5.4 represent the total spatially averaged mean square velocity in red colour and the spatially averaged mean square velocity for each mode for the rectangular plate with a unit of force amplitude for each blue line respectively. The infinite numbers of modes in the equation are truncated to a finite number. For this example rectangular plate, 50 modes with natural frequencies below 10 kHz are included in the calculation.

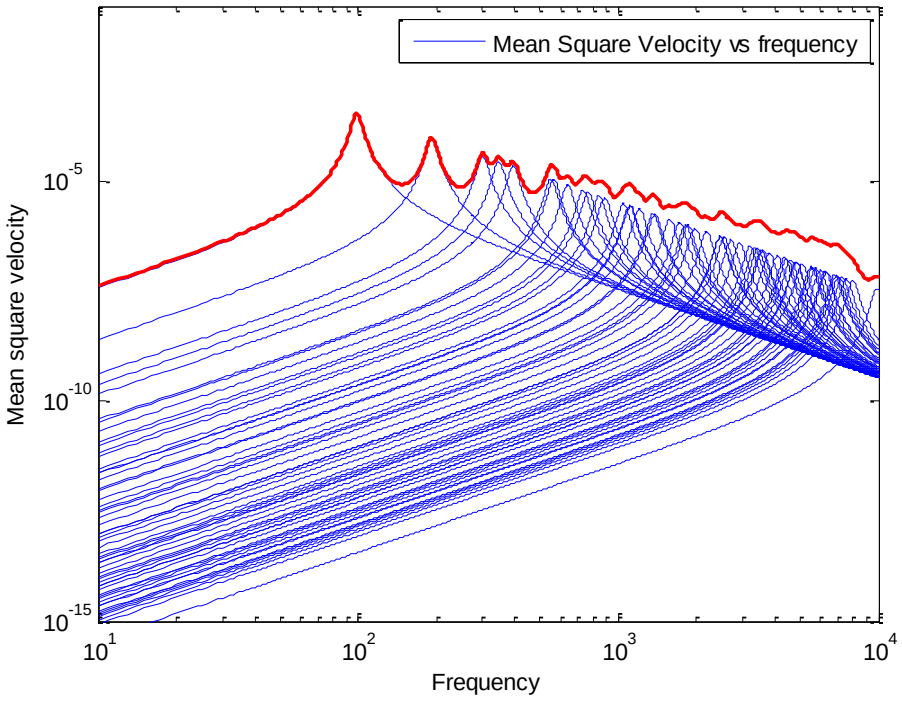

Figure 5.4 Theoretical mean square velocity (m^2/s^2) vs frequency for plate 1.2mm (0.297x0.198x0.0012)) baffle case- simply supported *(blue colour – modal mean square velocity, red colour – total mean square velocity)*

It can be seen that the higher the mode number, the lower the overall mean square velocity is for a given frequency. This illustrates the industrial problem of sound damping, that the lowest mode numbers with the longest wavelengths contain the largest normal velocity which leads to sound propagation. The radiation efficiency just contains information on how efficiently this velocity is translated into acoustic energy.

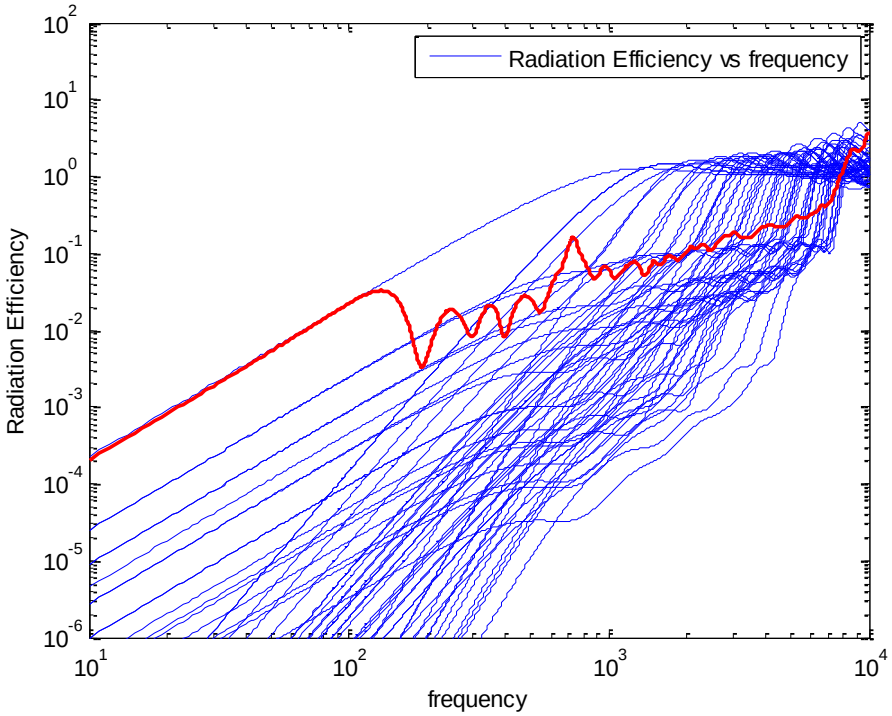

Figure 5.5 Theoretical radiation efficiency vs frequency for plate 1.2mm (0.297x0.198x0.0012)) baffle case- simply supported *(blue colour – modal radiation efficiency, red colour – Average radiation efficiency)*

From Figure 5.5, it can be seen that below 105 Hz, the radiation efficiency of the first mode, determines the overall result. This is due to the dominance of this mode in the response and high value of σ_{mn}. There are a number of spikes in the red line around 800 Hz and it may due to the non-square plate having certain modes in different directions that have similar natural frequencies. Therefore, a form of constructive interference in the overall radiation efficiency for a given frequency can be seen.

5.3 Radiation Efficiency for Baffled Plate

Generally, in practice, vibrating plates are not always set in a baffled boundary condition and therefore the case for an unbaffled plate is also important. In terms of sound propagation from automotive structures, plates and panels will have arbitrary boundary conditions, therefore it is important to consider the two extreme cases. When the sound field from one side can have an interaction with the other side, the plate can be categorised as unbaffled. For an unbaffled plate,

the particle velocity is not known at the outer side of the plate region, but assuming only flexural vibration and no damping material (or porous coverings), one assumption could be that the two velocities are identical and it has an interaction between the other. However, in the baffled plate, the particle velocity is known as zero at the boundaries. This makes the task to solve the sound radiation for an unbaffled case more complex compared with the baffled plate case.

Laulagnet [124] proposed a numerical evaluation for the sound radiation problem relating to a baffled plate with a simply supported end condition. This solution did not neglect the pressure jump in the plate velocity over a wide frequency range. This method is explained in the section 5.3.1 below.

The goal is to find the sound pressure level from a plate given a theoretical sound radiation efficiency and an experimentally calculated mean square velocity for the plate surface from the DIC experiment. The next section provides a method to obtain and achieve this goal. It is required so that comparisons can be made later from sound power prediction with the experimental results of section 3.6.

5.3.1 Radiation Efficiency Unbaffle Plate Theory

Consider a flat thin plate, located in the xy plane and located at *z*=0, excited by a harmonic driving force of angular frequency ω. The plate is unbaffled, with a surface area of S_p and the acoustic medium is infinite. The classical equation of flexural waves due to the force normal to the normal plate is given by:

$$D\nabla^4 w(x,y) - m_p\omega^2 w(x,y) = F(x,y) + \Delta p(x,y) \qquad (5.33)$$

Where *D* is the bending stiffness or rigidity modulus, m_p is the mass per unit area, *w(x,y)* is the transverse displacement of the plate, $\Delta p(x,y)$ the difference of the acoustic surface pressure. The expression of pressure jump is given by;

$$\Delta p(x,y) = p^{-}(x,y) - p^{+}(x,y) \tag{5.34}$$

Where $p^{-}(x,y)$and $p^{+}(x,y)$ are respectively the surface pressure on the *z* negative and *z* positive of the plate.

The symbol ∇^4 is given by

$$\nabla^4 = \frac{\partial^4}{\partial x^4} + \frac{2\partial^4}{\partial x^2 \partial y^2} + \frac{\partial^4}{\partial y^4} \tag{5.35}$$

Based from the classical homogeneous Helmholtz equation, the acoustic pressure is

$$\nabla^2 p(x,y,z) + k^2 p(x,y,z) = 0 \tag{5.36}$$

With *p(x,y,z)* is the acoustic pressure anywhere in the acoustic fluid, *k* the acoustics wave number ω/c, *c* is the sound velocity and ∇^2 is the Laplacian operator. The continuity between the normal acceleration of the plate and the fluid particle is given by Euler's equation:

$$\left.\frac{\partial p(x,y,z)}{\partial z}\right|_{z=0} = \rho_0 \omega^2 w(x,y) \tag{5.37}$$

The pressure anywhere in the volume entirely closing the plate can be found by applying Green's formula, see figure 5.6.

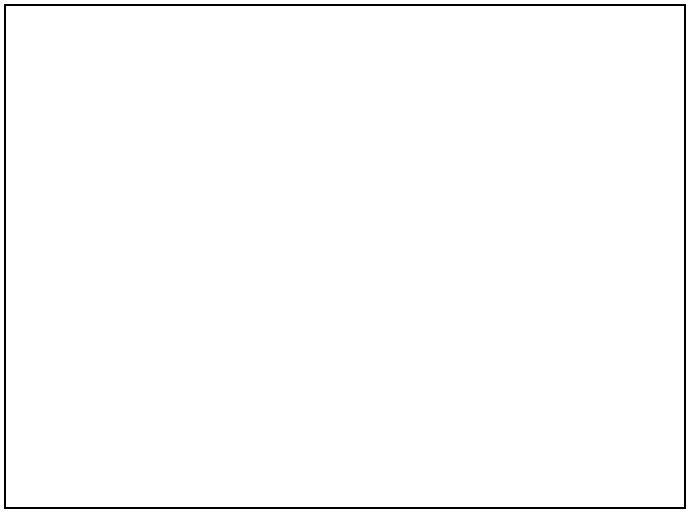

Figure 5.6 Image of a schematic view of the supported plate in the volume V with bounding surface area S_v. (taken from ref. [125])

$$p(M) = \int_{S_v} \left(\frac{\partial G}{\partial n_Q}(Q,M)p(Q) - \frac{\partial p}{\partial n_Q}(Q)G(Q,M) \right) dS_v \tag{5.38}$$

Where *M* belongs to a point in the medium, n_Q is the normal to the surface taken at Q at the plate composed by surface area S_P and S_V point, *G(Q,M)* is the Green's function satisfying :

$$\nabla^2 G(Q,M) + k^2 G(Q,M) = \delta(x - x_0)\delta(y - y_0)\delta(z - z_0) \tag{5.39}$$

Where the δ is the Dirac delta distribution; *Q* is at *(x,y,z)* and *M* is at *(x_0,y_0,z_0)*. The expression for Green's function can be found using the bi-dimensional spatial Fourier transform for equation 5.39 as [124]

$$G(x, x_0, y, y_0, z, z_0) = \frac{j}{8\pi^2} \int_{-\infty}^{+\infty} \int_{-\infty}^{+\infty} \frac{e^{jk_x(x-x_0)} e^{jk_y(y-y_0)} e^{jk_z|z-z_0|}}{k_z} dk_x dk_y \tag{5.40}$$

Where $k_z = \sqrt{k^2 - {k_x}^2 - {k_y}^2}$

Where k_x, k_y are the real Fourier's variables in the bi-dimensional wave-number domain. To ensure that *G is finite*, when $|z - z_0|$ tends to infinity, the definition of k_z is taken as

$$k_z = \sqrt{k^2 - {k_x}^2 - {k_y}^2} \qquad \text{if} \quad k^2 \geq {k_x}^2 + {k_y}^2$$
$$k_z = \sqrt{{k_x}^2 + {k_y}^2 - k^2} \qquad \text{if} \quad k^2 \leq {k_x}^2 + {k_y}^2 \tag{5.41}$$

Equation 5.38 will be simplified if it is considered that there are no reflected waves from surface S_V. Thus, the acoustical source is only located on the plate, the surface integral then reduces to S_p with S_{p+} denoting the upper surface side of the plate and S_{p-} the lower side of the plate. Then equation 5.38 can be decomposed as

$$p(M) = \int_{S_{p+}} -\frac{\partial G}{\partial z_Q}(Q,M)p^+(Q)dS_{p+} + \int_{S_{p-}} \frac{\partial G}{\partial z_Q}(Q,M)p^-(Q)dS_{p-} + \int_{S_{p+}} \frac{\partial p^+}{\partial z_Q}(Q)G(Q,M)\,dS_{p+} - \int_{S_{p-}} \frac{\partial p^-}{\partial z_Q}(Q)G(Q,M)\,dS_{p-} \tag{5.42}$$

Where $M \in V^+$with V^+ is the half-space located "above" the plate. Since both the acoustic pressure gradient and both G(Q,M) are continuous functions on the plate midsurface, the simple layer contribution vanishes when S_{p+} and S_{p-} tend to S_p.

Thus equation 5.42 will simplify become

$$p(M) = \int_{S_p} \left(\frac{\partial p^+(Q)}{\partial z_Q} - \frac{\partial p^-(Q)}{\partial z_Q}\right)G(Q,M)\,dS_p \qquad Q \in S_p \tag{5.43}$$

Rearrange it again and considering equation 5.34 it will become

$$p(M) = -\int_{S_p} \Delta p\left(\frac{\partial G(Q,M)}{\partial z_Q}\right) dS_p \tag{5.44}$$

Rearrange again equation 5.33 for Δp and substitute into equation 5.44, it yields

$$p(M) = \int_{S_{p-}} [F(x,y) + m_p \omega^2 w(x,y) - D\nabla^4 w(x,y)](\frac{\partial G(Q,M)}{\partial z_Q})\, dS_p \qquad (5.45)$$

$Q \in S_p$ and $M \in V^+$

This integral representation in equation 5.45 depends on the two unknown fields, the acoustics field *p(M)* and the vibration of the plate *w(Q)*.
By using Euler's equation (equation 5.37) in the plane at z=0, it can be connected to become

$$\frac{\partial p}{\partial z}(M)\Big|_{z=0} = \rho_0\, \omega^2 \mathrm{w(M)} \qquad (5.46)$$

$$\int_{S_{p-}} [F(x,y) + m_p \omega^2 w(x,y) - D\nabla^4 w(x,y)](\frac{\partial^2 G(Q,M)}{\partial z_Q \partial z_M})\, dS_p = \rho_0\, \omega^2 \mathrm{w(M)} \qquad (5.47)$$

With $\frac{\partial}{\partial z_Q}$ and $\frac{\partial}{\partial z_M}$ are derivatives in the z direction at Q and M respectively.
Next, equation 5.47 can be solved to find the displacement w.

Integral Solution Using the Modal Basis

Now, the displacement, w expend in a series of plate modes:

$$w(x,y) = \sum_{m=1}^{\infty}\sum_{n=1}^{\infty} a_{mn}\varphi_{mn}(x,y) \qquad (5.48)$$

With a_{mn} is the modal displacement amplitude and φ_{mn} is the modal shape as equation 5.5 for simply supported plate. The same kind of expansion can be applied for excitation force,

$$F(x,y) = \sum_{m=1}^{\infty}\sum_{n=1}^{\infty} F_{mn}\varphi_{mn}(x,y) \qquad (5.49)$$

Where F_{mn} is the generalized force density for mode (*m*,*n*). Next, the mode shape φ_{mn} [124, 125] need to satisfy and become

$$D\nabla^4\varphi_{mn}(x,y) = m_p{\omega_{mn}}^2\varphi_{mn}(x,y) \tag{5.50}$$

With ω_{mn}as in equation 5.13. Later, when equation 5.48 and 5.49 substituting into 5.47 , it can transform into

$$\rho_0\,\omega^2\sum_{m=1}^{\infty}\sum_{n=1}^{\infty}a_{mn}\varphi_{mn}(x_0,y_0)$$

$$= \int_{S_p}\sum_{m=1}^{\infty}\sum_{n=1}^{\infty}\left[F_{mn} - m_p{\omega_{mn}}^2 a_{mn} + m_p\omega^2 a_{mn}\right]\varphi_{mn}(x,y)$$

$$\times\frac{\partial^2 G}{\partial z_Q\partial z_M}(\mathrm{x},\mathrm{x}_0,\mathrm{y},\mathrm{y}_0,z_Q = z_M = 0)d_x d_y$$

$$= \int_{S_p}\sum_{m=1}^{\infty}\sum_{n=1}^{\infty}\left[F_{mn} - m_p({\omega_{mn}}^2-\omega^2)a_{mn}\right]\varphi_{mn}(x,y) \tag{5.51}$$

$$\times\frac{\partial^2 G}{\partial z_Q\partial z_M}(\mathrm{x},\mathrm{x}_0,\mathrm{y},\mathrm{y}_0,z_Q = z_M = 0)d_x d_y$$

Next, to find the set of unknownsa_{mn}, the mode shape of φ_{pq} need to be included by multiplying both side with $\varphi_{pq}$and then integrating over the plate area. With consideration equation 5.12 and the orthogonality of the mode shape where $\int_{S_p} m_p\,\varphi_{mn}\varphi_{pq}dS_p = 0$ for$m \neq p$ and $n \neq q$, the equation 5.51 yields

$$\rho_0\,\omega^2 a_{pq}\frac{S_p}{4} = \sum_{m=1}^{\infty}\sum_{n=1}^{\infty}\left[F_{mn} - m_p({\omega_{mn}}^2-\omega^2)a_{mn}\right]C_{pqmn} \tag{5.52}$$

With $C_{pqmn}$is acoustical cross-modal coupling or coupling terms define as

$$C_{pqmn} = \int_{S_p} \int_{S_p} \varphi_{pq}(x_0, y_0) \frac{\partial^2 G}{\partial z_Q \partial z_M} (\mathrm{x}, \mathrm{x}_0, \mathrm{y}, \mathrm{y}_0, z_Q = z_M = 0) \varphi_{mn} d_x d_{x_0} d_y d_{y_0} \tag{5.53}$$

Then, substitute Green function equation, equation 5.40 into equation 5.53 and performing double integral over S_p,

$$C_{pqmn} = \frac{j}{8\pi^2} \int_{-\infty}^{\infty} \int_{-\infty}^{\infty} k_z \tilde{\varphi}^*{}_{pq}(k_x, k_y)\, \tilde{\varphi}_{mn}(k_x, k_y) d_{k_x} d_{k_y} \tag{5.54}$$

Where $\tilde{\varphi}_{mn}(k_x, k_y)$ denotes the Fourier transform of the modal shape ofφ_{mn} and $\tilde{\varphi}^*{}_{pq}$ is the conjugate transform which can be expressed by

$$\tilde{\varphi}_{mn}(k_x, k_y) = \int_0^a \int_0^b \varphi_{mn}(x, y) e^{-j(k_x x + k_y y)} d_x\, d_y \tag{5.55}$$

Evaluating equation 5.55 analytically for simply supported mode shape gives

$$\tilde{\varphi}_{mn}(k_x, k_y) = ab\pi^2 mn \left[\frac{(-1)^m e^{-jk_x a} - 1}{a^2 k^2{}_x - m^2\pi^2}\right] \left[\frac{(-1)^n e^{-jk_y b} - 1}{b^2 k^2{}_y - n^2\pi^2}\right] \tag{5.56}$$

And for conjugate form of the mode shape, the result is identical except the sign of the exponentials is changed from negative to positive

$$\tilde{\varphi}^*{}_{pq}\,(k_x, k_y) = ab\pi^2 pq \left[\frac{(-1)^p e^{jk_x a} - 1}{a^2 k^2{}_x - m^2\pi^2}\right] \left[\frac{(-1)^q e^{jk_y b} - 1}{b^2 k^2{}_y - q^2\pi^2}\right] \tag{5.57}$$

From equation 5.55, it can be found that the integrand with respect to $k_x$is an even function when the mode orders (p,m) are the same parity. Also with respect to k_y, it is an even function when the mode orders (q,n) are the same parity. Thus, it can be simplify to

$$C_{pqmn} = \frac{j}{2\pi^2}\int_0^\infty \int_0^\infty k_z \tilde{\varphi}^*{}_{pq}(k_x, k_y)\, \tilde{\varphi}_{mn}(k_x, k_y) d_{k_x} d_{k_y} \tag{5.58}$$

When p and m are the same parity and q and n is also the same parity. Other than that, $C_{pqmn} = 0$

Finally, substitute equation 5.56 and 5.57 inside 5.58, it is found

$$C_{pqmn} = C_{mnpq} = \frac{2j}{pqmn}\left(\frac{ab}{\pi^3}\right)^2 \int_0^\infty \int_0^\infty k_z \Upsilon \Omega \, d_{k_x} d_{k_y} \tag{5.59}$$

With

$$k_z = \sqrt{k^2 - {k_x}^2 - {k_y}^2}$$

$$\Upsilon = \frac{1 - (-1)^p cos\ k_x a}{\left(\left(\frac{k_x a}{p\pi}\right)^2 - 1\right)\left(\left(\frac{k_x a}{m\pi}\right)^2 - 1\right)}$$

$$\Omega = \frac{1 - (-1)^q cos\ k_y b}{\left(\left(\frac{k_y b}{q\pi}\right)^2 - 1\right)\left(\left(\frac{k_y b}{n\pi}\right)^2 - 1\right)}$$

Lauglanet [124] solved Equation 5.59 by using a numerical method in order to calculate these cross-coupling terms to overcome the difficult oscillating infinite integrals in the k_x, k_y domain.

After the C_{pqmn} terms numerically evaluated, the modal displacement amplitude a_{mn} can be found by solving the linear matrix equation (based from equation 5.52),

$$\left[C_{pqmn}\right]\{m_p({\omega_{mn}}^2-\omega^2)a_{mn}\}-\rho_0\,\omega^2\frac{S_p}{4}[I]\{a_{mn}\}=\left[C_{pqmn}\right]\{F_{mn}\} \quad (5.60)$$

With $\left[C_{pqmn}\right]$ is complex cross coupling matrix, $[I]$ is the identity matrix of size N x N, and {} indicates a column vector. Inverting $\left[C_{pqmn}\right]$ it will become

$$[I]\{m_p({\omega_{mn}}^2-\omega^2)a_{mn}\}-\rho_0\,\omega^2\frac{S_p}{4}\left[C_{pqmn}\right]^{-1}\{a_{mn}\}=\{F_{mn}\} \quad (5.61)$$

In order to simplify and avoid matrix inversion, an approximation can be applied in which the off diagonal terms in $\left[C_{pqmn}\right]$ are neglected,which only self-modal radiation contribution are taken into calculation. Laugnett [124] and Azma [125] shows that this has given good approximation in light fluid such as air when compared to the exact solution. Thus, this approach is consistent within this thesis scope since the study is limited only for radiation in the air. Since the diagonal terms can be calculated to a first approximation without long computation needed for the off-diagonal terms, and multiplying by $\frac{S_p}{4}$, Equation 5.61 will become

$$M_{pq}({\omega_{mn}}^2-\omega^2)a_{mn}-\rho_0\,\omega^2\left(\frac{S_p}{4}\right)^2\left(\frac{1}{C_{pqmn}}\right)a_{mn}=\widehat{F}_{pq} \quad (5.62)$$

With $M_{pq}=m_p(\frac{S_p}{4})$ and $\hat{F}_{pq}=F_{mn}(\frac{S_p}{4})$ are the generalized force of the mode. Next the complex cross coupling value C_{pqmn} and the modal displacement amplitude a_{mn} value will be used to calculate the radiated power. The total radiated power from both sides of the plate can be defined as

$$W = \frac{1}{2}\int_{S_{P+}} \Re\{p^{+}.\boldsymbol{v}^{*}\}\boldsymbol{n}\, dS_{P_{+}} + \frac{1}{2}\int_{S_{P-}} \Re\{p^{-}.\boldsymbol{v}^{*}\}\boldsymbol{n}\, dS_{P\_}$$

$$W = \frac{1}{2}\int_{S_{P+}} \Re\left\{\{p^{+} - p^{-}\}{v_{pq}}^{*}\right\} dS_{P} \qquad 5.63$$

Since **n** denotes a normal surface, v_{pq}denotes the velocity normal direction of the plate. The pressure difference $(\Delta p\,(x,y) = p^{+} - p^{-})$ can also be written as sum of plates mode shapes

$$\Delta p\,(x,y) = \sum_{m=1}^{\infty}\sum_{n=1}^{\infty} p_{mn}\varphi_{mn}(x,y) \qquad 5.64$$

The plate velocity can be written as

$${v_{pq}}^{*} = \frac{\partial w^{*}}{\partial t} = -j\omega \sum_{m=1}^{\infty}\sum_{n=1}^{\infty} {a^{*}}_{mn}\varphi_{mn}(x,y) \qquad 5.65$$

Next,when equation 5.65 and 5.64 put inside 5.63 and then integral on S_p is performed,it will become,

$$W = \frac{\omega}{2}\frac{S_p}{4} Re\left\{j\sum_{m=1}^{\infty}\sum_{n=1}^{\infty} {a^{*}}_{mn}p_{mn}\right\} \qquad 5.66$$

To obtain a convenient calculation, substitute equation 5.64 into equation of motion, equation 5.33 and then applying the orthogonality relationship between the modal shapes, it will yield

$$m\left({\omega^{2}}_{pq} - \omega^{2}\right)a_{pq} = F_{pq} + p_{pq} \qquad 5.67$$

Finally, to eliminate p_{pq} ,put equation 5.67 into equation 5.66, it will become

$$W = \frac{\omega S_p}{8} Re\left\{ j \sum_{m=1}^{\infty} \sum_{n=1}^{\infty} (m({\omega^2}_{mn} - \omega^2) a_{mn} - F_{mn}) {a^*}_{mn} \right\} \quad 5.68$$

The total radiation efficiency, σ,can be found from equation 5.1 which is

$$\sigma = \frac{W_{pq}}{\rho c S \langle \overline{{v_{pq}}^2} \rangle}$$

With $\langle \overline{{v_{pq}}^2} \rangle$ is the spatially averaged velocity squared and *S* is the area of the plate. $\langle \overline{{v_{pq}}^2} \rangle$ was given by

$$\langle \overline{{v_{pq}}^2} \rangle = \frac{1}{2ab} \int_0^a \int_0^b \langle {v_{pqq}}^2 \rangle \, dxdy \quad 5.69$$

Using the expansion in the series of plate modes for velocity, it will give simplification as equation 5.24 (for modal velocity amplitude) and now for modal displacement amplitude.

$$\langle \overline{{v_{pq}}^2} \rangle = \frac{\omega}{8} \sum_{p=1}^{\infty} \sum_{p=2}^{\infty} |a_{pq}|^2 \quad 5.70$$

To conclude, the radiation efficiency for the unbaffled plate takes into consideration the fluid loading on both sides compared to the baffled case which only considers one side of the plate. Thus, it need to be further divided by two to have an equivalence to the radiation efficiency of the baffled plate [124,125].

5.3.2 Radiation Efficiency Result for Unbaffled Plate Case.

A MATLAB program has been produced to evaluate the equation for radiation efficiency for the un-baffled plate case. The plate is a rectangular panel which has all the same dimensions and properties as the baffled plate describe in section 5.3.1. The calculations are carried out in the frequency range between 1 Hz until 10 kHz.

Three selective early modes, mode (1, 1), mode (2, 1) and mode (2, 2) were also shown as examples and later become a base for the parameter value that will be used in predicting the radiation power.

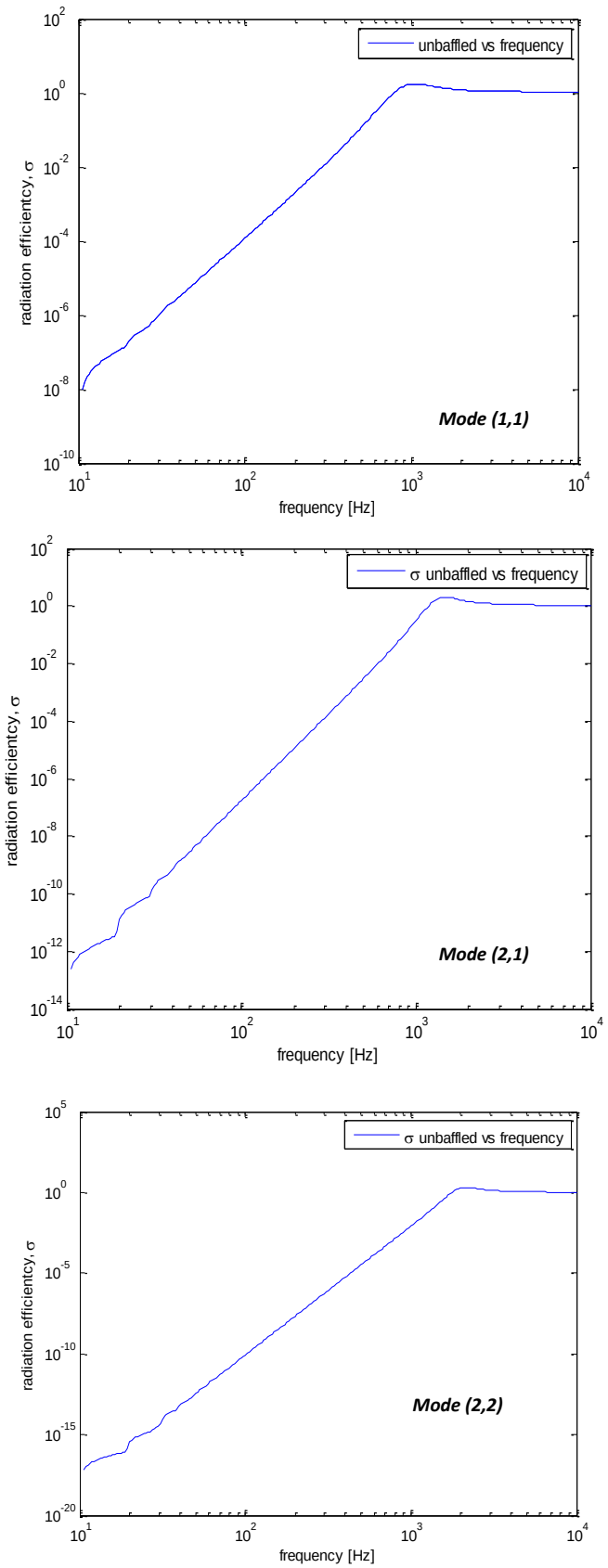

Figure 5.7: Radiation efficiency versus frequency for mode (1,1), (2,1) and (2,2)

Figure 5.7 shows the radiation efficiency for an unbaffled plate vibration with a mode shape corresponding to (1,1),(2,1) and (2,2). All the modes give a small value of radiation efficiency in the lower frequency and increase by frequency increment until they reach the maximum value around the calculated modal critical frequency. The graph also indicates that the higher modes will result in much lower radiation efficiency when compared to a lower mode at a lower frequency.

5.3.3 Comparison of the Radiation Efficiency for a Baffled and Un-baffled case for simply supported boundary condition.

Figure 5.8 shows the different radiation efficiency between baffled and un-baffle simply supported case for the lowest mode (1,1). Both of the results are plotted together for comparison so the differences are clearly identifyable. From the graph it can be seen that the radiation efficiency for the unbaffled plate is much reduced at low frequencies. In the Figure 5.8, the slope below the modal critical frequencies is almost 40 dB/decade for baffled compared to the unbaffled case with a 80dB/decade decrease.

Mode (1,1)

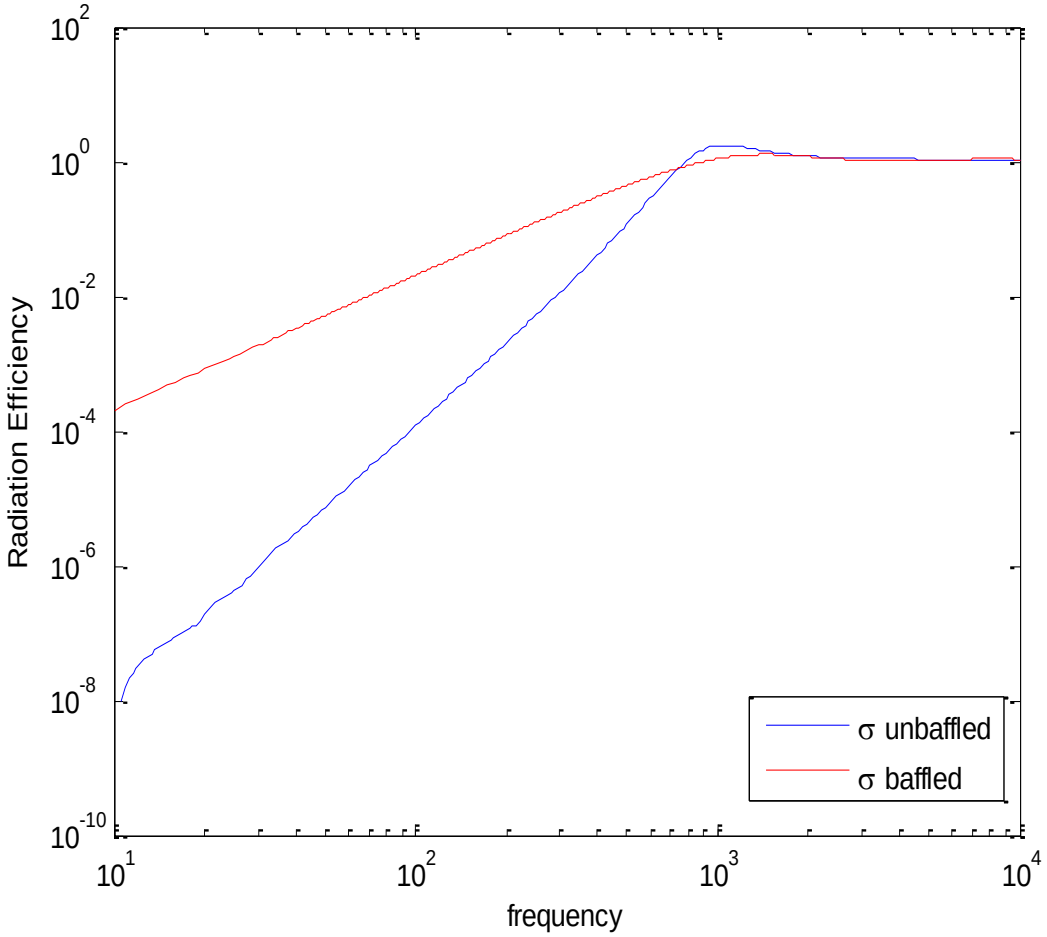

Figure 5.8: Radiation efficiency for the unbaffled case vs baffled case – 1.2mm (0.297x0.198x0.0012)m for mode (1,1)

Mode (2,1)

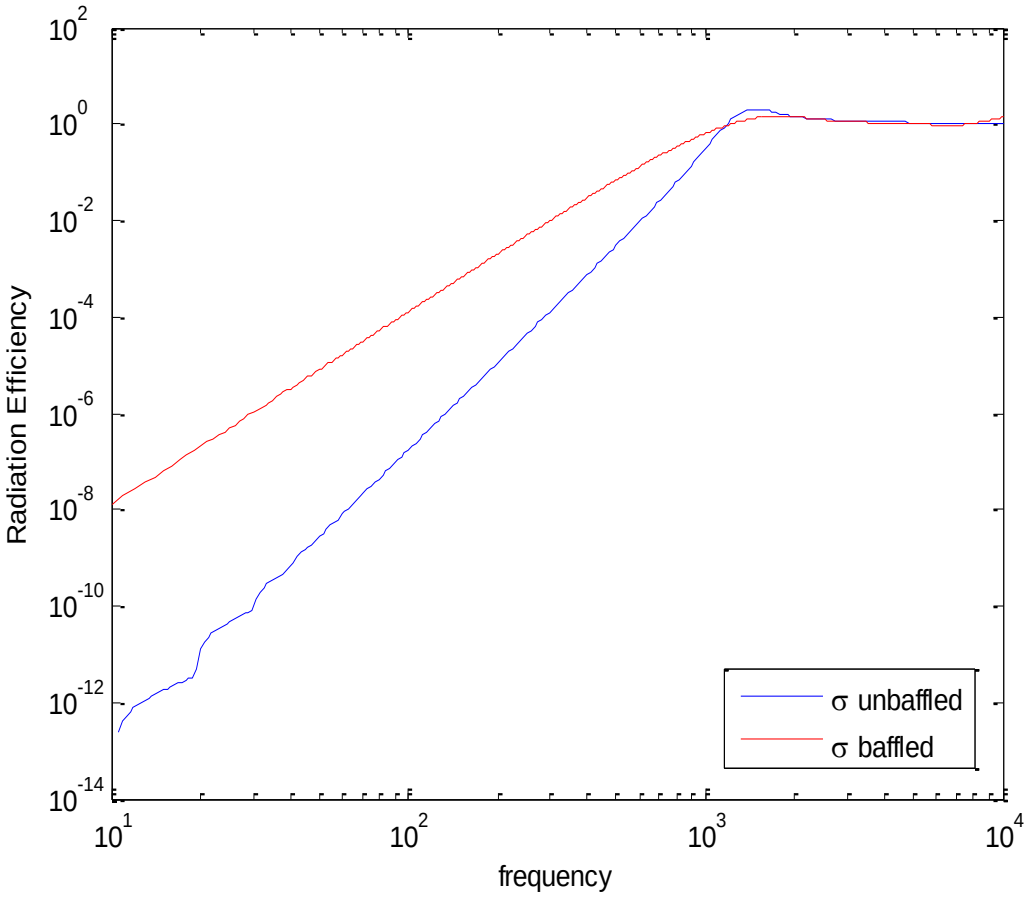

Figure 5.9: Radiation efficiency for the unbaffled case vs baffled case – 1.2mm (0.297x0.198x0.0012)m for mode (2,1)

Figure 5.9 shows different radiation efficiencies between the baffled and un-baffled simply supported case for the second lowest mode (2,1). When the mode is increased, the radiation efficiency for the mode still shows a large difference of value at lower frequency (below modal critical frequency) when compared between baffled and un-baffled cases. In the Figure 5.9, the slope below the modal critical frequencies is 80dB/decade for baffled compared to unbaffled which is around 120dB/decade.

Next, Figure 5.10 shows the different radiation efficiency between baffled and un-baffled simply supported case for mode (2,2). With the increment of mode, the radiation efficiency for lower frequency become smaller with the

slope below the modal critical frequencies is 130dB/decade for baffled compared to unbaffled which is around 170dB/decade.

Mode (2,2)

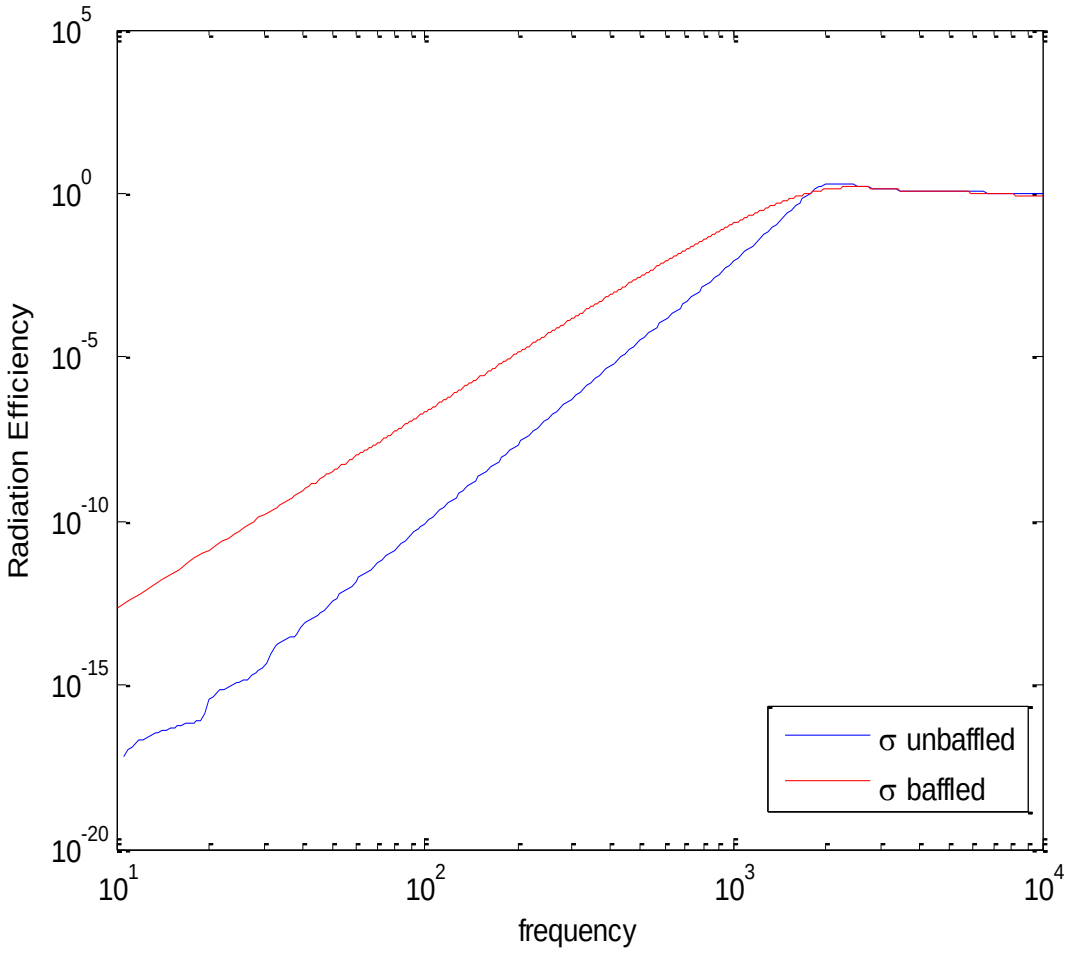

Figure 5.10: Radiation efficiency for the unbaffled case vs baffled case – 1.2mm (0.297x0.198x0.0012)m for mode (2,2)

5.3.4 Comparison of Radiation Efficiency of the Baffled Plate Between simply supported and clamped.

Since all the theoretical calculations are taken using the simply supported case for mathematic simplification, the differences in results need to be examined. According to Allen Berry [126], the radiation efficiency for all modes roughly show the same between the simply supported and clamped

plate (the difference being at most 4dB). Figure 5.11 illustrates the radiation efficiencies between a few modes under two different boundary conditions; clamped and simply supported plate.

The findings also agreed with the conclusion from Lomas et al. [127] which state there is only a small effect on the radiation efficiency because of elastic restraint against rotation at the edges. Futhermore, the radiation efficiency reaches its maximum value around modal critical frequencies as the same as the finding by Wallace [120].

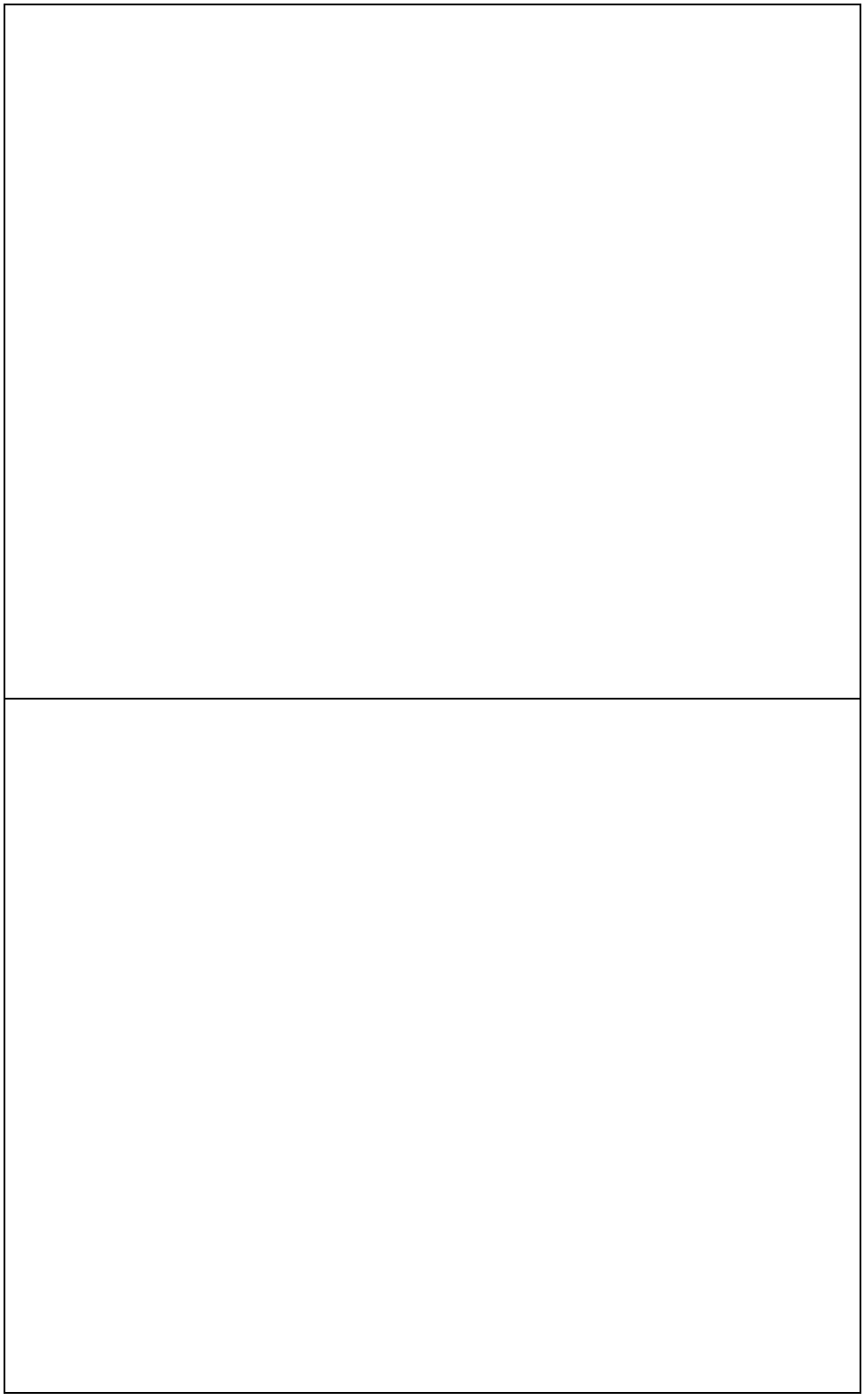

Figure 5.11: Image of radiation efficiency for the baffled plate between clamped (dashed curves) and simply supported (solid curves) for; (a) low modes (1,1),(2,1),(2,2) and (3,1); (b) high modes (5,5),(6,5) and (6,6). (Image taken from ref. [126])

5.4 Sound Power Prediction Using Digital Image Correlation Calculation

Digital Image Correlation is a non-destructive method for examining the surface displacement of materials. It uses a camera to track the movement of the surface and processes the data. Thus, the idea to predict the sound power is possible by calculating one of the main parameters that can be extracted from the DIC data. Figure 5.12 illustrates the flow chart on process to predict the sound power based from DIC experiment.

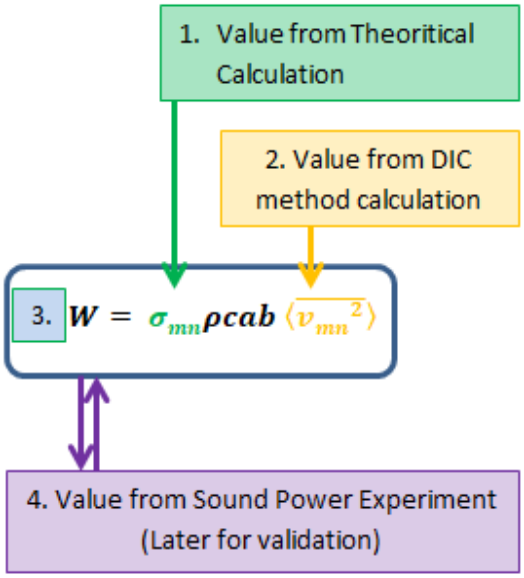

Figure 5.12: Flowchart on how process to predict sound power calculation based from DIC experiment.

In order to begin the sound power prediction, the general equation for radiation efficiency, equation 5.1 is being used. The value of radiation efficiency is taken from the theoretical value of an unbaffled plate of simply supported boundary conditions. Since the mathematical equation for the clamped plate is very complex, the value from the simply supported case will be used because as mentioned in section 5.3.4 before, the difference between both cases is quite small (the most 4dB) in lower frequency [126]. However, this difference will be taken into consideration as a potential source of error later in the sound power prediction.

Next, the parameter for spatial average mean square velocity is determined by using the DIC method calculation. DIC has the ability to track movement on every part of the surface depending on the resolution of the camera. Thus, the old difficulty in predicting this parameter that becomes one of the reasons why this mathematical formula did not produce a good result can be overcome and becomes one of the central novel contributions of the thesis. With the coverage of area of movement covered at maximum, the average value of the surface area can be calculated in the optimum condition.

Finally, the predicted sound power can be calculated by multiplying all the related parameters. In order to validate the method, sound power values of experimental measurements are also taken and then both of the predicted and experiment values are compared.

5.4.1 Method for calculating Spatial Average Mean Square Velocity from DIC

The 3D DIC has the ability to track movement in the outer plane compared to 2D only in-plane movement. Thus, the displacement of the Z-direction; an outer - plane can be tracked and utilised in this set of movements to become the velocity parameter.

DIC discretises the field of view (FOV) depending on the resolution of the camera. Next, to differentiate every discrete small box of areas, a unique identifier needs to be given; which is why speckle was added. After that, the translation movement of each pixel; based from camera resolution, is traced by comparing the previous image with each sequence of image respectively. Consequently, this set of sequence displacement image will display the movement of each small discrete box from image one until the end. Figure 5.13 illustrates graphically the displacement view on each small discrete box in the sequence of image number.

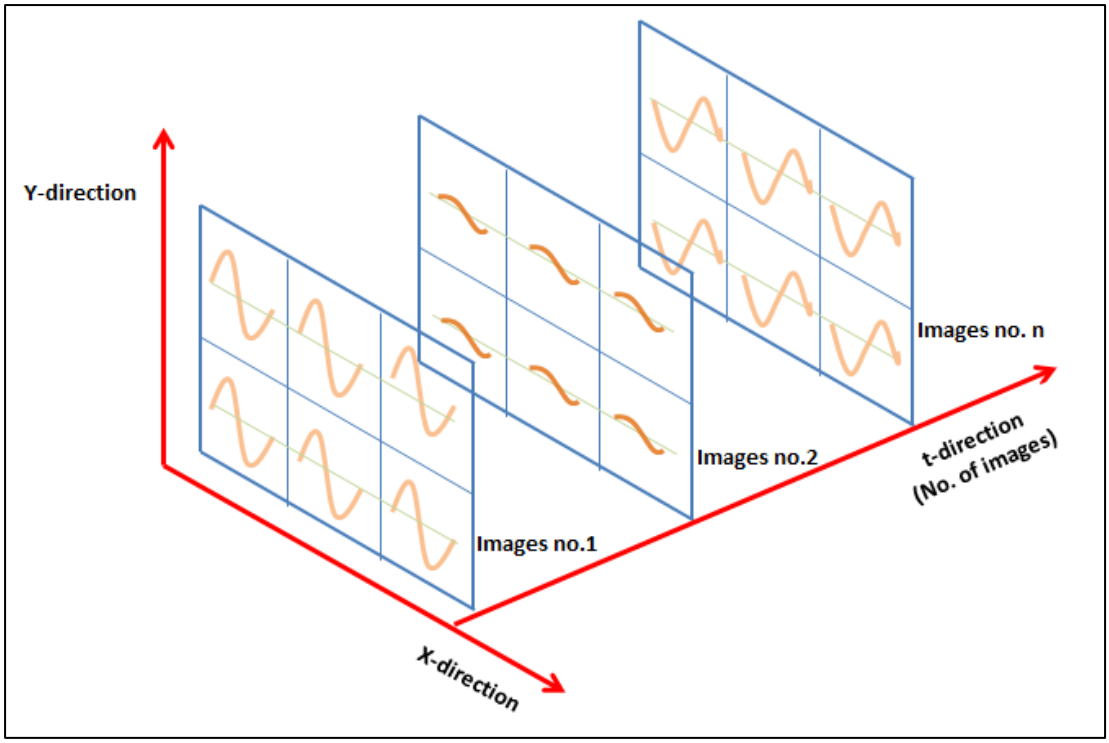

Figure 5.13: Graphical for the field of view plate (x, y) direction with the sequence number of images.

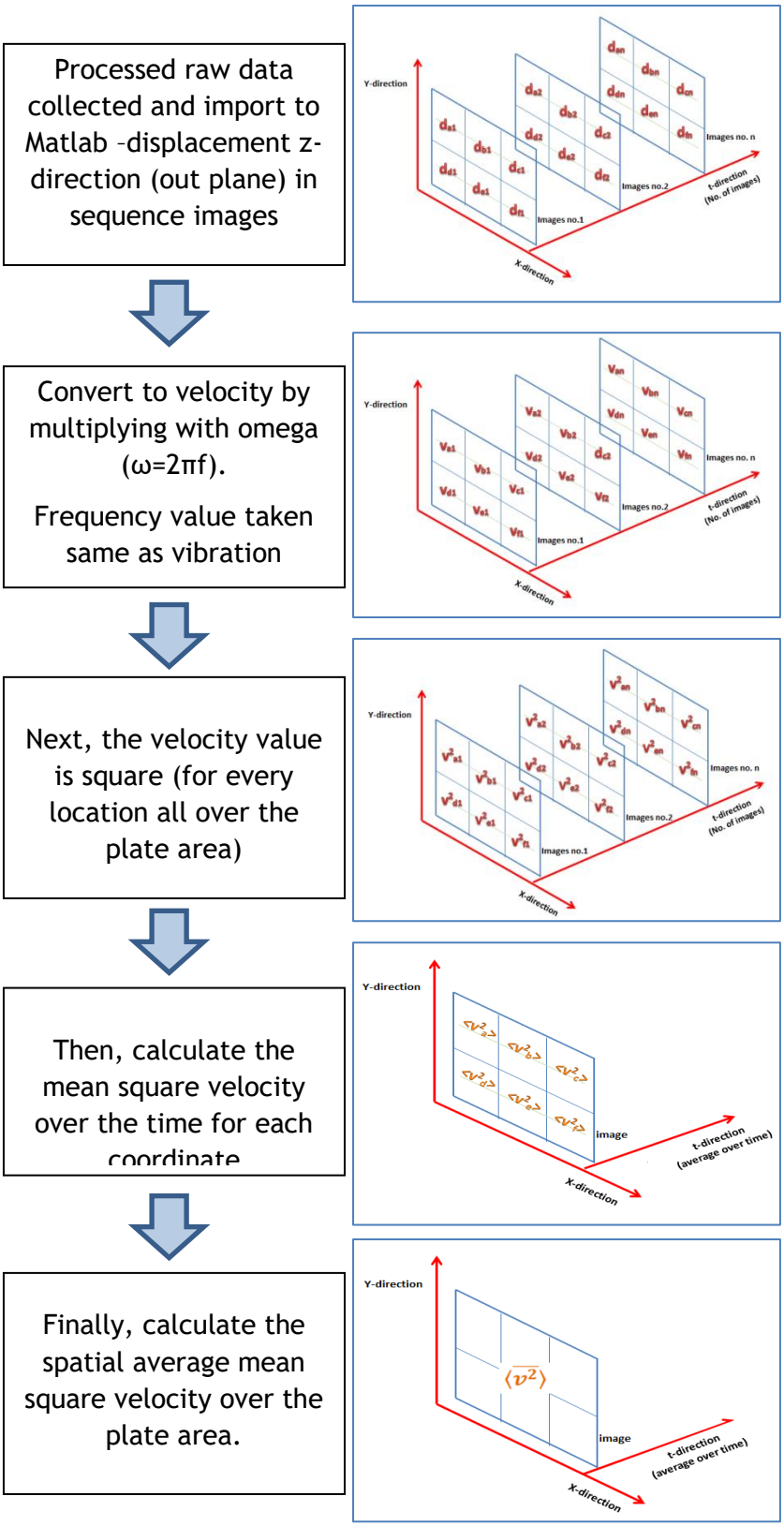

Figure 5.14: Flowchart on step to calculate spatial average mean square velocity based from DIC images.

The method for calculation begins with the displacement value collected for every image. If the complete measurement has 40 images of movement plus one static image as a baseline, all the raw displacement data for 41 images are extracted in Matlab software. Figure 5.14 illustrates the flowchart step to calculate the spatial average mean square velocity based from DIC images.

In Matlab, the data is sorted to determine the location and the sequence of its displacement at every point. Figure 5.15, shows the example image of plate at number 24; the displacement value of each location of plate in the colour scale of maximum and minimum displacement over all the plate. In the image, the centre of the plate experienced the maximum displacement in minus Z-direction outer plane.

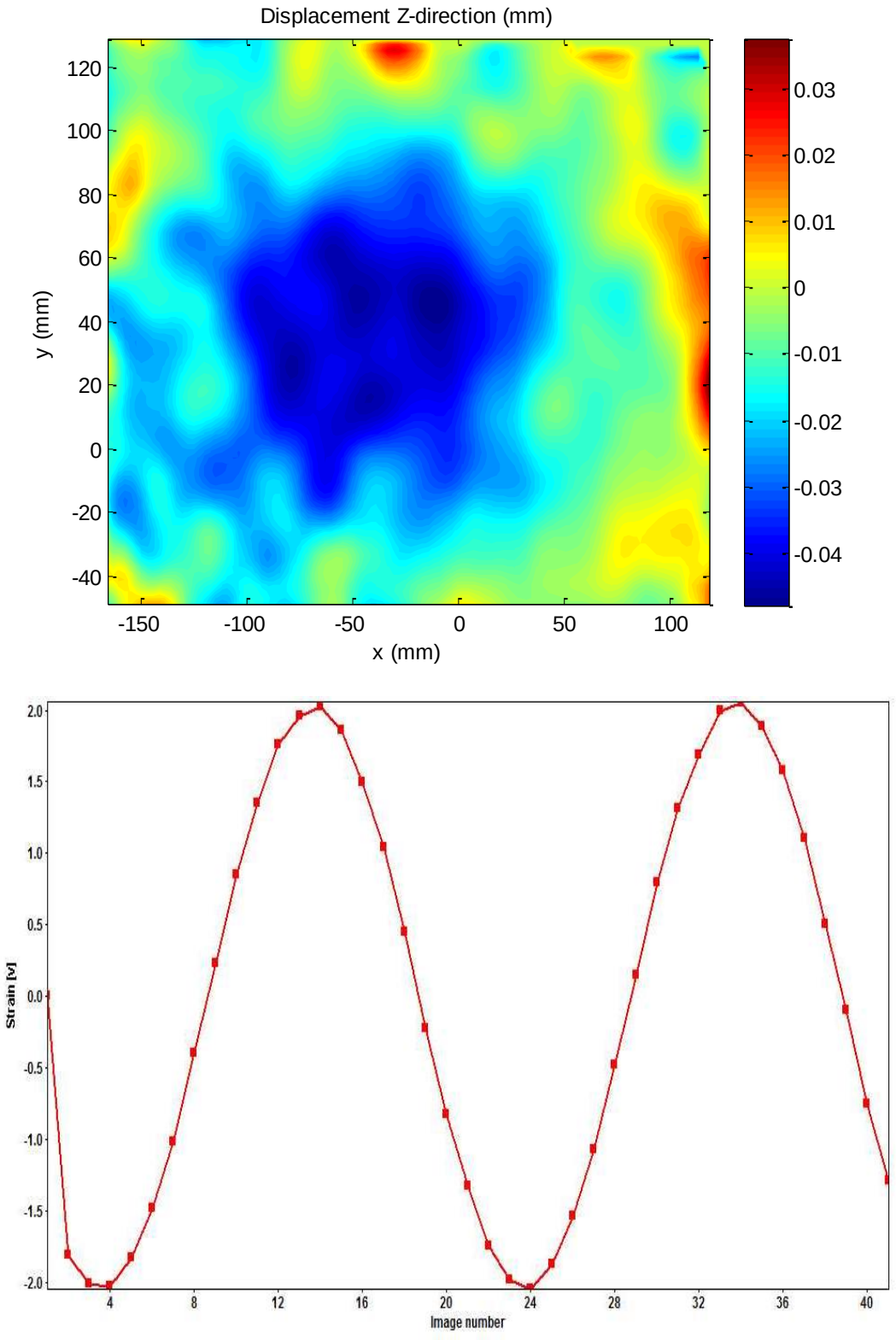

Figure 5.15: Displacement for the field of view, plot and image number versus voltage source

Next, all the displacement values for each location are converted to velocity by multiplying with omega, ω and the complex number i. Since the vibration source given to the plate by the shaker is a sinusoidal source with the value is respective to the plate resonance, the plate is expected to react in the sine wave according to the sinusoidal source. Thus, the omega from the vibration shaker is being used. After that, because of the sinusoidal model, the velocity needs to be squared in order to calculate the average and avoiding the zero average value. All the velocity for each location throughout the entire image needs to be squared. Subsequently, as shown in Equation 5.20, the average mean velocity square value is calculated by averaging the velocity square value for every location for each image.

Finally, this is only one image with various mean square velocity values for each location on the plate size. The spatial average value for that particular image is calculated by computing all the mean square velocity over the image of the plate area. Furthermore, for sinusoidal wave, the average will be zero, but the plate did not experience a perfect sinusoidal. For instance, for a perfect sinusoidal signal in a complete cycle with $y = A \sin \omega t$, the average value for y is zero. Nevertheless, for a signal with an offset of δ like $y = \delta + A \sin \omega t$, the average for y is not zero but δ. Moreover in theoretical calculation for radiation efficiency, the radiated power is divided by the spatial average mean square velocity that was developed based from a complete perfect sinusoidal wave. However, during experiment, the deformation captured by the camera does not show a good symmetrical shape of sinusoidal wave.

Thus, to increase accuracy, since the radiation efficiency referred is coming from theoretical value which is calculated from a perfect sinusoidal wave, the difference in deflection, δ, of real mode at the plate is considered. Therefore, the accurateness of the experiment can be increased by comparing the radiated sound power measured by experiment and divided by spatial averaged mean square velocity captured by experiment also. The Matlab for the modelling prediction can be found in the Appendix.

5.4.2 Selected Result of Spatial Average Mean Square Velocity from DIC

Mode (1,1) _200 Hz

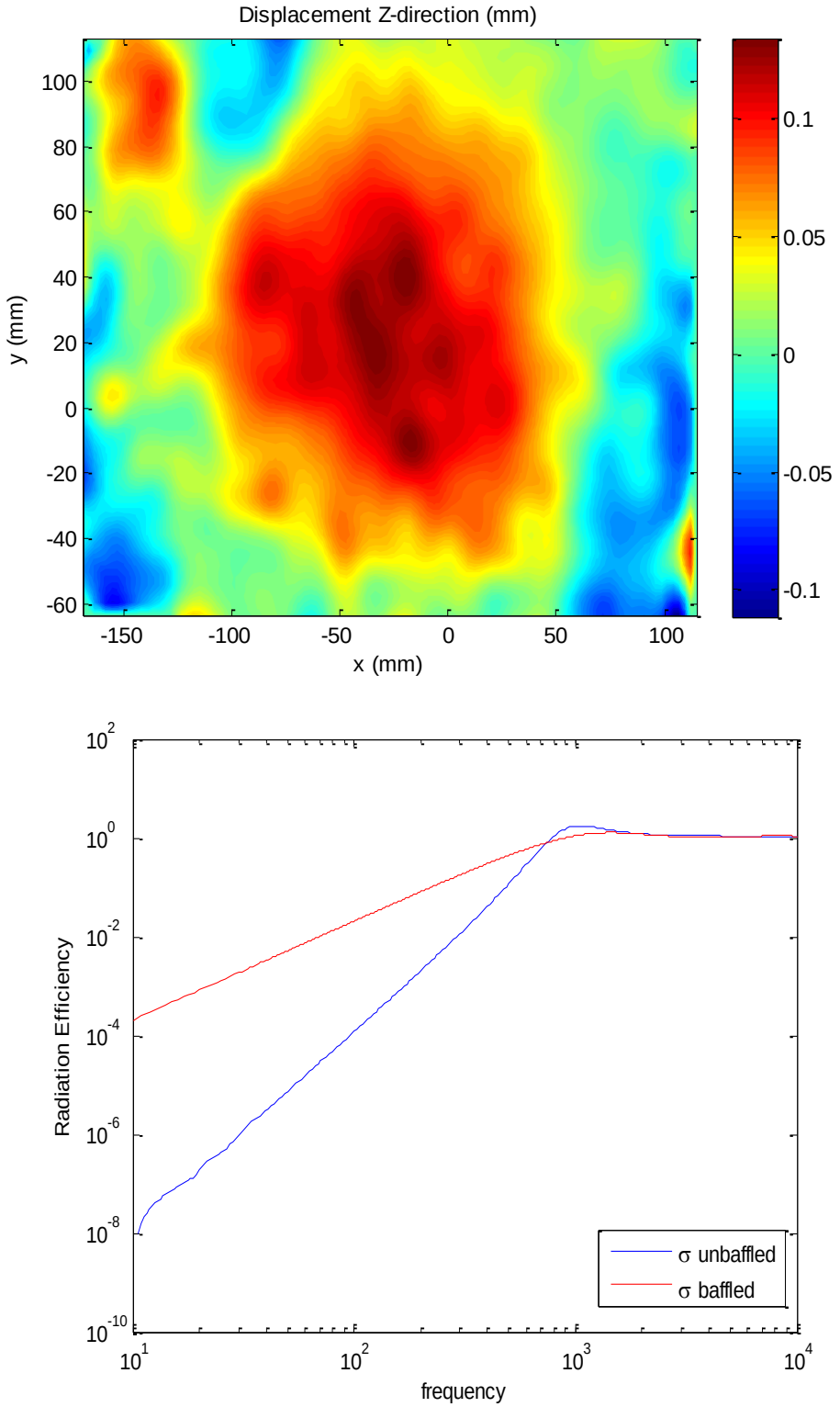

Figure 5.16: Displacement data from DIC and theoretical radiation efficiency graph for plate at mode (1,1)

Table 5.1 Data DIC measured, theoretical from graph and comparison of sound power between prediction and experiment for mode (1,1).

Mode	Radiation efficiency	δ^2	<Iv^2I>		Sound Power (SP)		Measured SP	
			Calculated	New calculated	Prediction (dB)	New prediction (dB)	(dB)	+ -
1,1	0.0020	0.00023	0.0028	0.0025	81.3	80.9	77.2	3.7

Figure 5.16 shows one of the images for the sequence of DIC data for mode (1,1). The data consists of displacement values for every point throughout the plate area. On the right hand side of the Figure 5.16, is the theoretical graph for ideal mode 1,1. From the modelling DIC calculation, the full results are shown in Table 5.1. The DIC calculation for average mean square velocity calculated provides a value of 0.0028 and when considering the existing of delta, δ, the value decrease to 0.0025.

Next, from the graph, the radiation efficiency for mode (1,1) at a frequency 195 Hz is 0.0020, the model predicts the sound power of 80.9 dB comparing to 81.3 dB before considering the delta. When validating it with the measured sound power, the difference between prediction and measurement is 3.7 dB. However, when considering the different boundary conditions between simply supported and clamped condition which as stated by Berry at section 5.3.4, the prediction can provide an accurate value between measured and prediction within the range of less than 4 dB.

Mode (2,1) _310Hz

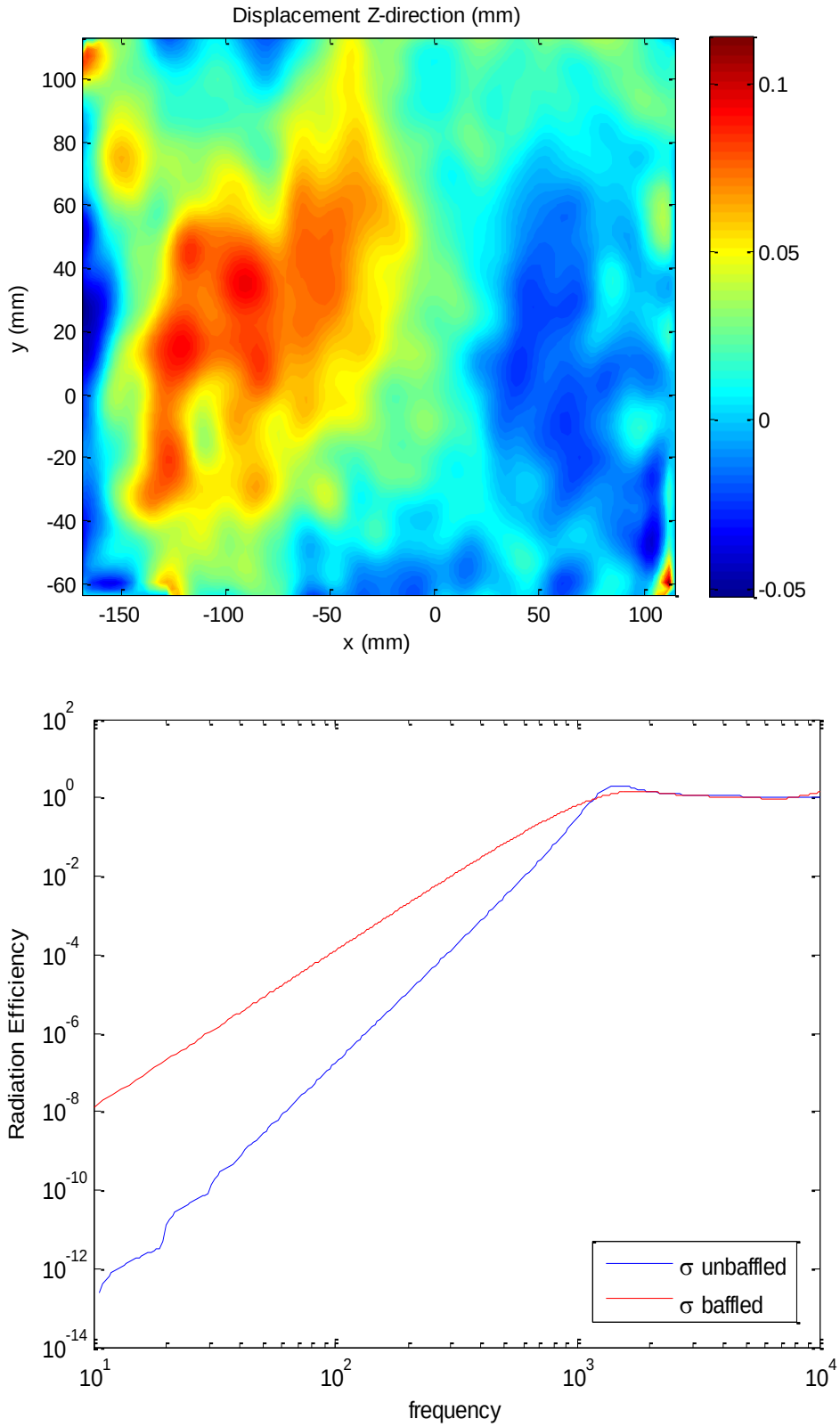

Figure 5.17: Displacement data from DIC and theoretical radiation efficiency graph for plate at mode (2,1)

Table 5.2 Data DIC measured, theoretical from graph and comparison of sound power between prediction and experiment for mode (2,1).

Mode	Radiation efficiency	δ^2	<Iv^2I>		Sound Power (SP)		Measured SP	
			Calculated	New calculated	Prediction (dB)	New prediction (dB)	(dB)	+ -
2,1	0.0015	0.00067	0.0042	0.0035	81.9	81.1	77.4	3.7

Figure 5.17 shows one of the images for the sequence of DIC data and the theoretical graph for radiation efficiency for mode 2,1. In the image, there can be seen a peak and bottom side by side to represent the 2,1 mode. Furthermore, Table 5.2 indicates the modelling result for predicting the sound power based from the DIC calculation. The difference between ideal shape and captured mode show a delta of 0.00067. The prediction sound power calculated at 81.1 dB and the measured noted at 77.4 dB. The different between both of the method is 3.7 dB. Yet, again if considered the boundary condition, the difference is less than 4 dB which indicate the prediction can provide a good accuracy result.

Mode (2,2)_590 Hz

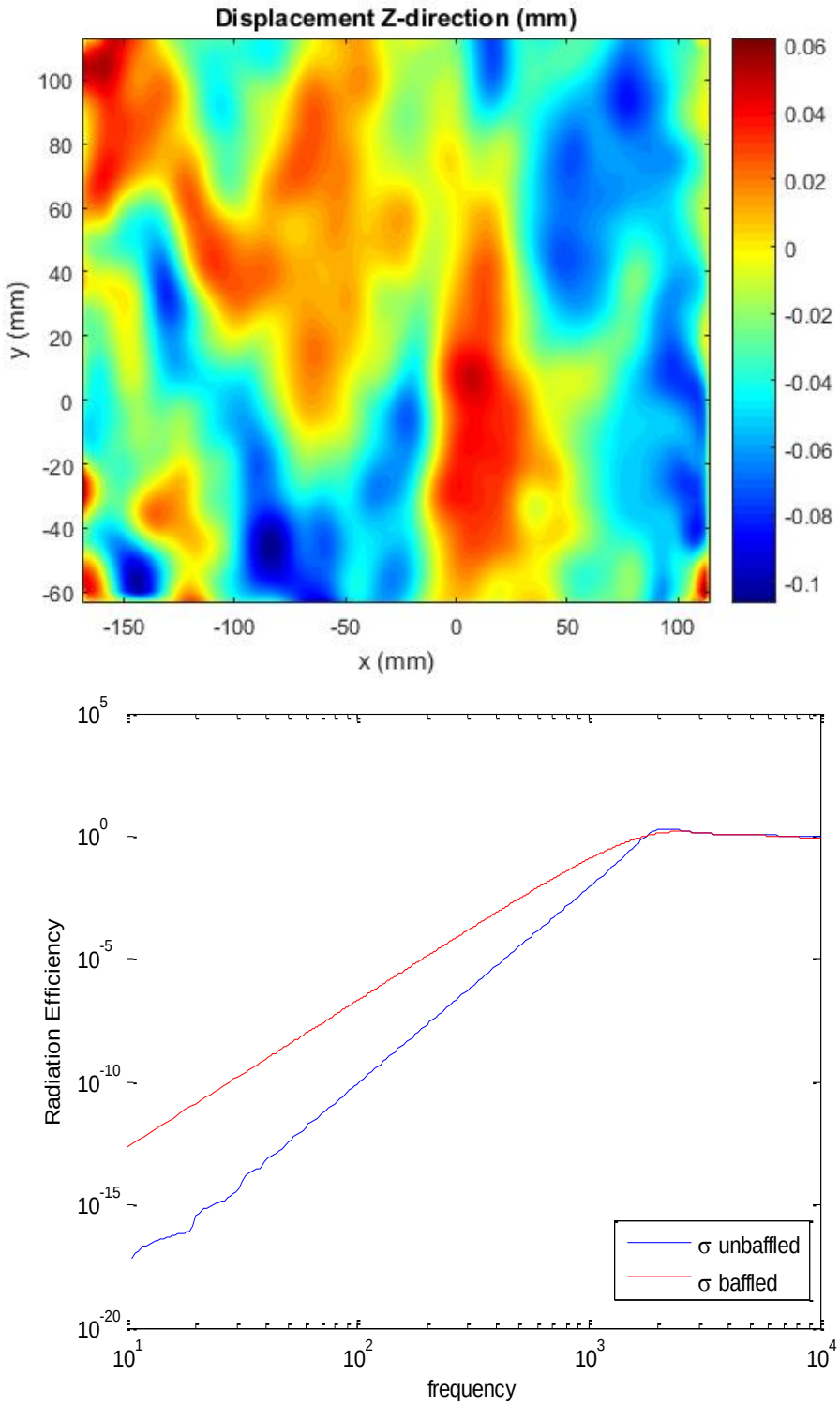

Figure 5.18: Displacement data from DIC and theoretical radiation efficiency graph for plate at mode (2,2)

Table 5.3 Data DIC measured, theoretical from graph and comparison of sound power between prediction and experiment for mode (2,2).

Mode	Radiation efficiency	δ^2	<Iv^2I>		Sound Power (SP)		Measured SP	
			Calculated	New calculated	Prediction (dB)	New prediction (dB)	(dB)	+ -
2,2	0.000132	0.000017	0.0169	0.0168	77.3	77.4	80.5	-3.1

Figure 5.18 shows one of the images for the sequence of DIC data and the theoretical graph for radiation efficiency for mode 2,2. Furthermore, Table 5.3 indicates the modelling result for predicting the sound power based from the DIC calculation. The difference between ideal shape and captured mode show a delta of 0.000017. The prediction sound power calculated at 77.4 dB and the measured noted at 80.5 dB. The different between both of the method is -3.1 dB. Yet, again if considered the boundary condition, the difference is less than 4 dB which indicate the prediction provide a good accuracy result.

5.5 Comparison of Results between DIC Prediction and Experimental

Based from the result, on overall, most of the predicted sound power shows the predict value within that acceptable range and according to theoretical finding. The radiation efficiency value is picked from the mathematic modelling for simply supported case for simplification and according to Allan Berry [126], as mentioned in section 5.3.4, there are not many differences in radiation efficiency value between clamped and simply supported with 4 dB difference.

Table 5.4: Comparison results of Sound Power (dB) between prediction (DIC) and experiment for different modes.

Mode	Frequency	Radiation efficiency	<Iv^2I>	Sound Power (dB)		Differences
				Prediction	Experiment	(dB)
1,1	200	0.0020	0.0025	80.9	77.2	3.7
2,1	310	0.0015	0.0035	81.8	77.4	3.7
1,2	480	0.00064	0.0064	80.0	80.0	0.0
2,2	590	0.00013	0.0168	77.4	80.5	-3.1
4,1	685	0.00095	0.0091	83.3	81.0	2.3
3,2	720	0.00025	0.0177	80.4	81.0	-0.6

For all the calculated mode, the prediction have a difference less than 4dB with maximum difference happen at mode 1,1 with 3.7 dB as shown in table 5.4 above. Although, for higher modes, (3, 2) and (4, 1), the difference is also small but the radiation efficiency value is solely taken from expected theory of mode shape. From observation, there are not significant outlines of the mode shape that captured by the DIC camera. The determination of the mode is figured out from the theoretical and finite element analysis. Yet, in the DIC stage, it is very hard to determine the correct mode unless with the help from finite element analysis.. This difficulty in determine the amplitude of vibration for higher frequency due to the noise in picture also mentioned by Nierecki as one of the challenge in DIC application [110].

5.6 Conclusion

Sound power prediction for individual modal modes can be predicted in a good accuracy with average mean square velocity calculated from the DIC measurement. Although the modelling uses the simplified theoretical radiation efficiency from mathematics, when considering the accepted range of dB values, the prediction sound power result in a good estimation.

This shows that, provided the natural frequency of an arbitrary panel can be identified by modal analysis and / or finite element methods, it is possible to predict the radiation efficiency and sound power of an arbitrary plate using the DIC equipment to obtain the surface velocity component. This can be done in a noisy environment meaning that special anechoic chambers for measurements aren't needed. On the next chapter, the thesis continue to discuss on some of the recommendation and future work with preliminary test show on the measurement of door car panel, suggestion for improving mathematic modelling and exploring more on the DIC image analysis stage.

CHAPTER 6
CONCLUSIONS AND FUTURE WORK

6.1 Introduction

This thesis contains a comprehensive design study on how to predict sound power for an automotive - type panel by modelling the output data from Digital Image Correlation equipment. Moreover, this study has used the low speed DIC camera in order to develop the model that can subsequently be used in order to predict the sound power parameter. The DIC shows some potential to calculate the mean square velocity value with relative accuracy, and thus generate a prediction for the sound power in an environment where sound measurements cannot be taken (or an anechoic environment is not available). Thus, the method indicates some prospects for application and data gathering in any type of boundary limitation.

The camera was able to provide a more accurate and spatially accurate averaging of the surface velocity than through the use of accelerometers and at a lower overall cost than either a Doppler laser vibrometer or a DIC with high speed cameras, providing that the possible measurement on a particular point location is in the field of camera view.

The research completed focuses on both the structural and acoustic characteristics of the test panel by comparing experimental measurements for both cases and validates the mode shape through Finite Element Analysis. Upon successfully predicting the sound power for the flat plate cases by using parameters from analytical calculations from theory, the method can be used as a reverse engineering step in predicting radiation efficiency. The radiation efficiency calculated will be more precise by considering the sound power and the mean square value captured by the DIC is the real experience by the sample.

6.2 General Conclusion

The thesis begins in chapter 1 by discussing the introduction of the research with the problem statement and the objective that are planned to be achieved. The novelty of the research in terms of techniques to predict sound power and alternative method to scanning lasser dopler are also discussed in this chapter. Next, in chapter 2, the thesis contains a through literature review, which shows the work previously undertaken and where gaps in knowledge are still to be resolved. A general overview on vehicle noise, current sound packages and established techniques that are widely practiced in noise and vibration refinement are provided. Also included are literatures on Digital Image Correlation and on past studies on how to predict the sound power based on a vibrating structure.

Furthermore, in chapter 3 and 4, the methodology and theory that are being used in this investigation, such as classical theoretical models, point mobility experiments, sound vibration and DIC setup best practice are reported respectively. The use of modal analysis methods in determining the resonance frequency of a structure have been planned as an experiment and validated through Finite Element Analysis. Experimental results for point mobility, mode shapes, natural frequencies and sound vibration are being reported. All have been re-calculated, compared theoretically, numerically and experimentally. Results from the DIC have also been produced to visualize the mode shape of an example automotive panel and to validate the modes that have been predicted by the FEM analysis.

Moreover, in chapter 5, the thesis also contains a discussion on how to predict the acoustic radiation characteristics of automotive panels, with a method to predict the sound power from DIC measurements and comparisons between predictions and experimental data. The method has been checked through the use of a baffled and unbaffled plate with various boundary conditions, as theoretical calculations are available on these cases. Data collected from the DIC equipment have been formulated to produce a desired parameter and with combinations of mathematical formula from the theoretical un-baffled case, an analysis of

predicting model calculations have been completed. The predicted sound power has then been evaluated with a sound power experimental value and comparisons between them were undertaken.

Finally, in this chapter on conclusion and future work, whilst the objective has been to obtain the sound power measurements using analytical expressions for the radiation efficiency, one application might be to reverse this process and use measurements of the sound power and surface velocity data from the DIC equipment to obtain actual values of the radiation efficiency.

6.3 Future Work

While conducting the research, there are few potential improvements that can considered as a future work to increase the quality of work and prediction. Some of the recommendations include:

1. **Improving Mathematic Modelling**. For running the prediction analysis, it is encouraged to use the more complicated mathematic to represent the correct boundary condition for plate sample. Currently, for simplification purpose, the boundary condition used for mathematic consideration is a simply supported case, while the more accurate mathematic according to the experiment is clamped boundary condition.

   Simply supported boundary condition will provide displacement, *w=0* and *d2w/dX2=0* while clamped boundary condition will provide *w=0* and *dw/dX=0* . Thus, for a mode shape equation, for simply supported, it can be represented for deflection on X(x) with sin (m-1) πx/a, but for clamped, it is becoming more complex as shown below (Classical FEM solution – equation 3.4a and 3.4b)

$$X(x) = \cos\gamma_1\left(\frac{x}{a}-\frac{1}{2}\right)+\frac{\sin\frac{\gamma_1}{2}}{\sinh\frac{\gamma_1}{2}}\cosh\gamma_1\left(\frac{x}{a}-\frac{1}{2}\right);(m=2,4,6\ldots.) \qquad (3.4a)$$

$$X(x) = \sin\ \gamma_2\left(\frac{x}{a}-\frac{1}{2}\right)+\frac{\sin\frac{\gamma_2}{2}}{\sinh\frac{\gamma_2}{2}}\sinh\gamma_2\left(\frac{x}{a}-\frac{1}{2}\right);(m=3,5,7\ldots.) \qquad (3.4b)$$

With the value of γ_1 and γ_2 are obtained as roots of

$$tan\ \frac{\gamma_1}{2}+\ tanh\ \frac{\gamma_1}{2}=0 \qquad \text{and} \qquad tan\ \frac{\gamma_2}{2}+\ tanh\ \frac{\gamma_2}{2}=0$$

This still avoids the real life variations in boundary condition at the plate edges, which have been shown important in this study.

2. **Representing a DIC image in the signal.** DIC experiment was run using a single sinusoidal vibration source with a sequence of capturing images was taken. The deformation in z-direction for the plate was exploited to represent the velocity and mean square velocity that were searched. However, the value calculated was only a single value at that particular sinusoidal frequency, thus it lacks more information on another frequency.

   Further study needs to be explored on representing the sequence of image captured in terms of possible signals to be representatives from time domain to frequency domain. If there is a possible method to represent it, more specific values such as mean square velocity can be represented in more broad frequency domain to provide a bigger set of useful data. There are few studies on representing an image as a signal representation by looking at the different intensity value of pixel to convert to signal and maybe the concept can be used for the DIC image (image analysis and pattern recognition).

3. **Measuring the average combination of mean square velocity for all the modes.** One of the issues to represent a good deformation of a plate is by exciting it to a particular resonance frequency and capturing the sequence of the displacement image. Therefore, this particular resonance frequency value can be used to calculate angular velocity and later for the mean square velocity value.

   However, for practical purpose, we are interested to measure the combination of all mean square velocity for every mode because most of the time, every sample received a random type of vibration and not only particular frequency only. Some researcher uses the combination of radiation efficiency by looking for every early mode shape before averaging it, but this step is long and took some effort to complete.

4. **Use the wide lens type for the DIC camera.** The cameras that have been used are a standard lens and are normally used for capturing images of samples in the small distance between them. However, because of the nature of the plate which is big compared to the normal working condition, it is required for a big gap in order to capture the full field of view to the plate, (around 1.8m-2m height). This height, and distance may be reducing the sharpness capability of the image to capture more sensitive movement of the plate vibration. Any small movement to the camera itself will interrupt the accuracy of the data. For instant, imaging when we are taking pictures with a high zooming setup. Any small shake movement in our hand will result big movement in the imaging picture.

   Therefore, it is suggested to use the camera together with the wide lens type to minimize the distance between the camera and the sample. With two additional types of this lens, the bigger size of the sample can be done and less number of experiments can be reduced in order to cover the wide area.

5. **Improving the experimental repeatability.** DIC measurement is involving measuring a very sensitive deflection on a surface of panel. A small movement in the reverberation floor may have an impact on the surface measurement. Thus to increase the repeatability of the data, every set of measurement is advised to be measured a few times in terms of their spatial average mean square velocity and the mean value for parameter it is calculated.

   Then, every spatial average mean square velocity value is computed in the sound power prediction model to predict the sound power level value. Finally, this set of prediction value will be validated with experiment. This will give a varying set of sound power level with standard deviations to calculate in order to make sure 95% of the value is within the limit of agreement.

6 **Reverse procedure to determine radiation efficiency.** Determine the radiation efficiency value; as recognised in the literature, it is difficult, especially in a theoretical calculation when involving different types of boundary condition and shape of the sample. Thus, this experimental method can be used in order to calculate the radiation efficiency. Originally, by calculating the spatial average mean square velocity and determining the radiation efficiency, predicted sound power value can be calculated. However, with these reverse procedure, sound power level is determined earlier together with the spatial average mean square velocity. Therefore, it is a more realistic approach since determining radiation efficiency through theoretical method is very difficult unless for simple geometry with simple boundary condition. The prediction calculates it before providing a quite good prediction when compared to the experiment in terms of sound power. Consequently, more complicated or realistic application can be run and analysed.

   For instance, an experiment to determine the structural and acoustic characteristic for a car door panel as shown in the figure 6.1 below. In this

case, two sections need to be divided because of the limitation area covered by the camera field of view due to the camera distance.

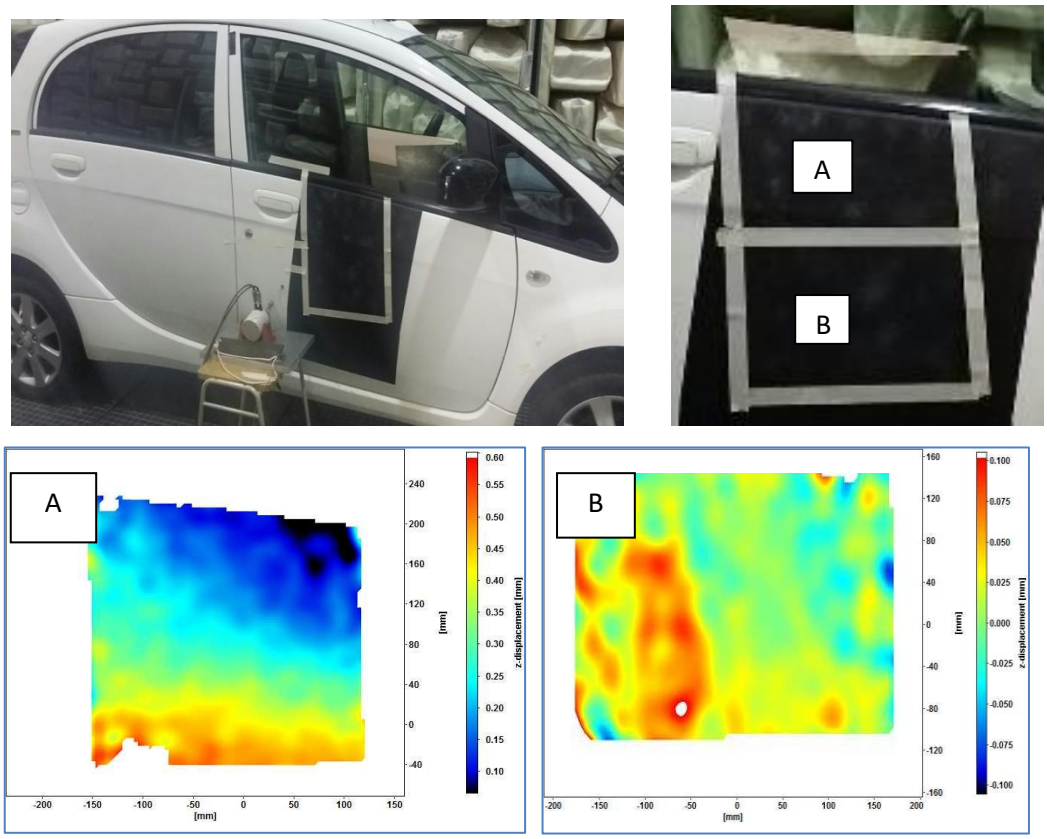

Figure 6.1: Preliminary study to determine sound radiation efficiency from door car panel.

The mean square velocity with respective to the mode and together the sound power measurement can be analysed to calculate the radiation efficiency. However, during this study, the car door panel characteristic did not provide further data to investigate because of the research time constraint; this therefore requires more exploring consideration into complex and complicated shape and the size of the sample.

To conclude, the three objectives planned in early chapter 1 successfully been achieved especially for objective number one and two. For chapter 3, the prediction well been proved for a few early mode shape when comparing to the measurement under consideration of mathematic simplification. Few other higher modes also provide a promising prediction when looking consideration of image captured by DIC for higher modes which have difficulty to specify a good illustrate

of mode shape images. Any future study can deliver few suggestions that can improve the quality and accuracy of the prediction model and contribute more on knowledge in determine the structural and acoustical characteristic for material. With a good prediction value, this sound power determination using the DIC hope can be develop more to help the development of ISO standard for measurement which currently there only a draft for development DD ISO/TS7849-1; 2009 [128].

References

[1] “Company History Benz Patent Motor Car: The first automobile (1885–1886)” [Online]. Available: https://www.daimler.com/company/tradition/company-history/1885-1886.html

[2] A. Yousefi and A. Hadi-Vencheh, “An integrated group decision making model and its evaluation by DEA for automobile industry,” *Expert Syst. Appl.*, 2010, vol. 37, no. 12, pp. 8543–8556.

[3] Hyo-Chan Kwon, Chang-Hee Cho, Cheong-Wu Nam, Soo-Won Chae, Seong-Yun Seo and Kwon-Hee Kim, "Reducing car audio button noise while maintaining tactile quality", *Advances in Mechanical Engineering*, 2018, Vol. 10(1) 1–10.

[4] Kumar, G., Walsh, S.J. and Krylov, V.V., *"Radiated sound power of automotive-type panels with dome-shaped indentations*." Proceedings of Forum Acusticum, alborg, Denmark, 2011, 26 June - 1 July, pp.2383-2386.

[5] Kumbhar Mansinh,, S., Miskin Atul,, R., and Chaudhari,, V., "Substructuring Approach in Interior Noise Refinement of a Vehicle," *SAE Technical Paper* 2009-26-0043, 2009, https://doi.org/10.4271/2009-26-0043.

[6] A. Rousounelos, S. J. Walsh, and V. V Krylov, “Weakly Radiating Structural Automotive-Type Panels Modes,” 2009, 16th *International Congress on Sound and Vibration*.

[7] Marburg, Steffen. Et., “Case Studies on Structural-acoutics optimization of a finite beam,” *Acta Acust.*, 2006, vol. 92, pp. 427–439.

[8] Shepherd, Micah & Hambric, Stephen. Structural-acoustic optimization of a pressurized, ribbed panel. *The Journal of the Acoustical Society of America*, 2014, 136. 2142-2142. 10.1121/1.4899728.

[9] Haosen Yang, Huirong Li, and Hui Zheng, A structural-acoustic optimization of two-dimensional sandwich plates with corrugated cores, J*ournal of Vibration and Control*, 2016, Vol 23, Issue 18, pp. 3007 - 3022

[10] Ehrhardt D.A., Yang S., Beberniss T.J., Allen M.S. Linear and Nonlinear Response of a Rectangular Plate Measured with Continuous-Scan Laser

Doppler Vibrometry and 3D-Digital Image Correlation. In: De Clerck J. (eds) Experimental Techniques, Rotating Machinery, and Acoustics, Volume 8. Conference Proceedings of the Society for Experimental Mechanics Series. Springer, Cham, 2015, https://doi.org/10.1007/978-3-319-15236-3_23

[11] P. Saha and S. Engineers, "Developing Vehicle Sound Packages", Sound & Vibration, 2011, pp. 10–13.

[12] A. Wolfindale, G. Dunne, S.J. Walsh, Vehicle noise primary attribute balance. *Applied Acoustics*, 2012, 73, 386-394

[13] A. Albarbar, F. Gu, a. D. Ball, and a. Starr, "Acoustic monitoring of engine fuel injection based on adaptive filtering techniques," *Appl. Acoust.*,2010, vol. 71, no. 12, pp. 1132–1141.

[14] Xu Wang, *Vehicle noise and vibration refinement*. Woodhead Publishing, 2010, eBook ISBN: 9781845698041.

[15] Matthew Harrison, *Vehicle Refinement : Controlling noise and vibration in road vehicles*. Elsevier Butterworth-Heinemann, 2004, eBook ISBN: 9780080474755.

[16] E. G. Giakoumis, A. M. Dimaratos, and C. D. Rakopoulos, "Experimental study of combustion noise radiation during transient turbocharged diesel engine operation," *Energy*, 2011, vol. 36, no. 8, pp. 4983–4995.

[17] M. E. Braun, S. J. Walsh, J. L. Horner, and R. Chuter, "Noise source characteristics in the ISO 362 vehicle pass-by noise test: Literature review," *Applied Acoustics*,2013, vol. 74, no. 11, pp. 1241–1265.

[18] L. Pruvost, Q. Leclère, and E. Parizet, "Diesel engine combustion and mechanical noise separation using an improved spectrofilter," *Mech. Syst. Signal Process.*,2009, vol. 23, no. 7, pp. 2072–2087.

[19] H. E. Head and J. D. Wake, "Noise of Diesel Engines Under Transient Conditions," *SAE Tech. Pap.*, 1980.

[20] BMW, Types of four-wheel drive (4WD) and all-wheel drive (AWD) systems, [online], https://x-engineer.org/automotive-engineering/drivetrain/awd-technologies/types-four-wheel-drive-4wd-all-wheel-drive-awd-systems.

[21] Wellmann, T., Govindswamy, K., Braun, E., and Wolff, K., "Aspects of

Driveline Integration for Optimized Vehicle NVH Characteristics," SAE Technical Paper, 2007, https://doi.org/10.4271/2007-01-2246.

[22] A. R. George and J. R. Callister, “Aerodynamic Noise of Ground Vehicles,” *SAE Tech. Pap.*, 1991, PA, SAE911027.

[23] Christian Peric, Simon Watkins, Elizabeth Lindqvist, Wind turbulence effects on aerodynamic noise with relevance to road vehicle interior noise, *Journal of Wind Engineering and Industrial Aerodynamics*, 1997, Pages 423-435,ISSN 0167-6105, https://doi.org/10.1016/S0167-6105(97)00174-8.

[24] J. S. C. Chuang, H. Lin, Y. Chen, and T. Su, “Study of Tire Noise for Vehicle Noise Control,” *SAE Tech. Pap.*, no. 2005–01–2415, 2005.

[25] A. Kuijpers, G. van Blokland, Tyre/road noise models in the last two decades: a critical evaluation, Proceedings of Inter-Noise 2001, The Hague, The Netherlands, 2001, pp. 2593–2598.

[26] Eisenblaetter, J., Walsh, S.J. and Krylov, V.V., Experimental investigations into the air pumping effect at the tyre/road interface. Proceedings of the Institute of Acoustics, 2006, 28 (1), pp.356-36.

[27] Keijiro Iwao, Ichiro Yamazaki, A study on the mechanism of tire/road noise, *JSAE Review*, 1996, Volume 17, Issue 2, Pages 139-144

[28] Joël Lelong, “Vehicle noise emission : evaluation of tyre/road- and motor-noise contributions.,” in *Inter Noise 99*, 1999, pp. 1–6.

[29] Matijević, D.V., Popović, V.M., Overview of Modern Contributions in Vehicle Noise and Vibration Refinement with Special Emphasis on Diagnostics, *FME Transactions*, 2017, Vol. 45, No. 3, pp. 448-458.

[30] M. Bettella, M. F. Harrison, and R. S. Sharp, “Investigation of Automotive Creep Groan Noise With a Distributed-Source Excitation Technique,” *J. Sound Vib.*, vol. 255, no. 3, pp. 531–547, Aug. 2002.

[31] K. B. Dunlap, M. A. Riehle, and R. E. Longhouse, “An Investigative Overview of Automotive Disc Brake Noise,” *SAE Tech. Pap.*, vol. 1999–01–01, no. 724, 1999.

[32] S. S. Gosavi, “Automotive Buzz, Squeak and Rattle (BSR) Detection and Prevention,” Jan. 2005.

[33] S.-H. Shin and C. Cheong, “Experimental characterization of instrument panel buzz, squeak, and rattle (BSR) in a vehicle,” *Appl. Acoust.*, vol. 71, no. 12, pp. 1162–1168, Dec. 2010.

[34] S. Kim, D. C. Park, S. Hong, P. Sellerbeck, A. Fiebig, M. Csakan, and C. Apelian, “Target Sound Development for Luxury Sedan based on Driving Experience and Preference Study,” May 2013.

[35] P. Susini, O. Houix, N. Misdariis, B. Smith, and S. Langlois, “Instruction’s effect on semantic scale ratings of interior car sounds,” *Appl. Acoust.*, vol. 70, no. 3, pp. 389–403, Mar. 2009.

[36] L. Zhang, “What Really Affect Customer Perception ? A Window Regulator Sound Quality Example,” no. 971909, pp. 5–8, 1997.

[37] D. Vige, “Vehicle interior noise refinement-cabin sound package design and development,” in *Vehicle noise and vibration refinement*, Matthew Harrison, Ed. Woodhead Publishing, 2010.

[38] Robert J. Bernhard, “Automobile, Bus and Truck interior noise and vibration prediction and control,” in *Handbook of Noise and Vibration Control*, M. J. Crocker, Ed. John Willey & Son Inc, 2007.

[39] J.-C. Bonnet, “Sound Quality Design, Trends in Vehicle Acoustics,” *Bussiness Forum China*, pp. 25–27, 2010.

[40] Y. S. Wang, G. Q. Shen, H. Guo, X. L. Tang, and T. Hamade, “Roughness modelling based on human auditory perception for sound quality evaluation of vehicle interior noise,” *J. Sound Vib.*, vol. 332, no. 16, pp. 3893–3904, Aug. 2013.

[41] Malcolm J. Crocker, Ed., *Handbook of Noise and Vibration*. John Willey & Son Inc.

[42] P. S. Wentzel, Richard E, “Empirically Predicting the Sound Transmission Loss of Double-Wall Sound Barrier Assemblies,” *SAE Tech. Pap.*, no. 951268, 2011.

[43] P. Saha, “The Thought Process for Developing Sound Package Treatments for a Vehicle,” SAE Technical Paper 2011-01-1679, 2011, https://doi.org/10.4271/2011-01-1679.

[44] J. Siavoshani, S. and Tudor, “PAPER SERIES ABA - New Generation of Vehicle Dashmats,” *SAE Tech. Pap.*, no. 2005–01–2277, 2005.

[45] A. Shivle, Smita and Murthy, “Improvement in Noise Transmission Across Firewall of a Passenger Car,” *SAE Tech. Pap.*, no. 2010–01–0751, 2010.

[46] J. R. Calllster and G. E. Freeman, “Aeroacoustic and Acoustic Testing of Automobile Side Windows,” *SAE Tech. Pap.*, no. 960902, 1996.

[47] Y. QIAN and J. Vanbuskirk, “Sound Absorption Composites and Their Use in Automotive Interior Sound Control,” *SAE Trans.*, p. P–291 (vol.1), 1995.

[48] R. Zulkifli, T.K. Thye, Mohd Faizal Bin Mat Tahir, Ahmad Rasdan Ismail, Mohd Jailani Mohd Nor, “Automotive Noise Insulation Composite Panel Using Natural Fibres with Different Perforation Areas,” *Appl. Mech. Mater.*, pp. 63–67, 2012.

[49] D. V. Parikh, Y. Chen, and L. Sun, “Reducing Automotive Interior Noise with Natural Fiber Nonwoven Floor Covering Systems,” *Text. Res. J.*, vol. 76, no. 11, pp. 813–820, Jan. 2006.

[50] A. Boyer, J. Casulli, J. Horak, H. Khan, and S. Charles, “ECoustics -- Vehicle Sound Package Inspired by Environmental Design,” *SAE Tech. Pap.*, no. 2007–01–2405, 2007.

[51] P. Chen and G. Ebbitt, “Noise Absorption of Automotive Seats,” in *SAE, International Congress and Exhibition*, 1998, no. 724.

[52] A. Mcmullan and M. Mealman, “An Investigation of Automotive Seat Fabric Sound Absorption,” SAE Tech. Pap., no. 2001–01–1454, 2001.

[53] S. K. Jain, M. P. Joshi, P. G. Shravage, P. S. Yadav, and N. V Karanth, “Evaluation of Acoustic Performance of Automotive Seats by Experimental and Simulation Techniques,” *SAE Tech. Pap.*, no. 2013–26–0105, 2013.

[54] R. Gayathri, R. Vasanthakumari, and C. Padmanabhan, “Sound absorption, Thermal and Mechanical behavior of Polyurethane foam modified with Nano silica, Nano clay and Crumb rubber fillers,” *Int. J. Sci. Eng. Res.*, vol. 4, no. 5, pp. 301–308, 2013.

[55] Y. Gur, S. Abhyankar, and D. Wagner, “Radiating Panel NVH Performance Evaluations for Vehicle Design,” SAE Technical Paper 2013-01-1991, 2013, https://doi.org/10.4271/2013-01-1991.

[56] L. F. P. Melzak M da Silva,Marcio Furukava,.Samir N. Y.,Roberto Jordan, Vanessa A. de Andrade Taufik El Helou, “Comparison of Asphalt Melt Sheets and LASD Materials for Structural Damping of a Passenger Vehicle,” *SAE Tech. Pap.*, no. 2008–36–0391, 2008.

[57] Teo L. Rocha and Marcio Calcada, “Control of Airborne Road Noise Using Sealers,” *SAE Tech. Pap.*, no. 2010–36–0458, 2010.

[58] K. M. Lilley and P. E. Weber, “Vehicle Acoustic Solutions,” *SAE Tech. Pap.*, no. 2003–01–1583, 2003.

[59] J. P. and J. V. B. H. Nelisse-, “Application of SEA in Vehicle Sound Package Design” Canadian. Acoustics, vol. 28, no. 3, pp. 168–169, 2000.

[60] Shorter, P., "Recent Advances in Automotive Interior Noise Prediction," SAE Technical Paper 2008-36-0592, 2008, https://doi.org/10.4271/2008-36-0592

[61] N. Atalla and F. Sgard, “Modeling of perforated plates and screens using rigid frame porous models,” *J. Sound Vib.*, vol. 303, no. 1–2, pp. 195–208, Jun. 2007.

[62] J. Simon and S. Charles, “On the Use of the Fast Multipole Method for Accurate Automotive Body Panel Acoustics Load Prediction,” no. 2007–01–2313, 2007.

[63] Charpentier, A., Sreedhar, P., and Fukui, K., "Using the Hybrid FE-SEA Method to Predict Structure-borne Noise Transmission in a Trimmed Automotive Vehicle," SAE Technical Paper 2007-01-2181, 2007, https://doi.org/10.4271/2007-01-2181.

[64] A. Charpentier, P. Sreedhar, and B. Gardner, “Use of a Hybrid FE-SEA Model of a Trimmed Vehicle to Improve the Design for Interior Noise,” SAE Tech. Pap., no. 2009–01–2199., 2009.

[65] Vaz, I., Washburn, K., and DeVries, L., "Improvement of an SEA Model of Cab Interior Sound Levels Through Use of a Hybrid FE/SEA Method," SAE Technical Paper 2011-01-1706, 2011, https://doi.org/10.4271/2011-01-1706.

[66] P. Shorter and S. Charles, “Using the Hybrid FE-SEA Method to Predict and Diagnose Component Transmission Loss,” SAE Tech. Pap., no. 2007–01–2172, 2007.

[67] C. Musser, “Sound Package Performance , Weight , and Cost Optimization Using SEA Analysis,” SAE Tech. Pap., no. 2003–01–1571, 2003.

[68] Musser, C., Manning, J., and Peng, G., "Prediction of Vehicle Interior Sound Pressure Distribution with SEA," SAE Technical Paper 2011-01-1705, 2011, https://doi.org/10.4271/2011-01-1705.

[69] J. Plunt, “Strategy for transfer path analysis (TPA) applied to vibro-acoustic systems at medium and high frequencies,” in Proc. ISMA 23, 16-18 September, Leuven, no. 1.

[70] Yao, L., & Zhang, G. (2012). Study on Automotive Interior Structure-Borne Sound Based on TPA. Proceedings of the FISITA 2012 World Automotive Congress, 457–469. doi:10.1007/978-3-642-33832-8_36

[71] J. Plunt and I. T. Ab, “Finding and Fixing Vehicle NVH Problems with Transfer Path Analysis,” Sound And Vibration, no. November, pp. 12–16, 2005.

[72] Shorter, P., Gardner, B., and Bremner, P., "A Review of Mid-Frequency Methods for Automotive Structure-Borne Noise," SAE Technical Paper 2003-01-1442, 2003, https://doi.org/10.4271/2003-01-1442.

[73] T. Courtois, C. Bertolini, and F. Porsche, “A Procedure for Efficient Trimmed Body FE Simulations , Based on a Transfer Admittance Model of the Sound Package,” SAE Tech. Pap., vol. 3, no. 2, pp. 1–13, 2010.

[74] V. B. Georgiev, V. V. Krylov, and R. E. T. B. Winward, “Simplified Modelling of Vehicle Interior Noise: Comparison of Analytical, Numerical and Experimental Approaches,” Low Freq. Noise Vib. Act. Control, vol. 25, no. 2, pp. 69–92, Jun. 2006.

[75] S.-H. Oh, H. Kim, and Y. Park, “Active control of road booming noise in automotive interiors,” J. Acoust. Soc. Am., vol. 111, no. 1, p. 180, 2002.

[76] Lee, Y. and Nasiri, A., "Real Time Active Noise Control of Engine Booming in Passenger Vehicles," SAE Technical Paper 2007-01-0411, 2007, https://doi.org/10.4271/2007-01-0411.

[77] R. Schirmacher, R. Lippold, F. Steinbach, and F. Walter, “Practical aspects of implementing car interior active noise control systems,” J. Acoust. Soc. Am., vol. 123, no. 5, p. 3532, 2008.

[78] E. Bianchini, “Active vibration control of automotive like panels Active vibration control of automotive like panels,” SAE Tech. Pap., no. 2008–36–0576, 2008.

[79] Togashi PhD, C., Nakano PhD, M., and Nagai PhD, M., "A Study on Active Hydraulic Engine Mount to Reduce Interior Car Noise and Vibration over Wide Frequency Band," SAE Technical Paper 2011-01-1636, 2011, https://doi.org/10.4271/2011-01-1636.

[80] S. Tewes, “Active Trim Panel Attachments for Control of Sound Transmission through Aircraft Structures,” PhD Thesis, Technische Universit at Munchen, 2006.

[81] I. Kim and Y.-S. Kim, “Active vibration control of trim panel using a hybrid controller to regulate sound transmission,” Int. J. Precis. Eng. Manuf., vol. 10, no. 1, pp. 41–47, Jul. 2009.

[82] McCormick, N., & Lord, J. (2010). Digital Image Correlation. Materials Today, 13(12), 52–54. doi:10.1016/s1369-7021(10)70235-2

[83] H. W. S. Michael A. Sutton, Jean-Jose Orteu, Image Correlation for Shape, Motion and Deformation Measurements. Springer Science+Business Media, LLC 2009, 2009.

[84] T. Siebert, R. Wood, and K. Splitthof, “High speed image correlation for vibration analysis,” J. Phys. Conf. Ser., vol. 181, p. 012064, 2009.

[85] T. Siebert, W. Z. Wang, J. E. Mottershead, and A. Pipino, “Application of High Speed Image Correlation for Measurement of Mode Shapes of a Car Bonnet,” Appl. Mech. Mater., vol. 70, pp. 45–50, 2011.

[86] M. N. Helfrick, C. Niezrecki, P. Avitabile, and T. Schmidt, “3D digital image correlation methods for full-field vibration measurement,” Mech. Syst. Signal Process., vol. 25, no. 3, pp. 917–927, 2011.

[87] Theunis R. Botha, Digital Image Correlation : Application in Vehicle Dynamics. PhD Thesis, University of Pretoria, 2015.

[88] A.E.H. Love, “Mathematical Theory of Elasticity,” Cambridge Univeristy Press, 1927.

[89] G. B. Warburton, “The vibration of rectangular plates,” Arch. Proc. Inst. Mech. Eng. 1847-1982 (vols 1-196), vol. 168, no. 1954, pp. 371–384, 2006.

[90] A. W. Leissa, “Vibration of Plates,” Scientific and Technical Information Division, NASA, 1969.

[91] R. D. Blevins, Formulas for Natural Frequency and Mode Shape. Krieger Publishing Company, 2001.

[92] G. Kumar, “Structural-Acoustic Properties of Automotive Panels with Shell Elements,” Loughborough University, 2014.

[93] Erik Cietus Petersen, Application notes - An Overview of Standards for Sound Power Determination (bo0416).

[94] BS EN ISO 3745. Acoustics - determination of sound power levels of noise sources using sound pressure. Precision methods for anechoic and semi-anechoic rooms. CEN, 2003.

[95] BS EN ISO 3745. Acoustics - determination of sound power levels of noise sources using sound pressure. Precision methods for reverberation rooms. CEN, 1994.

[96] BS EN ISO 9614. Acoustics - determination of sound power levels of noise sources using sound intensity - part 1 measurement at discrete points. CEN, 1993.

[97] BS EN ISO 9614: 2002 . Acoustics - determination of sound power levels of noise sources using sound intensity - part 2 measurement by scanning. CEN, 1997.

[98] Vinh Trinh, Measure,ment of Sound Intensity and Sound Power, MRL Technical Report MRL-TR-93-32, http://www.dtic.mil/dtic/tr/fulltext/u2/a279246.pdf.

[99] F.J. Fahy. Sound Intensity. Elsevier Applied Science, London, 1989.

[100] Bruel & Kjaer. Product Data: Sound Intensity Probe Kit Type 3599 (bp1880). https://www.bksv.com/-/media/literature/Product-Data/bp1880.ashx.

[101] Bruel & Kjaer Sound Intensity. https://www.bksv.com/media/doc/br0476.pdf.

[102] D.A.Ehrhardt,etal.,Full-field linear and nonlinear measurements using Continuous-Scan Laser Doppler Vibrometry and high speed Three-Dimensional Digital Image Correlation, Mech.Syst.SignalProcess.(2016), http://dx.doi.org/10.1016/j.ymssp.2015.12.003i

[103] STANBRIDGE, A. B., & EWINS, D. J. (1999). MODAL TESTING USING A SCANNING LASER DOPPLER VIBROMETER. Mechanical Systems and Signal Processing, 13(2), 255–270. doi:10.1006/mssp.1998.1209

[104] Stanbridge, A. B., Ewins, D. J., & Khan, A. Z. (2000). Modal Testing Using Impact Excitation and a Scanning LDV. Shock and Vibration, 7(2), 91–100. doi:10.1155/2000/527389

[105] Yang, S., Sracic, M. W., & Allen, M. S. (2012). Two Algorithms for Mass Normalizing Mode Shapes From Impact Excited Continuous-Scan Laser Doppler Vibrometry. Journal of Vibration and Acoustics, 134(2), 021004. doi:10.1115/1.4005020

[106] hen, Da-Ming & Zhu, W. (2019). Rapid and Dense 3D Vibration Measurement by Three Continuously Scanning Laser Doppler Vibrometers. 19-29. 10.1007/978-3-319-74693-7_3.

[107] P.L. Reu, et al., Comparison of DIC and LDV for practical vibration and modal measurements, Mech. Syst. Signal Process. (2016), http://dx.doi.org/10.1016/j.ymssp.2016.02.006i

[108] D.A.Ehrhardt, S.Yang, T.J.Beberniss, M.S.Allen, Mode shape comparison using continuous-scan laser Doppler vibrometry and high speed 3D digital image correlation, In: Proceedings of the International Modal Analysis Conference XXXII, Orlando, FL, 2014.

[109] Helfrick, M. N., Niezrecki, C., Avitabile, P., & Schmidt, T. (2011). 3D digital image correlation methods for full-field vibration measurement. Mechanical Systems and Signal Processing, 25(3), 917–927. doi:10.1016/j.ymssp.2010.08.013

[110] C.Niezrecki, P.Avitabile, C.Warren, P.Pingle, M.Helfrick, A review of digital image correlation applied to structura dynamics, in: AIP Conference Proceedings, vol.1253(1), 2010,pp.219–232.

[111] T.J. Beberniss, D.A. Ehrhardt, High-speed 3D digital image correlation vibration measurement: Recent advancements and noted limitations, Mech. Syst. Signal Process. (2016), http://dx.doi.org/10.1016/j.ymssp.2016.04.014

[112] Yu, L., & Pan, B. (2017). Single-camera high-speed stereo-digital image correlation for full-field vibration measurement. Mechanical Systems and Signal Processing, 94, 374–383. doi:10.1016/j.ymssp.2017.03.008.

[113] López-Alba, E., Felipe-Sesé, L., Schmeer, S., & Díaz, F. A. (2016). Optical low-cost and portable arrangement for full field 3D displacement measurement using a single camera. Measurement Science and Technology, 27(11), 115901. doi:10.1088/0957-0233/27/11/115901.

[114] Warburton, J.R., Lu, G., Buss, T.M. et al. Exp Mech (2016) 56: 1219. https://doi.org/10.1007/s11340-016-0162-1

[115] Mat Tahir, M.F., Walsh, S.J. and O'Boy, D.J., 2015. Evaluation of the digital image correlation method for the measurement of vibration mode shapes.

Inter-Noise and Noise-Con Congress and Conference Proceedings, 9-12th Aug., 2015, pp. 1986-1995.

[116] Fruehmann, R. K., Dulieu-Barton, J. M., Quinn, S., & Tyler, J. P. (2015). The use of a lock-in amplifier to apply digital image correlation to cyclically loaded components. Optics and Lasers in Engineering, 68, 149–159. doi:10.1016/j.optlaseng.2014.12.021.

[117] VIC 3D v7- Testing Guide (user manual).

[118] Lavision, "DaVis_D81- User manual.

[119] F. J. Fahy and P. Gardonio. Sound and Structural Vibration: Radiation, Transmission and Response. Academic Press, London, 2nd edition, 2006.

[120] C. E.Wallace. Radiation resistance of a rectangular panel. Journal of the Acoustical Society of America, 51:946–952, 1972.

[121] L. Cremer, M. Heckl, and B. A. T. Petersson. Structure-borne sound. Springer, Berlin, 3rd edition, 2005.

[122] Xie, G & Thompson, David & Jones, C.J.C. The radiation efficiency of baffled plates and strips. Journal of Sound and Vibration.2005. 280. 181-209. 10.1016/j.jsv.2003.12.025.

[123] G. Xie, D.J. Thompson and C.J.C. Jones, Investigation of the Radiation Efficiency of Strips, ISVR Technical Memorandum No 895, 2002, http://resource.isvr.soton.ac.uk/staff/pubs/PubPDFs/Pub1588.pdf

[124] B. laulagnet, Sound Radiation by simply supported unbaffled plate, 1998. The Journal of the Acoustical Society of America 103, 2451.

[125] Azma Putra. Sound Radiation from perforated plates, University of Southampton, Faculty of Engineering, Science and Mathematics, Institute of Sound and Vibration Research, Phd Thesis (2008).

[126] A. Berry, J. L. Guyader, and J. Nicolas, A general formulation for the sound radiation from rectangular, baffled plates with arbitrary boundary conditions, 1990. The Journal of the Acoustical Society of America 88, 2792–2802.

[127] N.S. Lomas and S.I. Hyek, Vibration and acoustic radiation of elastically supported rectangular plates, 1977, Journal Sound Vibration 52, 1-25

[128] ISO/TS 7849-1:2009, Acoustics — Determination of airborne sound power levels emitted by machinery using vibration measurement — Part 1: Survey method using a fixed radiation factor

APPENDIX

DIC complete image for mode shape (1,1)

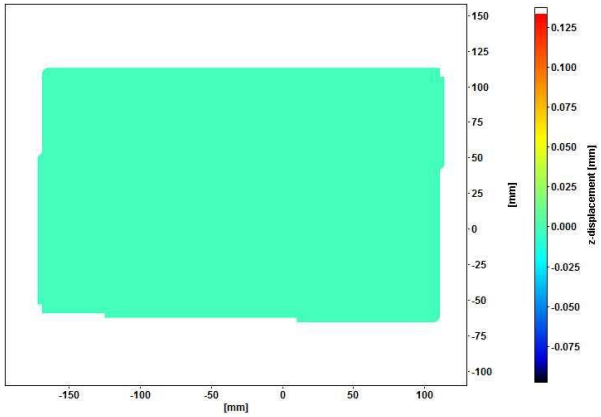

Image no 1

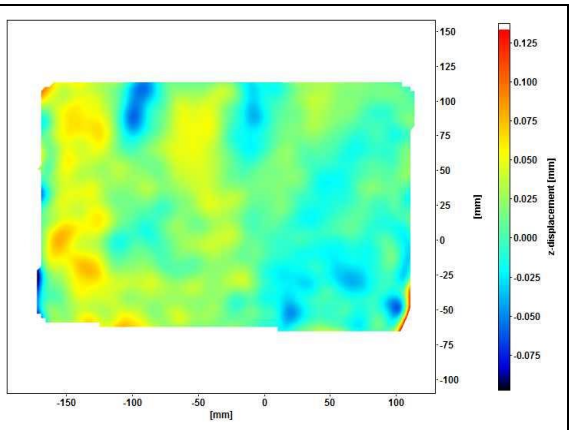

Image no 2

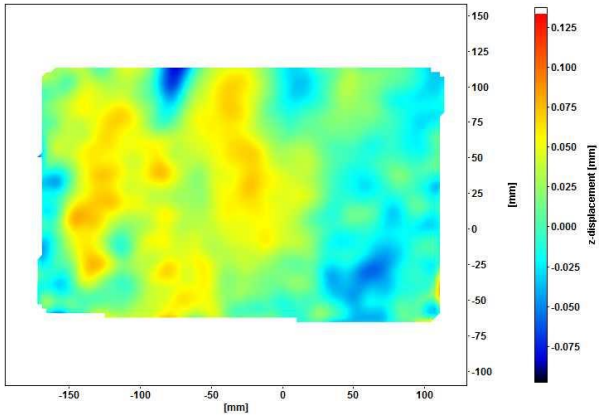

Image no 3

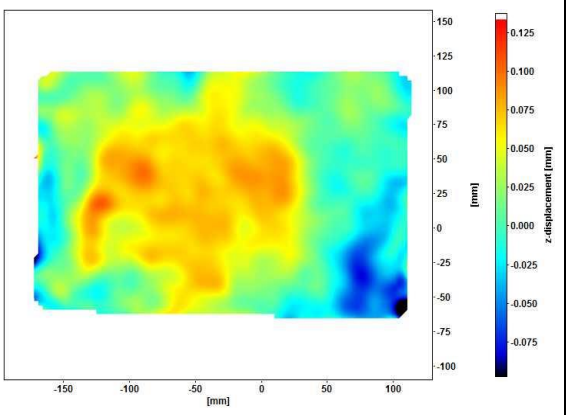

Image no 4

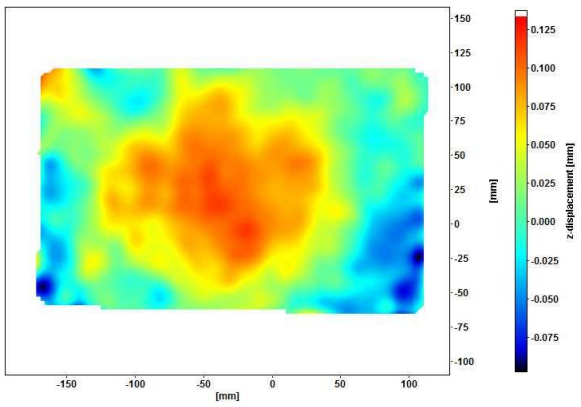

Image no 5

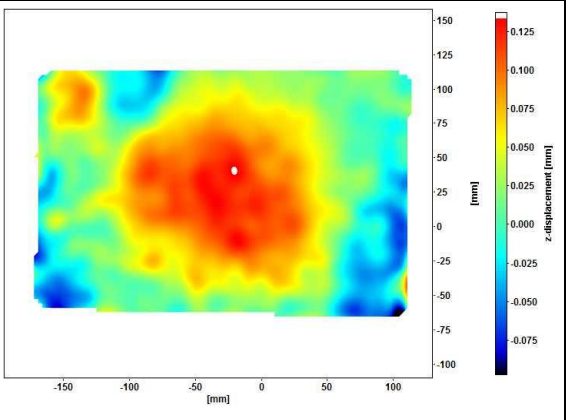

Image no 6

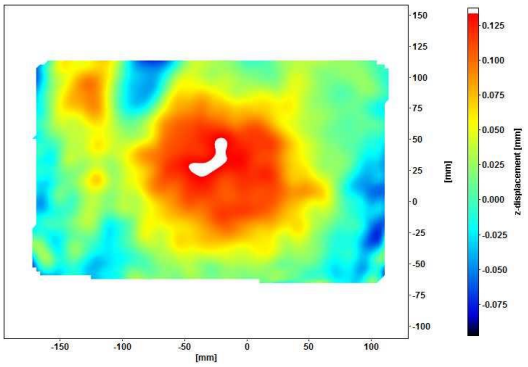

Image no 7

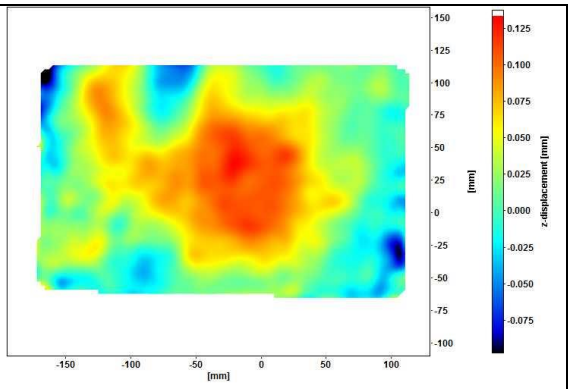

Image no 8

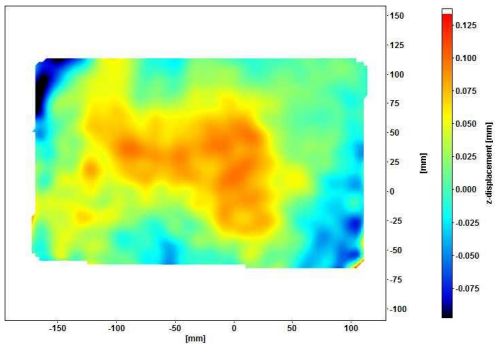

Image no 9

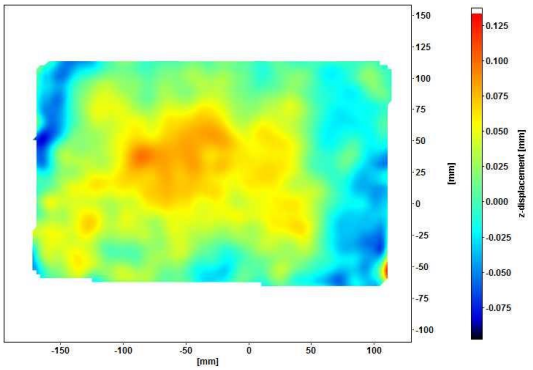

Image no 10

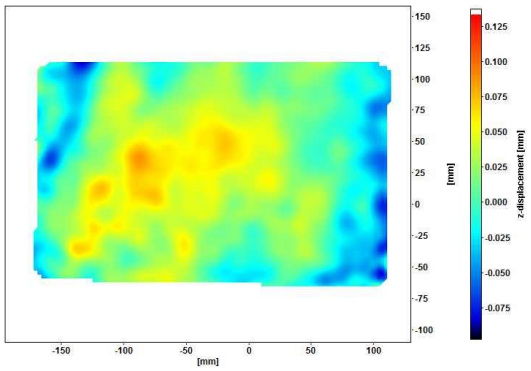

Image no 11

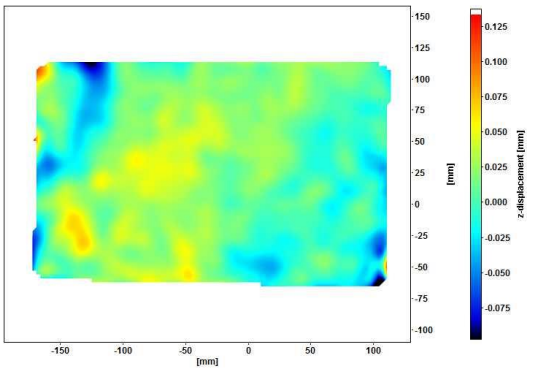

Image no 12

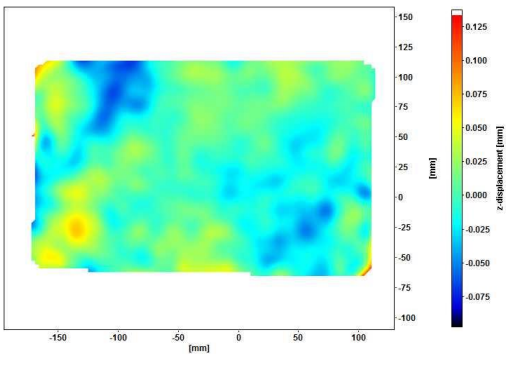

Image no 13

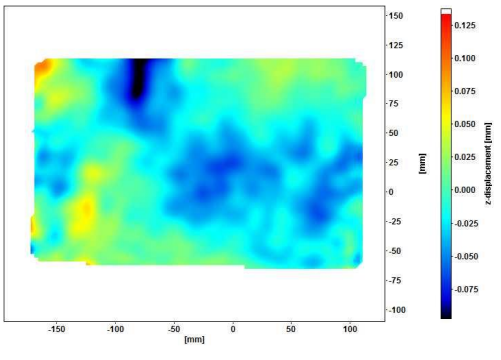

Image no 14

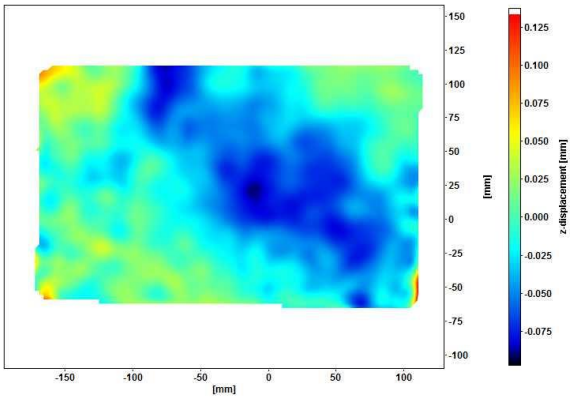

Image no 15

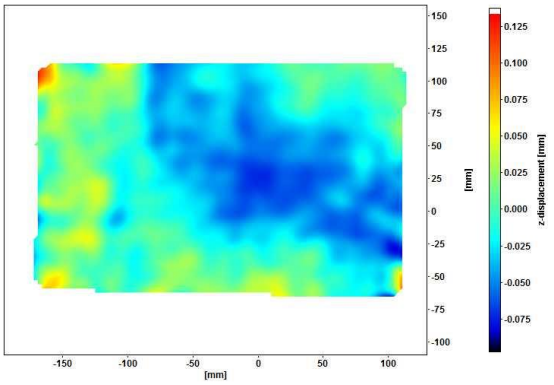

Image no 16

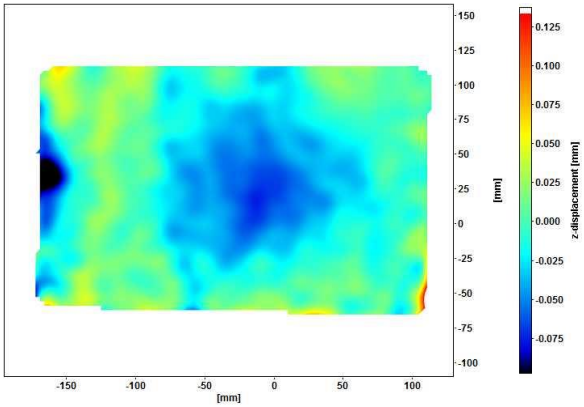

Image no 17

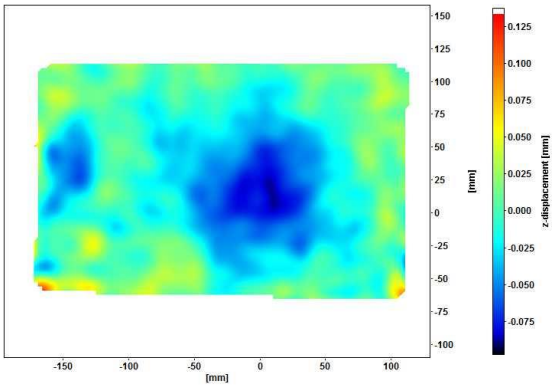

Image no 18

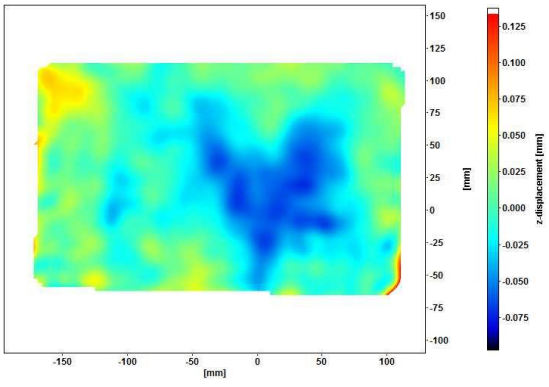

Image no 19

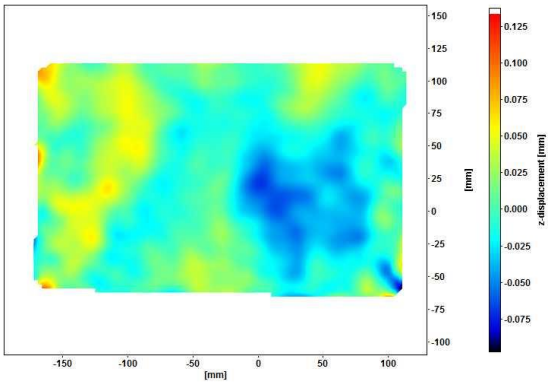

Image no 20

DIC complete image for mode shape (2,1)

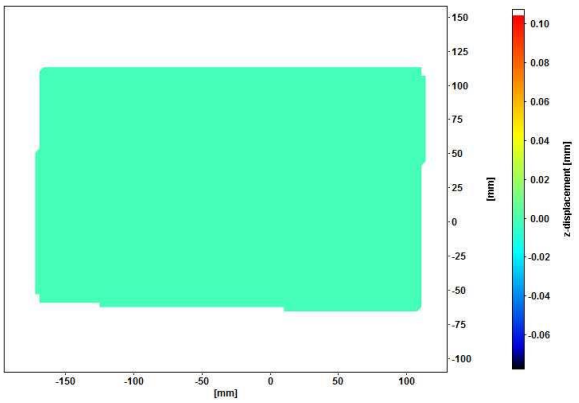

Image no 1

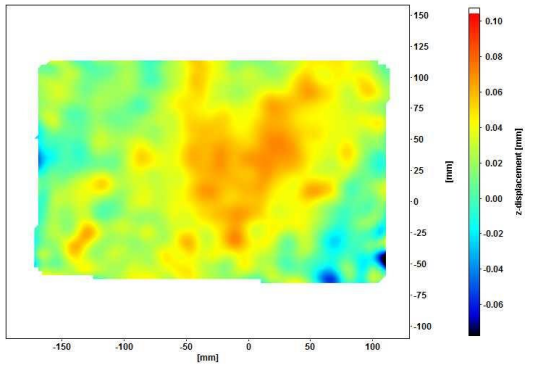

Image no 2

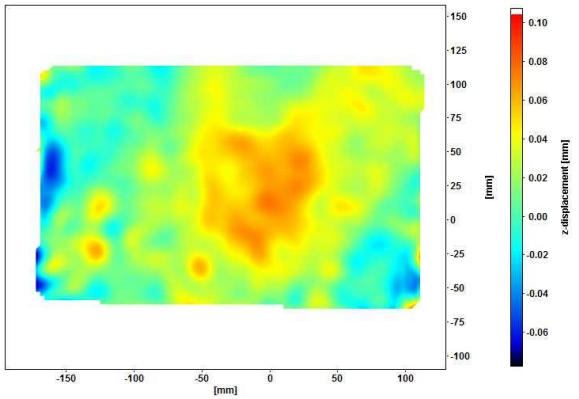

Image no 3

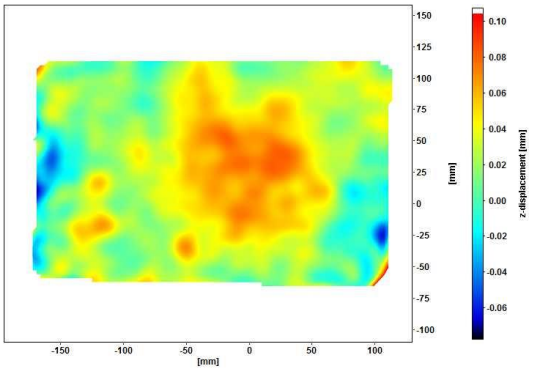

Image no 4

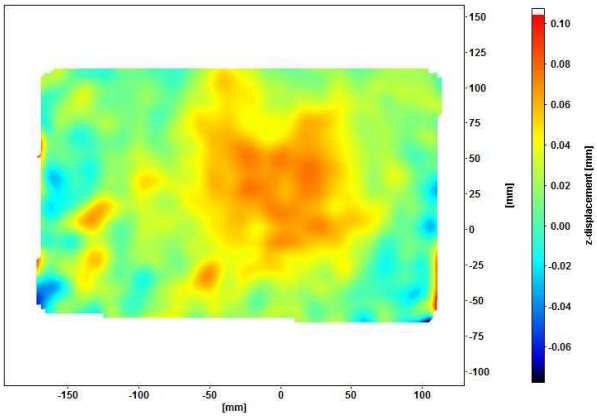

Image no 5

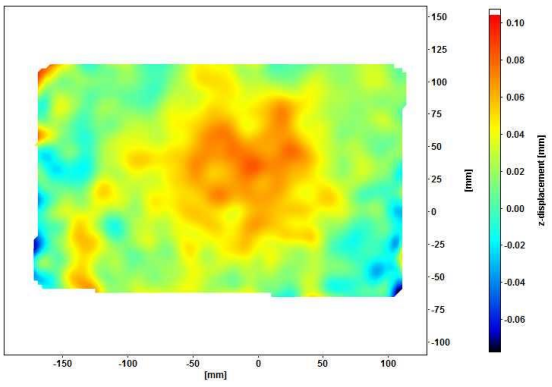

Image no 6

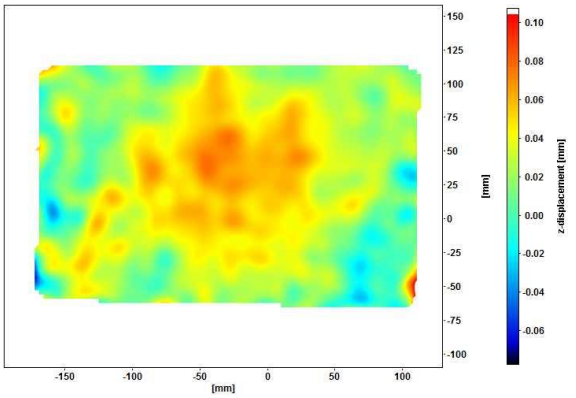

Image no 7

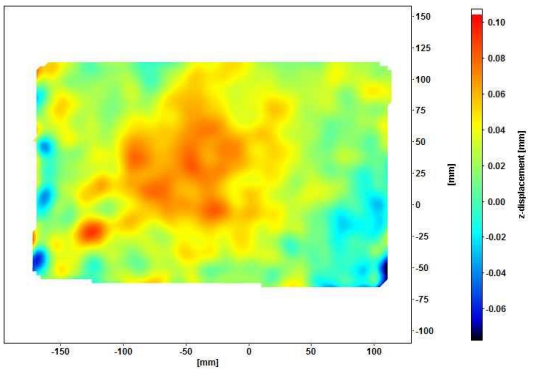

Image no 8

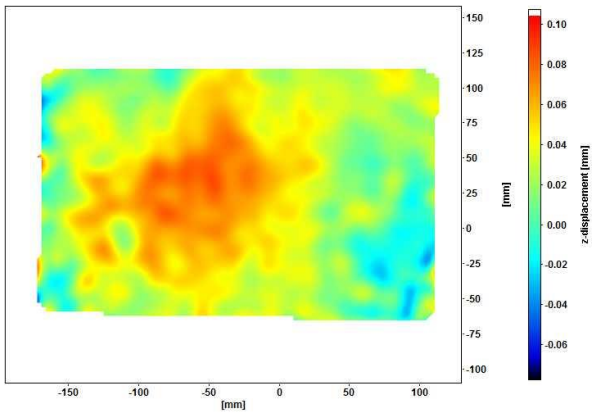

Image no 9

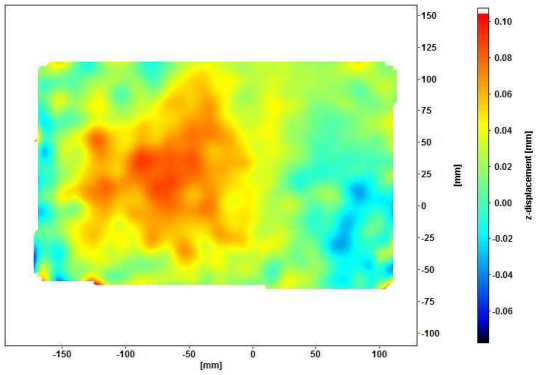

Image no 10

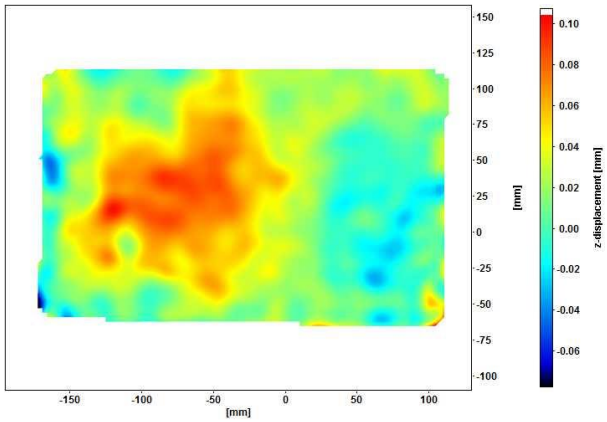

Image no 11

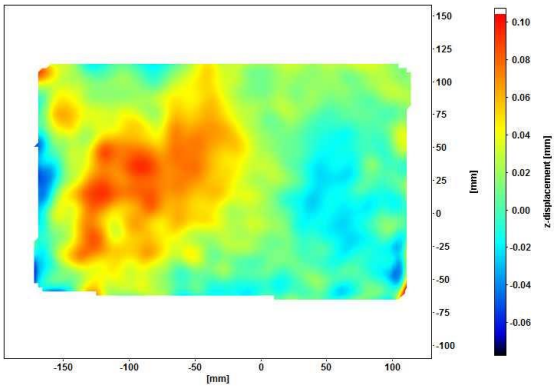

Image no 12

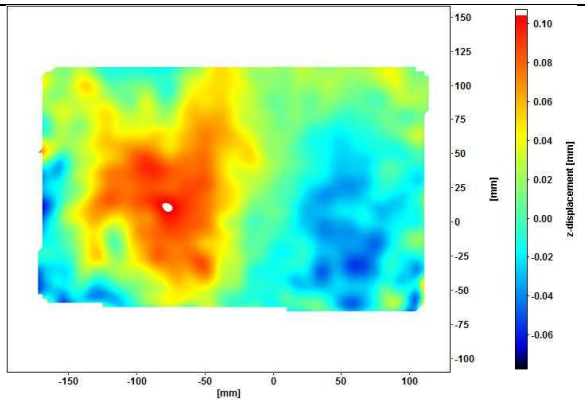

Image no 13

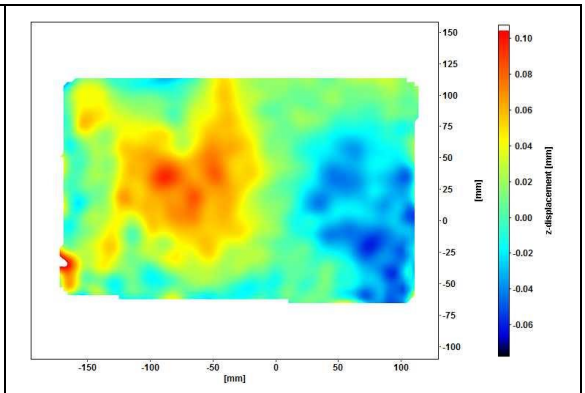

Image no 14

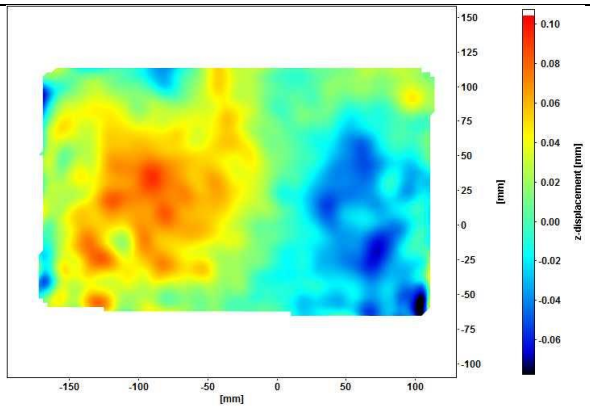

Image no 15

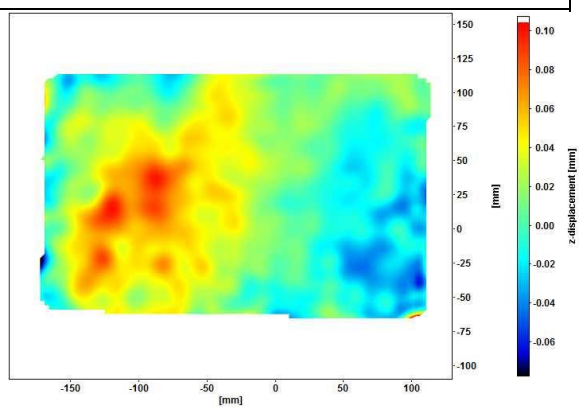

Image no 16

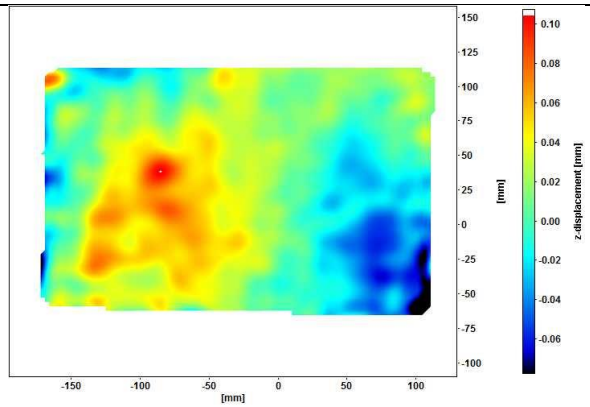

Image no 17

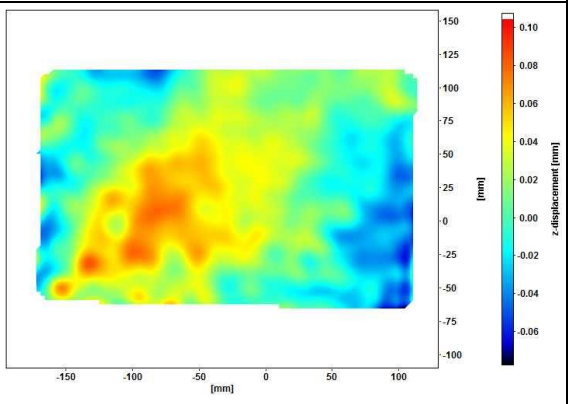

Image no 18

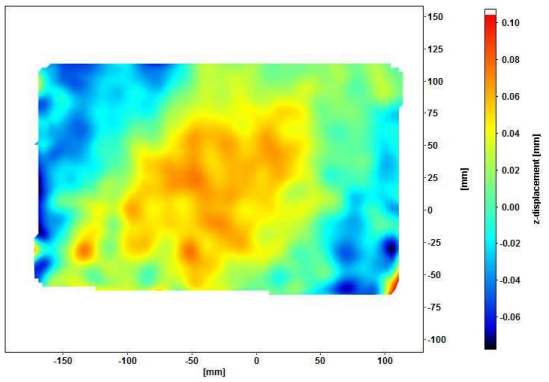

Image no 19

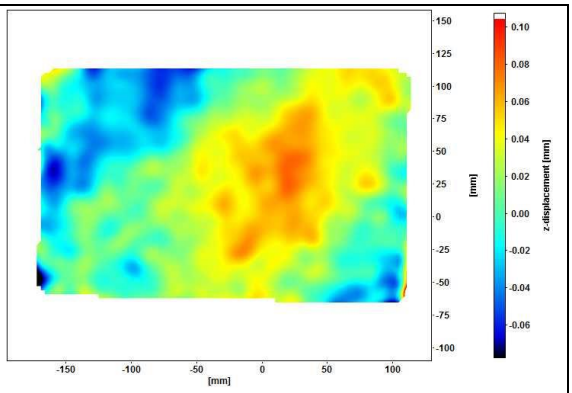

Image no 20

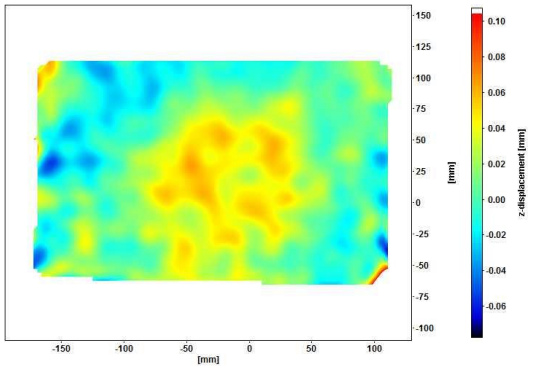

Image no 21

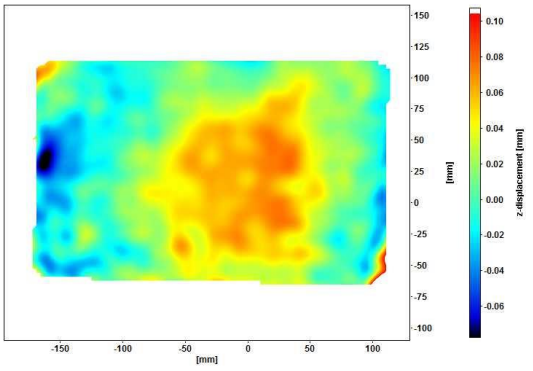

Image no 22

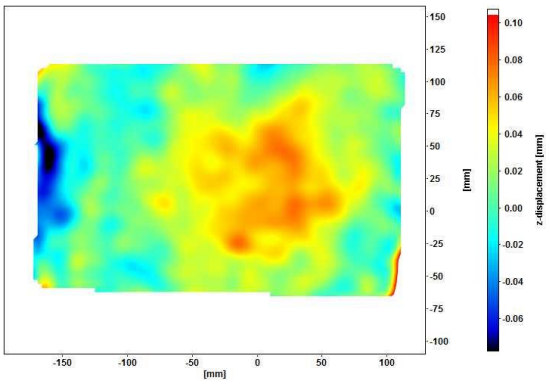

Image no 23

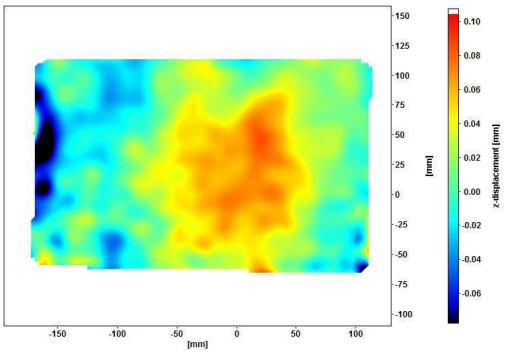

Image no 24

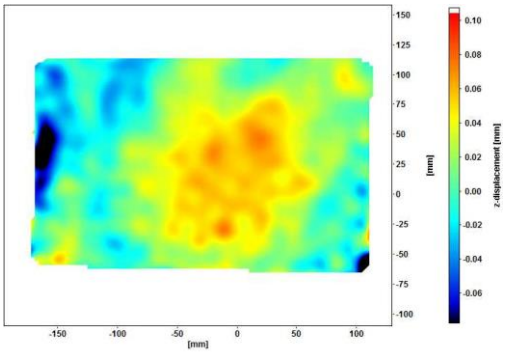

Image no 25

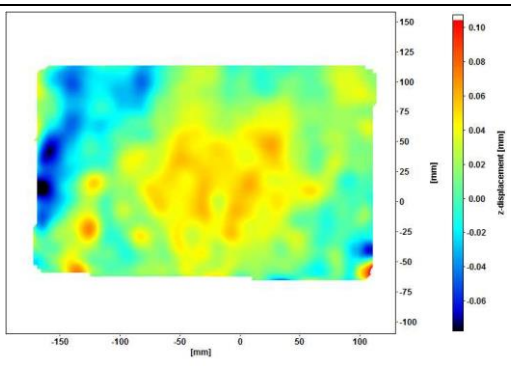

Image no 26

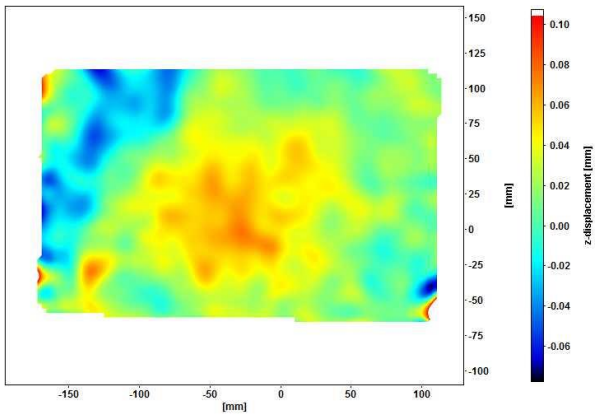

Image no 27

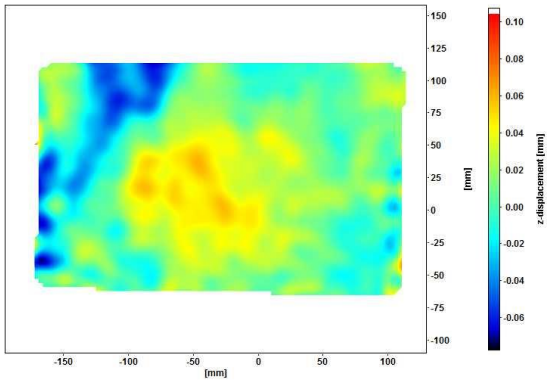

Image no 28

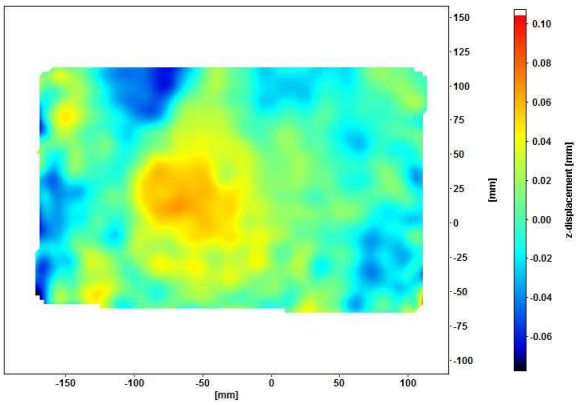

Image no 29

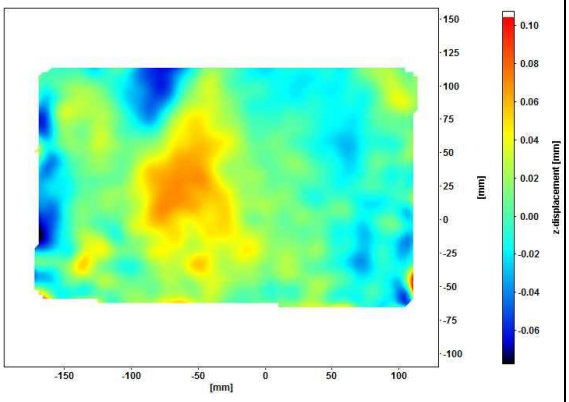

Image no 30

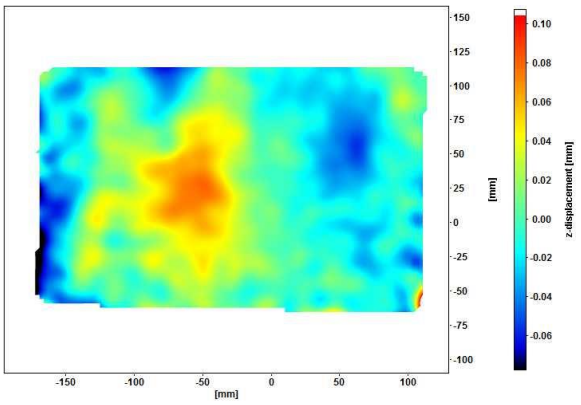

Image no 31

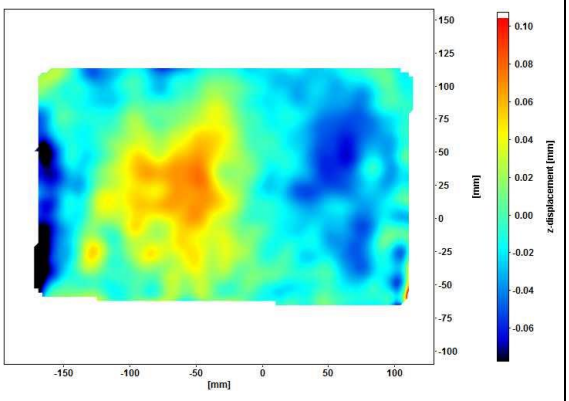

Image no 32

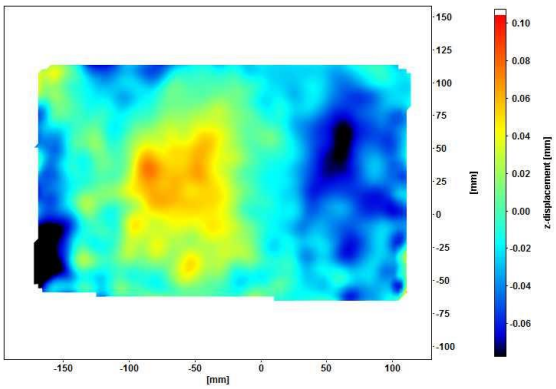

Image no 33

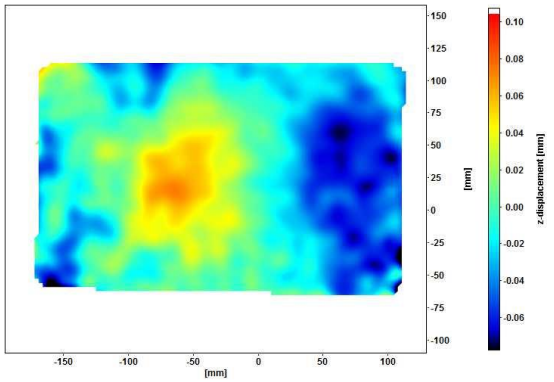

Image no 34

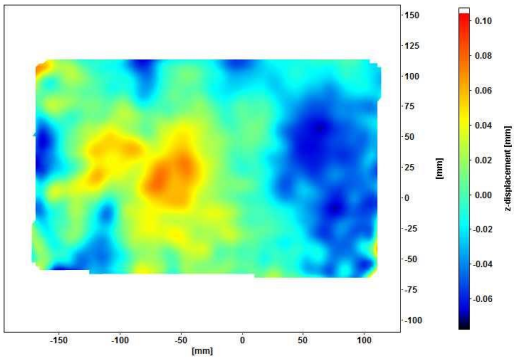

Image no 35

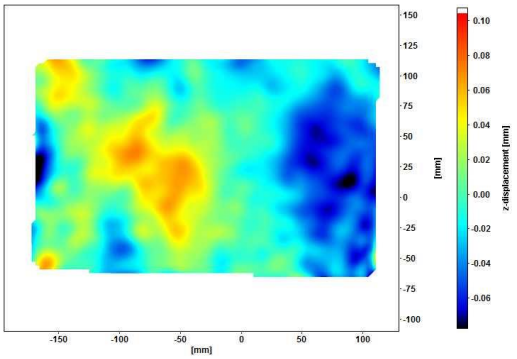

Image no 36

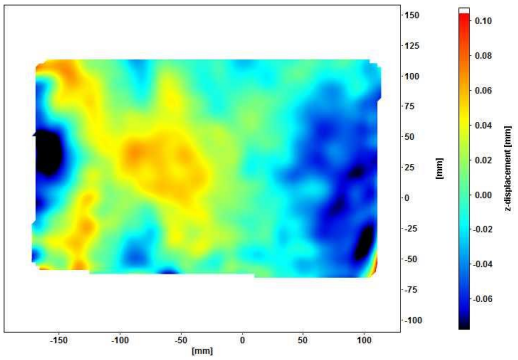

Image no 37

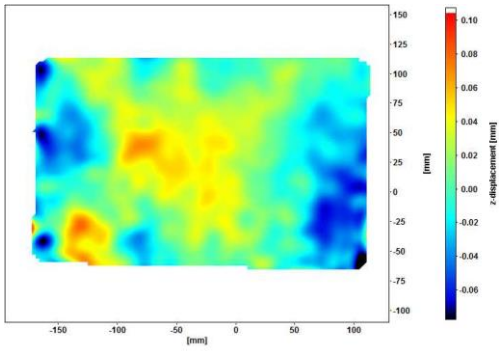

Image no 38

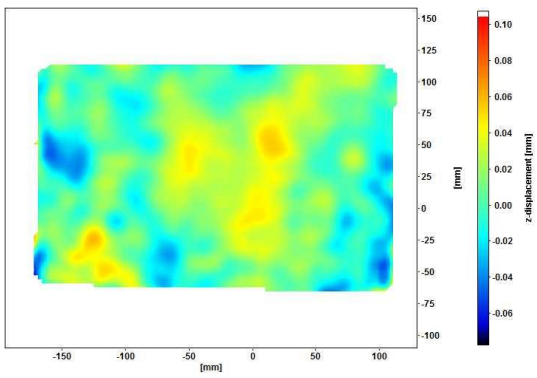

Image no 39

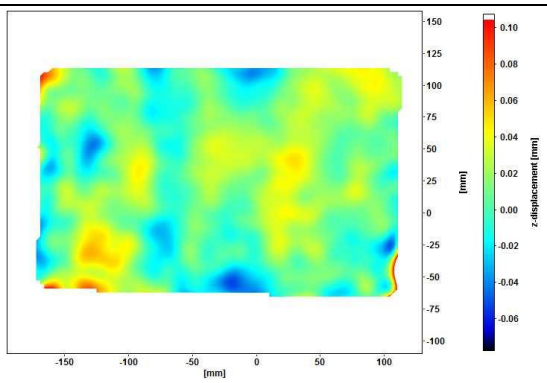

Image no 40

Matlab Cooding For Radiatian Efficiency Baffled Case- Simply Supported

```
% Radiation Efficiency for baffled case- simply supported

clc;
clear all;
close all;

%-------------------------- size plate -----------------------------------
a =0.297;                                                       % unit m
b =0.198;                                                       % unit m
h = 0.0012;                                                     % unit m

%------------- Air properties for radiation efficency formula -------------
rho = 1.225 ;                                          % density of air kg/m3
c = 343 ;                                              % speed of sound, ms-2
S = a*b ;                                              % surface area

%-------------------------- plate properties ------------------------------
Ep =  2.00*10^11;                   % modulus young plate N/m2
v = 0.272 ;                         % poisson ration
rho_plate = 7817 ;                  % density of plate kg/m3 - stainless
ms = rho_plate*h;                   % mass per unit area of the plate

%integer mode shape (example mode 2,2) -----------
%                                    %
m = 2;                              % mode shape
n = 2;                              %
%                                    %

freq = ((0:10000)') ;               % freq calculation
omega = 2*pi* freq ;
k = omega./ c ;

Mmn = ms*a*b/4 ;
M = 4*Mmn ;

Vmn(:,1)=freq ;

radeff_mnA = (64*a*b*(k.^2))./((pi^6)*(m^2)*(n^2)) ;

%utk case m = odd, n= odd-----------------------------------------------------
%radeff_mnJ =
@(G,H)((((cos((k*a*sin(G)*cos(H))/2)).*(cos((k*b*sin(G)*sin(H))/2))./(((((
k*a*sin(G)*cos(H))./(m*pi)).^2)-1).*((((k*b*sin(G)*sin(H))./(n*pi)).^2)-
1))).^2).* (sin(G));
%radeff_mnK = quadv(@(H) quadv(@(G)
radeff_mnJ(G,H),0,pi/2,'ArrayValued',true),0,pi/2,'ArrayValued',true) ; %
original code: radeff_mnK = dblquad(radeff_mnJ,0,pi/2,0,pi/2) ;
%-------------------------------------------------------------------------

%utk case m = even, n= even---------------------------------------------------
radeff_mnJ =
@(G,H)((((sin((k*a*sin(G).*cos(H))/2)).*(sin((k*b*sin(G)*sin(H))/2))./((((
(k*a*sin(G)*cos(H))./(m*pi)).^2)-1).*((((k*b*sin(G)*sin(H))./(n*pi)).^2)-
1))).^2).*(sin(G));
radeff_mnK = quadv(@(H) quadv(@(G)
radeff_mnJ(G,H),0,pi/2,'ArrayValued',true),0,pi/2,'ArrayValued',true)
```

```
%-------------------------------------------------------------------------

%utk case m = even, n= odd-----------------------------------------------
%radeff_mnJ =
@(G,H)((((sin((k*a*sin(G).*cos(H))/2)).*(cos((k*b*sin(G)*sin(H))/2))./(((((
(k*a*sin(G)*cos(H))./(m*pi)).^2)-1).*((((k*b*sin(G)*sin(H))./(n*pi)).^2)-
1))).^2).*(sin(G));
%radeff_mnK = quadv(@(H) quadv(@(G)
radeff_mnJ(G,H),0,pi/2,'ArrayValued',true),0,pi/2,'ArrayValued',true);
%-------------------------------------------------------------------------

%utk kes m = odd, n= even-------------------------------------------------
%radeff_mnJ =
@(G,H)((((cos((k*a*sin(G)*cos(H))/2)).*(sin((k*b*sin(G)*sin(H))/2))./(((((
k*a*sin(G)*cos(H))./(m*pi)).^2)-1).*((((k*b*sin(G)*sin(H))./(n*pi)).^2)-
1))).^2).*(sin(G));
%radeff_mnK = quadv(@(H) quadv(@(G)
radeff_mnJ(G,H),0,pi/2,'ArrayValued',true),0,pi/2,'ArrayValued',true)
%-------------------------------------------------------------------------

% CHECK UTK KES M,N EVEN AND ODD -
% COS (a/2) dan cos (b/2) hanya bila m,n odd
% sin (a/2) dan Sin (b/2) hanya bila m,n even
% check utk combination odd-even
%-------------------------------------------------------------------------


radeff_mnL= radeff_mnA.*radeff_mnK;

figure;
plot(Vmn(:,1),radeff_mnK,'r');
loglog(Vmn(:,1),radeff_mnK,'r');
xlabel('frequency');
ylabel('Nilai kamiran');
legend('kamiran vs frequency');


figure;
plot(Vmn(:,1),radeff_mnL,'r');
loglog(Vmn(:,1),radeff_mnL,'r');
xlabel('frequency');
ylabel('Radiation Efficiency');
legend('Radiation Efficiency vs frequency');
```

Matlab for Predicting Spatial Average Mean-Square Velocity

```
% Predicting mean-square velocity value based from DIC %

clc;
clear all;
close all;

f = 590                         ;                   %resonance frequency hz
ratioeff= 0.00013;                                  % reffer graf formula cremer

fid1 = fopen('B00001.dat','rt');                    %image static
fid2 = fopen('B00002.dat','rt');
fid3 = fopen('B00003.dat','rt');
fid4 = fopen('B00004.dat','rt');
fid5 = fopen('B00005.dat','rt');
fid6 = fopen('B00006.dat','rt');
fid7 = fopen('B00007.dat','rt');
fid8 = fopen('B00008.dat','rt');
fid9 = fopen('B00009.dat','rt');
fid10 = fopen('B00010.dat','rt');
fid11 = fopen('B00011.dat','rt');
fid12 = fopen('B00012.dat','rt');
fid13 = fopen('B00013.dat','rt');
fid14 = fopen('B00014.dat','rt');
fid15 = fopen('B00015.dat','rt');
fid16 = fopen('B00016.dat','rt');
fid17 = fopen('B00017.dat','rt');
fid18 = fopen('B00018.dat','rt');
fid19 = fopen('B00019.dat','rt');
fid20 = fopen('B00020.dat','rt');
fid21 = fopen('B00021.dat','rt');
fid22 = fopen('B00022.dat','rt');
fid23 = fopen('B00023.dat','rt');
fid24 = fopen('B00024.dat','rt');
fid25 = fopen('B00025.dat','rt');
fid26 = fopen('B00026.dat','rt');
fid27 = fopen('B00027.dat','rt');
fid28 = fopen('B00028.dat','rt');
fid29 = fopen('B00029.dat','rt');
fid30 = fopen('B00030.dat','rt');
fid31 = fopen('B00031.dat','rt');
fid32 = fopen('B00032.dat','rt');
fid33 = fopen('B00033.dat','rt');
fid34 = fopen('B00034.dat','rt');
fid35 = fopen('B00035.dat','rt');
fid36 = fopen('B00036.dat','rt');
fid37 = fopen('B00037.dat','rt');
fid38 = fopen('B00038.dat','rt');
fid39 = fopen('B00039.dat','rt');
fid40 = fopen('B00040.dat','rt');
fid41 = fopen('B00041.dat','rt');
fid42 = fopen('B00042.dat','rt');
fid43 = fopen('B00043.dat','rt');

d1 = textscan(fid1, '%f%f%f%f%f%f', 'HeaderLines',3, 'CollectOutput',1);
%image static
d2 = textscan(fid2, '%f%f%f%f%f%f', 'HeaderLines',3, 'CollectOutput',1);
d3 = textscan(fid3, '%f%f%f%f%f%f', 'HeaderLines',3, 'CollectOutput',1);
```

```
d4 = textscan(fid4, '%f%f%f%f%f%f', 'HeaderLines',3, 'CollectOutput',1);
d5 = textscan(fid5, '%f%f%f%f%f%f', 'HeaderLines',3, 'CollectOutput',1);
d6 = textscan(fid6, '%f%f%f%f%f%f', 'HeaderLines',3, 'CollectOutput',1);
d7 = textscan(fid7, '%f%f%f%f%f%f', 'HeaderLines',3, 'CollectOutput',1);
d8 = textscan(fid8, '%f%f%f%f%f%f', 'HeaderLines',3, 'CollectOutput',1);
d9 = textscan(fid9, '%f%f%f%f%f%f', 'HeaderLines',3, 'CollectOutput',1);
d10 = textscan(fid10, '%f%f%f%f%f%f', 'HeaderLines',3, 'CollectOutput',1);
d11 = textscan(fid11, '%f%f%f%f%f%f', 'HeaderLines',3, 'CollectOutput',1);
d12 = textscan(fid12, '%f%f%f%f%f%f', 'HeaderLines',3, 'CollectOutput',1);
d13 = textscan(fid13, '%f%f%f%f%f%f', 'HeaderLines',3, 'CollectOutput',1);
d14 = textscan(fid14, '%f%f%f%f%f%f', 'HeaderLines',3, 'CollectOutput',1);
d15 = textscan(fid15, '%f%f%f%f%f%f', 'HeaderLines',3, 'CollectOutput',1);
d16 = textscan(fid16, '%f%f%f%f%f%f', 'HeaderLines',3, 'CollectOutput',1);
d17 = textscan(fid17, '%f%f%f%f%f%f', 'HeaderLines',3, 'CollectOutput',1);
d18 = textscan(fid18, '%f%f%f%f%f%f', 'HeaderLines',3, 'CollectOutput',1);
d19 = textscan(fid19, '%f%f%f%f%f%f', 'HeaderLines',3, 'CollectOutput',1);
d20 = textscan(fid20, '%f%f%f%f%f%f', 'HeaderLines',3, 'CollectOutput',1);
d21 = textscan(fid21, '%f%f%f%f%f%f', 'HeaderLines',3, 'CollectOutput',1);
d22 = textscan(fid22, '%f%f%f%f%f%f', 'HeaderLines',3, 'CollectOutput',1);
d23 = textscan(fid23, '%f%f%f%f%f%f', 'HeaderLines',3, 'CollectOutput',1);
d24 = textscan(fid24, '%f%f%f%f%f%f', 'HeaderLines',3, 'CollectOutput',1);
d25 = textscan(fid25, '%f%f%f%f%f%f', 'HeaderLines',3, 'CollectOutput',1);
d26 = textscan(fid26, '%f%f%f%f%f%f', 'HeaderLines',3, 'CollectOutput',1);
d27 = textscan(fid27, '%f%f%f%f%f%f', 'HeaderLines',3, 'CollectOutput',1);
d28 = textscan(fid28, '%f%f%f%f%f%f', 'HeaderLines',3, 'CollectOutput',1);
d29 = textscan(fid29, '%f%f%f%f%f%f', 'HeaderLines',3, 'CollectOutput',1);
d30 = textscan(fid30, '%f%f%f%f%f%f', 'HeaderLines',3, 'CollectOutput',1);
d31 = textscan(fid31, '%f%f%f%f%f%f', 'HeaderLines',3, 'CollectOutput',1);
d32 = textscan(fid32, '%f%f%f%f%f%f', 'HeaderLines',3, 'CollectOutput',1);
d33 = textscan(fid33, '%f%f%f%f%f%f', 'HeaderLines',3, 'CollectOutput',1);
d34 = textscan(fid34, '%f%f%f%f%f%f', 'HeaderLines',3, 'CollectOutput',1);
d35 = textscan(fid35, '%f%f%f%f%f%f', 'HeaderLines',3, 'CollectOutput',1);
d36 = textscan(fid36, '%f%f%f%f%f%f', 'HeaderLines',3, 'CollectOutput',1);
d37 = textscan(fid37, '%f%f%f%f%f%f', 'HeaderLines',3, 'CollectOutput',1);
d38 = textscan(fid38, '%f%f%f%f%f%f', 'HeaderLines',3, 'CollectOutput',1);
d39 = textscan(fid39, '%f%f%f%f%f%f', 'HeaderLines',3, 'CollectOutput',1);
d40 = textscan(fid40, '%f%f%f%f%f%f', 'HeaderLines',3, 'CollectOutput',1);
d41 = textscan(fid41, '%f%f%f%f%f%f', 'HeaderLines',3, 'CollectOutput',1);
d42 = textscan(fid42, '%f%f%f%f%f%f', 'HeaderLines',3, 'CollectOutput',1);
d43 = textscan(fid43, '%f%f%f%f%f%f', 'HeaderLines',3, 'CollectOutput',1);

A1 = cell2mat(d1);
A2 = cell2mat(d2);
A3 = cell2mat(d3);
A4 = cell2mat(d4);
A5 = cell2mat(d5);
A6 = cell2mat(d6);
A7 = cell2mat(d7);
A8 = cell2mat(d8);
A9 = cell2mat(d9);
A10 = cell2mat(d10);
A11 = cell2mat(d11);
A12 = cell2mat(d12);
A13 = cell2mat(d13);
A14 = cell2mat(d14);
A15 = cell2mat(d15);
A16 = cell2mat(d16);
A17 = cell2mat(d17);
A18 = cell2mat(d18);
A19 = cell2mat(d19);
A20 = cell2mat(d20);
```

```
A21 = cell2mat(d21);
A22 = cell2mat(d22);
A23 = cell2mat(d23);
A24 = cell2mat(d24);
A25 = cell2mat(d25);
A26 = cell2mat(d26);
A27 = cell2mat(d27);
A28 = cell2mat(d28);
A29 = cell2mat(d29);
A30 = cell2mat(d30);
A31 = cell2mat(d31);
A32 = cell2mat(d32);
A33 = cell2mat(d33);
A34 = cell2mat(d34);
A35 = cell2mat(d35);
A36 = cell2mat(d36);
A37 = cell2mat(d37);
A38 = cell2mat(d38);
A39 = cell2mat(d39);
A40 = cell2mat(d40);
A41 = cell2mat(d41);
A42 = cell2mat(d42);
A43 = cell2mat(d43);

A(:,1)=A1(:,1);                                  %coordinate x
A(:,2)=A1(:,2);                                  %coordinate y
A(:,3)=A1(:,6);        %displacement image 1 - static image displacement=0
A(:,4)=A2(:,6);        %displacement image 2
A(:,5)=A3(:,6);        %displacement image 3
A(:,6)=A4(:,6);        %displacement image 4
A(:,7)=A5(:,6);        %displacement image 5
A(:,8)=A6(:,6);        %displacement image 6
A(:,9)=A7(:,6);        %displacement image 7
A(:,10)=A8(:,6);       %displacement image 8
A(:,11)=A9(:,6);       %displacement image 9
A(:,12)=A10(:,6);      %displacement image 10
A(:,13)=A11(:,6);      %displacement image 11
A(:,14)=A12(:,6);      %displacement image 12
A(:,15)=A13(:,6);      %displacement image 13
A(:,16)=A14(:,6);      %displacement image 14
A(:,17)=A15(:,6);      %displacement image 15
A(:,18)=A16(:,6);      %displacement image 16
A(:,19)=A17(:,6);      %displacement image 17
A(:,20)=A18(:,6);      %displacement image 18
A(:,21)=A19(:,6);      %displacement image 19
A(:,22)=A20(:,6);      %displacement image 20
A(:,23)=A21(:,6);      %displacement image 21
A(:,24)=A22(:,6);      %displacement image 22
A(:,25)=A23(:,6);      %displacement image 23
A(:,26)=A24(:,6);      %displacement image 24
A(:,27)=A25(:,6);      %displacement image 25
A(:,28)=A26(:,6);      %displacement image 26
A(:,29)=A27(:,6);      %displacement image 27
A(:,30)=A28(:,6);      %displacement image 28
A(:,31)=A29(:,6);      %displacement image 29
A(:,32)=A30(:,6);      %displacement image 30
A(:,33)=A31(:,6);      %displacement image 31
A(:,34)=A32(:,6);      %displacement image 32
A(:,35)=A33(:,6);      %displacement image 33
A(:,36)=A34(:,6);      %displacement image 34
A(:,37)=A35(:,6);      %displacement image 35
```

```
A(:,38)=A36(:,6);      %displacement image 36
A(:,39)=A37(:,6);      %displacement image 37
A(:,40)=A38(:,6);      %displacement image 38
A(:,41)=A39(:,6);      %displacement image 39
A(:,42)=A40(:,6);      %displacement image 40
A(:,43)=A41(:,6);      %displacement image 41
A(:,44)=A42(:,6);      %displacement image 42
A(:,45)=A43(:,6);      %displacement image 43

%-------------------------------------------------------------------------
%-------------------------------------------------------------------------
%specific condition for trim - area luar dari panel sample tp dalam
%view = camera (depend FOV camera)

fallv = A(:,2)>116;           % y direction higher value % manually decide
fallx= A(:,2)<-64;            % y direction lower value
fally= A(:,1)>115;            % x direction higher value
fallz= A(:,1)<-170;           % x direction lower value

%combine all yg nak buang (trim)
Tfall= fallv|fallx|fally|fallz;                    % | logic utk "or"
A(Tfall,:) = [];

% untuk pilih imej number spesific cycle---------------------------------
% image selection
B = A (:, 3:45) ;

% contoh nak imej 4--> 24  ( tulis (4+2) ---> (24+2) sbb colum 1 dan 2
adalah koordinat         <<<<<---=+++++_----------------------


%Dari raw data, coloum 1 = koordinat x,coloum 2 = koordinat y,coloum 6 =
%displacement dalam arah z,
x = A(:,1);
y = A(:,2);
z = B(:,11);

% contoh image no. 5- image 1 statik tiada displacement (utk B -imej asal
no.4 (di A) kini adalah no.1 (di B)


%-------------------------------------------------------------------------
%-------------------------------------------------------------------------

%plot displacement arah Z
xi=linspace(min(x),max(x),106);
yi=linspace(min(y),max(y),94);

[XI YI]=meshgrid(xi,yi);
ZI = griddata(x,y,z,XI,YI);
contourf(XI,YI,ZI,400,'LineColor','none');    %15 = bilangan countour line
%c=colorbar;                                  %utk adakan colorbar
colorbar('FontSize',10);
%a=colorbar;
%title(a,'Z-direction (mm)');

xlabel('x (mm)');
ylabel('y (mm)');
title ('Displacement Z-direction (mm)');
```

```
figure;
surf(XI,YI,ZI);
colorbar;
xlabel('x (mm)');
ylabel('y (mm)');
zlabel('Displacement (mm)');

% Create the stem chart in position 1 of a 2x1 grid
figure;
subplot(2,1,1)
contourf(XI,YI,ZI,200,'LineColor','none');   %15 = bilangan countour line
colorbar;                                    %utk adakan colorbar
xlabel('x (mm)');
ylabel('y (mm)');
colorbar;

% Create the stem chart in position 2 of a 2x1 grid
subplot(2,1,2)
surf(XI,YI,ZI);
colorbar;
xlabel('x (mm)');
ylabel('y (mm)');
zlabel('Displacement (mm)- image no.8');

%-------------------------------------------------------------------------
%-------------------------------------------------------------------------
%kiraan untuk velocity surface
% omega

omega = 2*pi*f ;
velocityMM =(B(:,:).*omega);              %unit mm/s-1  **** check ini****
velocityM= (velocityMM.*0.001) ;          %Convert ke m/s

v= velocityM(:,9);                        %contoh halaju image no.5

%plot halaju
figure ;
VI = griddata(x,y,v,XI,YI);
contourf(XI,YI,VI,200,'LineColor','none');    %200 = bilangan countour line
colorbar;                                     %utk adakan colorbar
xlabel('x (mm)');
ylabel('y (mm)');
title ('Velocity Z-direction (m/s-2)- image no.8');

%-------------------------------------------------------------------------
%-------------------------------------------------------------------------
%

velocity2= velocityM.*velocityM;                        %velocity kuasa dua
[m,n]=size(velocity2);

v2= velocity2(:,11);                              % velocity2 for image no.8

figure ;
V2I = griddata(x,y,v2,XI,YI);
contourf(XI,YI,V2I,200,'LineColor','none');  %200 = bilangan countour line
colorbar;                                    %utk adakan colorbar
xlabel('x (mm)');
```

```
ylabel('y (mm)');
title ('Velocity2 Z-direction (m2/s4)- image no.8');


v2avgT = ((1/(n))*sum(velocity2(:,1:end),2)) ;     %velocity2 average for
area overtime
[a,b]=size(v2avgT);

maxX= max(A(:,1))*0.001;                    % maximum koordinat x in meter
minX= min(A(:,1))*0.001 ;                   % minimum koordinat x in meter
maxY= max(A(:,2))*0.001  ;                  % maximum koordinat y in meter
minY= min(A(:,2))*0.001   ;                % minimum koordinat y in meter

bigarea = (maxX-minX)* (maxY-minY)
smallarea = bigarea/a

%(B(:,:).*omega);
v2avgT_smallarea= (v2avgT (:,:).*smallarea);

%kiraan lama tak ambik kira area.
     v2avgTarea = ((1/(a))*sum(v2avgT(:,1:end)))                    %m2s-2

%v2avgTarea = ((1/(bigarea))*sum(v2avgT_smallarea(:,1:end)))
%m2s-2

%figure average mean square over time - number of image
figure ;
V3I = griddata(x,y,v2avgT,XI,YI);
contourf(XI,YI,V3I,200,'LineColor','none');  %200 = bilangan countour line
colorbar;                                    %utk adakan colorbar
xlabel('x (mm)');
ylabel('y (mm)');
title ('Velocity2 Z-direction (m2/s4)- overtime - all of the images');


% Kiraan utk sound Power-----------------------------------------------------
%--
%-- W = rho*c*S*v*efficiency.
%--
%-------------------------------------------------------------------------


rho= 1.225;                          % air density kg/m3
c = 343;                             % speed op sound  ms-1

Lx =0.298 ;                          % 308mm
Ly =0.197;                           % 207mm
S= Lx*Ly;


SoundPower= rho*c*S*ratioeff*(v2avgTarea)    % dalam unit watt

SPWreff = 10^-12;     % 1pW

SoundPower_dB =10*log10(SoundPower/SPWreff)
```

```
%untuk check value velocity bagi permukaan plat----------------------------
%secara theory - value ini sepatutnya 0 ----------------------------------
%-------------------------------------------------------------------------

velocityMavgT = ((1/(n))*sum(velocityM(:,1:end),2)) ;           %velocity2
average for area overtime
[a,b]=size(velocityMavgT);

velocityavgT_smallarea= (velocityMavgT (:,:).*smallarea);
velocityavgTarea2 = ((1/(bigarea))*sum(velocityavgT_smallarea(:,1:end)))

%_-----------------------------------------------------------------------------
%-----------------------------------------------------------------------------

%[j k]=size(B);

delta2=velocityavgTarea2^2
newV2=  v2avgTarea-delta2

NewSoundPower= rho*c*S*ratioeff*(newV2);             % New dalam unit watt

NewSoundPower_dB =10*log10(NewSoundPower/SPWreff)
```